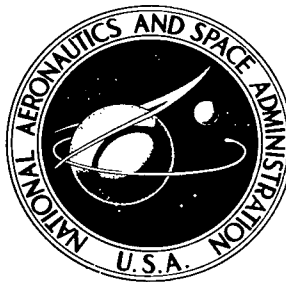


NASA TECHNICAL NOTE

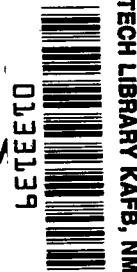


NASA TN D-6294

e.1

NASA TN D-6294

LOAN COPY: RETURN
AFWL (DOGL)
KIRTLAND AFB, N. M.



CALCULATION OF ELECTRON CONCENTRATION
FOR A BLUNT BODY AT ORBITAL SPEEDS
AND COMPARISON WITH EXPERIMENTAL DATA

*by Charles J. Schexnayder, Jr., Paul W. Huber,
and John S. Evans*

*Langley Research Center
Hampton, Va. 23365*



0133139

| | | | |
|--|--|---|----------------------|
| 1. Report No. NASA TN D-6294 | 2. Government Accession No. | 3. Recipient's Catalog No. | |
| 4. Title and Subtitle CALCULATION OF ELECTRON CONCENTRATION FOR A BLUNT BODY AT ORBITAL SPEEDS AND COMPARISON WITH EXPERIMENTAL DATA | | 5. Report Date May 1971 | |
| | | 6. Performing Organization Code | |
| 7. Author(s) Charles J. Schexnayder, Jr., Paul W. Huber, and John S. Evans | | 8. Performing Organization Report No. L-6705 | |
| | | 10. Work Unit No. 129-01-22-05 | |
| 9. Performing Organization Name and Address NASA Langley Research Center Hampton, Va. 23365 | | 11. Contract or Grant No. | |
| | | 13. Type of Report and Period Covered Technical Note | |
| 12. Sponsoring Agency Name and Address National Aeronautics and Space Administration Washington, D.C. 20546 | | 14. Sponsoring Agency Code | |
| | | 15. Supplementary Notes | |
| 16. Abstract <p>Calculation of electron concentration for a blunt-nosed body at orbital speeds has been made by use of pure-air nonequilibrium chemistry throughout the flow field and for the same flow field with alkali contamination (in local ionic equilibrium) in the boundary layer. Plasma diagnostic data from onboard Langmuir probes, reflectometers, and antenna voltage standing wave ratio (VSWR), along with passive data from attenuation of beacon and telemetry signals, are available for the first two RAM C reentries. These data are compared with calculated flow-field ionization and radio-frequency (RF) signal attenuation for both inviscid flow and for inviscid flow merged with boundary layer. In general, there is good agreement between plasma theory and the data. Above 71 km, ambipolar electron-ion diffusion was found to have a major influence on profile peak values of electron concentration. For RAM C-I at altitudes less than 60 km, there is a large increase in electron concentration in the boundary layer due to ionization of alkali impurities from the heat shield. Indications of boundary-layer transition along the body and of ablation rate on the nose were obtained from the low-altitude reflectometer data.</p> | | | |
| 17. Key Words (Suggested by Author(s)) Reentry communications Electron concentration Plasma sheath | | 18. Distribution Statement Unclassified - Unlimited | |
| 19. Security Classif. (of this report) Unclassified | 20. Security Classif. (of this page) Unclassified | 21. No. of Pages 84 | 22. Price* \$3.00 |

CALCULATION OF ELECTRON CONCENTRATION
FOR A BLUNT BODY AT ORBITAL SPEEDS AND COMPARISON
WITH EXPERIMENTAL DATA

By Charles J. Schexnayder, Jr., Paul W. Huber,
and John S. Evans
Langley Research Center

SUMMARY

Calculation of electron concentration for a blunt-nosed body at orbital speeds has been made by use of pure-air nonequilibrium chemistry throughout the flow field and for the same flow field with alkali contamination (in local ionic equilibrium) in the boundary layer. Plasma diagnostic data from onboard Langmuir probes, reflectometers, and antenna voltage standing wave ratio (VSWR), along with passive data from attenuation of beacon and telemetry signals, are available for the first two RAM C reentries. These data are compared with calculated flow-field ionization and radio-frequency (RF) signal attenuation for both inviscid flow and for inviscid flow merged with boundary layer. Good agreement between plasma theory and data is obtained in the altitude range between about 30 km and 71 km. At altitudes greater than 71 km, ambipolar electron-ion diffusion and wall recombination are shown to have a large effect on peak electron concentration in the plasma. For RAM C-I at altitudes less than 60 km, there is a large increase in electron concentration in the boundary layer due to ionization of alkali impurities from the heat shield. Indications of boundary-layer transition along the body and of ablation rate on the nose were obtained from the low-altitude reflectometer data.

INTRODUCTION

The free electrons which are produced in hypersonic-flow-field plasmas are the dominant factor in the entry radio blackout phenomenon. Therefore, in order to define, circumvent, or alleviate the blackout problem, it is important that one be able to determine the magnitude and distribution of electrons in the plasmas near communication antennas, as well as to determine the interactions which occur between the plasma, the antennas, and the propagating electromagnetic signals. Theoretical evaluation of the electron density levels and profiles for a given entry communications problem requires precise and detailed consideration of complex systems of chemical and thermodynamic processes for the complete shock layer, since free electrons are present only as trace

species in time-dependent systems. (See ref. 1.) Even with careful analysis, uncertainties in the flow species to be considered, the reaction rate coefficients, viscous interactions, antenna near-field effects, and so forth combine to make applicability to many real-life situations in doubt, particularly those involving ablation contamination (ref. 2) or high-altitude blackout.

The problem of radio blackout has led to the establishment of a flight project at the Langley Research Center called the Radio Attenuation Measurements Project (RAM). The basic objectives of Project RAM have been to obtain a better understanding of the factors which influence transmission of radio waves through entry vehicle plasmas and to search for ways to reduce or eliminate blackout.

The RAM project has included three series of flight payloads; namely, RAM A, RAM B, and RAM C. All were spherically blunted 9° half-angle cones with nose diameters of 5.08 cm (2 inches), 20.32 cm (8 inches), and 30.48 cm (12 inches), respectively. Maximum velocity for both the A and B series was about 5.5 km/sec (18 000 ft/sec) whereas the maximum speed for the C series was about 7.6 km/sec (25 000 ft/sec). Descriptions of the flights and the results were published in references 3 to 8 and references 9 to 12 dealt with an analysis of flight results.

The purpose of this paper is to compare flight results from RAM C-I and C-II with theoretical calculations and to draw some conclusions from the comparison. In addition to the reflectometer data of RAM C-II (ref. 8), this paper uses attenuation and signal blackout data from the receiving stations (refs. 7 and 8) to infer the plasma flow-field properties. Also, each RAM C flight carried a rake of Langmuir probes (refs. 7 and 13) which recorded ion concentration profiles on the aft part of the payload.

Included in the paper are appendix A which deals with the clean-air flow field, appendix B which deals with a mass conservation computer program, appendix C which gives details of the boundary-layer treatment, appendix D which shows the effects of ablation on the electron concentration in the boundary layer, and appendix E which gives the interpretation of low-altitude reflectometer data.

SYMBOLS

| | |
|-------------|--|
| A | surface area, cm^2 |
| \hat{C}_p | normalized pressure coefficient, $\frac{p - p_\infty}{p_{ns} - p_\infty}$ |
| c_p | specific heat at constant pressure of air mixture, $\text{erg-g}^{-1}\text{-K}^{-1}$ |
| D_l | reaction energy divided by RT_0 for l th reaction |

| | |
|-----------|--|
| d_N | body nose diameter, cm (in.) |
| F | fraction (by weight) of alkali contaminant in heat shield |
| f | signal frequency, MHz |
| G | degeneracy factor |
| H_i | enthalpy of i th species, erg-mole ⁻¹ |
| K_l | equilibrium constant for l th reaction, mole-cm ⁻³ or dimensionless |
| k_l | reaction rate constant for l th reaction, cm ³ -mole ⁻¹ -s ⁻¹ or cm ⁶ -mole ⁻² -s ⁻¹ |
| k | rarefaction parameter |
| l | reaction identification number |
| M | molecular weight, g-mole ⁻¹ ; also Mach number; also third body in a chemical reaction |
| m | flow rate, g-s ⁻¹ |
| \dot{m} | ablation gas surface flux, g-cm ⁻² -s ⁻¹ |
| N | quantity used in Saha equation (see eq. (13)) |
| N_A | Avogadro constant, 6.02217×10^{23} particles-mole ⁻¹ |
| N_e | electron concentration, electrons-cm ⁻³ |
| N_{Re} | Reynolds number |
| p | pressure, dyne-cm ⁻² |
| $Q_{i,l}$ | contribution of l th reaction rate to rate of change of i th species, mole ² -g ⁻² |
| R | gas constant, erg-mole ⁻¹ -K ⁻¹ or cm ³ -atm-mole ⁻¹ -K ⁻¹ |

| | |
|---------------|--|
| r_b | distance from body axis to body surface, cm |
| r_s | distance from body axis to shock front, cm |
| $(SL)_\alpha$ | signal loss due to absorption, dB |
| $(SL)_t$ | total signal loss, dB |
| S | entropy, erg-mole ⁻¹ |
| s | distance along streamline from shock front, cm |
| T | temperature, K |
| t | time from lift-off, s |
| u | flow velocity, cm-s ⁻¹ |
| \bar{V} | effective ionization energy, eV |
| X_i | mole fraction of alkali species |
| x | distance from nose along body axis, cm |
| y | distance from body along normal to body surface, cm |
| Z | compressibility factor |
| α | absorption coefficient or fraction of ionizable species singly ionized |
| Γ_p | power reflection coefficient |
| γ | specific heat ratio |
| γ_e | specific concentration of electrons, mole-g ⁻¹ |
| γ_i | specific concentration of ith species, mole-g ⁻¹ |
| Δ | value of y at shock front for a given value of x/d_N , cm |

| | |
|------------------------|--|
| δ | distance to edge of boundary layer, cm |
| δ_m | effective boundary-layer thickness for merged profile, cm |
| δ^* | boundary-layer displacement thickness, cm |
| ϵ | angle between axis and tangent to shock wave, deg |
| $\eta = \sum \gamma_i$ | mole-g ⁻¹ |
| θ_b | angle between axis and tangent to spherical nose, deg |
| θ_c | angle between axis and conical body surface, deg |
| μ | viscosity, g-cm ⁻¹ -s ⁻¹ |
| μ_l | reduced mass of colliding species for <i>l</i> th reaction, g-mole ⁻¹ |
| ν | collision frequency of an electron with other particles, s ⁻¹ |
| ρ | density, g-cm ⁻³ |
| σ_l | cross section for <i>l</i> th reaction, cm ² |
| ω | angular frequency, $2\pi f$, radian-s ⁻¹ |

Subscripts:

| | |
|-----|---|
| abl | ablation material |
| alk | alkali material |
| b | body |
| cr | critical value |
| c | cone |
| e | electron or quantity at boundary-layer edge |

| | |
|----------|---|
| f | endothermic rate direction |
| i | species identification number |
| ns | value at shock front on stagnation streamline |
| o | standard conditions ($p_0 = 1 \text{ atm}$, $T_0 = 273.2 \text{ K}$) |
| p | peak |
| r | exothermic rate direction |
| s | value at shock front on a general streamline |
| ∞ | ambient flight conditions |
| 1,2,3,4 | reflectometer body stations (see table I) |

Special notations:

| | |
|-----|---|
| cr | calculated $N_e = N_{e,cr}$ |
| cr* | Langmuir probe measured $N_e = N_{e,cr}$ |
| tr | transition from laminar to turbulent flow in boundary layer |

Primes denote transformed coordinates and circumflex, a normalized quantity.

RAM C FLIGHT DESCRIPTION

There were three RAM C flights but only the first two are discussed here, since the last one took place after this paper was written. The RAM C payload was a 9° half-angle blunted cone with a nose diameter of approximately 30.5 cm and entered the earth's atmosphere at a velocity of 7.6 km/sec. Figure 1 gives the trajectory of the first two flights. RAM C-I (ref. 7) was a material-addition experiment with water injection at the nose and at side positions. Four communications antennas were also used for passive diagnostic instrumentation. On RAM C-II (ref. 8), the principal effort was on a plasma diagnostic experiment based on 15 reflectometers. There were also four communications antennas. Each payload carried a rake of eight Langmuir probes which extended 7 cm into the aft

flow field in a direction normal to the surface. Table I lists the diagnostic instruments and their locations for the two flights. During the entry data period, the payloads had a spin rate of about 3 rps and a near-zero angle of attack, except for a few short periods where it was as high as 5° .

It might be noteworthy to mention that although both payloads had the same configuration, there were two different ways of protecting the payload from the heat generated at the nose. (See sketch in fig. 1.) In the RAM C-I flight, NARMCO 4028, a phenolic graphite charring ablator, was used at the nose. In the RAM C-II flight for the primary data period 100 to 56 km, a beryllium (Be) nose cap positioned over a teflon ablator allowed reflectometer data to be taken in a clean-air flow. The nose cap was ejected at approximately 56 km; the teflon remained as an ablator at lower altitudes. Both payloads used teflon on the afterbody for heat protection.

An analysis of a sample of the NARMCO 4028 used to fabricate the heat shield showed that it contained about $1100 \mu\text{g/g}$ sodium (Na). The analysis was incapable of detecting potassium (K), if present, at less than $3600 \mu\text{g/g}$ which means that the ablator could have contained up to $4700 \mu\text{g/g}$ of alkali. The Be nose cap and the teflon were found to be free of any significant amounts of alkaline impurities. For a sample of teflon the analysis showed the alkali content to be less than 5 ppm.

THEORY

Clean-Air Flow Field

The techniques described in reference 1 provide a good approximation to the structure of the flow field around a spherically blunted cone such as the RAM payload. Since a knowledge of the electron concentration in the flow field is the major factor in any study involving radio blackout, the ability to calculate the concentration and distribution of the electrons is important. As in reference 1, emphasis is placed on the chemical kinetics and the influence of the boundary layer in computing the properties within the blunt-body flow field. The reader is referred to appendixes A, B, and C for a detailed description of the flow-field calculations.

In the inviscid flow part of the calculations, density, velocity, temperature, and gas composition are computed as functions of distance along a streamline. Velocity and density are then used in a mass balance program to obtain y-coordinates for the stream tubes at prespecified x/d_N locations. At altitudes greater than 30 km, boundary-layer corrections to inviscid results are obtained by following streamlines into the laminar boundary layer. The stream-tube method used accounts for the effects on the flow field of boundary-layer displacement, streamline swallowing, and vorticity interaction normal to the flow direction. The effects of finite-rate chemistry on a streamline position and

shock shape are also included. A shortcoming of the method (even with boundary-layer corrections) is an inability to include the effects of electron-ion diffusion. This effect, as will be shown later, is not negligible for N_e profile peak values for RAM C at altitudes greater than 70 km.

Contaminated Boundary Layer

Ablation from the RAM C-I heat shield of materials known to contain easily ionized impurities such as sodium (Na) and potassium (K) made it necessary to account for an expected increase in electron concentration in the boundary layer. Appendix D gives the details of the calculation along with typical electron concentration profiles useful for comparing with RAM C-I flight data. Alkali ionization is assumed to be decoupled from the air-ablation chemistry and is in equilibrium with the local nonequilibrium thermal properties of the air boundary layer as determined previously. No calculations have been made for the air-teflon boundary layer, for reasons to be discussed later.

RESULTS

Comparison of Data With Plasma Calculations

Values at the peaks of pure air N_e profiles (see appendix A) are plotted in figure 2 as a function of altitude and velocity at body locations appropriate for comparison with data from the RAM C-II flight. Electron concentrations, as derived herein from reflectometer data, are plotted as horizontal bars at values of $N_{e,p} = N_{e,cr}$. (The low-altitude bars are dashed to indicate the presence of uncertainties to be discussed later.) The length of a bar represents the period during which the reflection coefficient changed rapidly. Examples of the region of rapid change in the reflection-coefficient data are shown in figure 3, where reflection-coefficient records from reference 8 are shown with arrows denoting the times for theoretical $N_{e,cr}$, Langmuir-probe-measured $N_{e,cr}$, and where transition from laminar to turbulent flow probably occurred in the boundary layer. The region where body motion was observed is shown as well as the region of fast ablation. (See appendix E and ref. 8.) Figure 4 shows samples of reflectometer phase data similarly marked. Shock-tube tests of the X- and S-band reflectometers in reference 14 indicated that critical N_e was associated with the end rather than with the beginning of the rise to high reflection coefficient (that is, the low-altitude high Γ_p ends of the bars) for the collision frequency range ($\nu/\omega < 1.0$) appropriate to the onset of critical N_e . For high-collision frequency ($\nu/\omega \geq 1.0$), the theoretical indications are that $N_{e,cr}$ occurs at low values of reflection coefficient; thus, for the low-altitude reflectometer decay data, the $N_{e,cr}$ point is expected to be at the low-altitude low Γ_p end of the bars.

In addition to the reflectometer data, the rise of VSWR in the VHF antenna feed circuits is shown in figure 2. Langmuir probe data for the RAM C-II flight (ref. 13) are shown as a cross-hatched area representing envelopes (due to spin and angle of attack) of data for the outermost probe ($y = 7.08$ cm). (The highest ion concentration values measured on each profile were always at the outermost probe.) That part of the Langmuir probe data which is not hatched indicates the altitude range for which probe temperatures were above 812 K. These data may have been affected by thermal degradation of the beryllium oxide insulation. (See ref. 7.) The VHF pattern data in figure 2 represents the altitudes at which the antenna patterns (seen because of vehicle spin) were observed briefly to be circular. (See ref. 15.) The analysis in reference 16 for a similar antenna array indicates that the occurrence of a circular pattern is a definite and sharp indicator for the condition $N_{e,p} = N_{e,cr}$. This observation is an excellent check on the other diagnostic data. Signal attenuation data for X-band, C-band, and VHF frequencies for the RAM C-II flights are converted to $N_{e,p}$ values for display in figure 2 by using the plane-wave nonhomogeneous plasma model given in reference 17. This conversion is done by first assuming a generalized profile shape (as a function of altitude) and arbitrarily letting the N_e magnitude vary. Values of $N_{e,p}$ are then found whose profiles yield theoretical attenuations equal to the measured attenuations. The N_e profile shapes assumed in this method are similar to those found in appendix A.

Values at the peaks of the air plus alkali N_e profile curves (see appendix D) are plotted in figure 5 as a function of altitude and velocity for x/d_N of 2.0 and 4.0 and are compared with data from the RAM C-I flight. Curves representing pure air $N_{e,p}$ are also shown. Langmuir probe data (ref. 7) are shown as a cross-hatched area representing envelopes of data for the outermost probe. In addition to $N_{e,p}$ values derived from attenuation data for X-band, C-band, and VHF frequencies, the rise of VSWR in the VHF antenna feed circuits along with the VHF pattern data are also shown.

Inspection of the theory and flight results in figures 2 and 5 for the altitude regime greater than 60 km brings up some interesting points. (1) There is generally good agreement among the various diagnostic techniques for this altitude range. (2) In view of the agreement of RAM C-I and C-II data, there does not appear to be any effect of alkali ionization at altitudes greater than 65 km. (3) At all body stations and in the altitude range above 71 km, calculated peak N_e values are seen to be much higher than the measured values. However, the theoretical model utilizes the stream-tube concept and hence does not allow for inclusion of effects of electron-ion diffusion or for wall recombination effects.

Estimated correction factors for these effects are obtained by correlating RAM C data with shock-layer solutions from the literature which include diffusion and wall effects. The results are plotted in figure 6. The hatched region is one which includes theoretically

and experimentally determined $N_{e,p}$ reduction factors taken from results of references 18 to 22. This factor is the one by which $N_{e,p}$ for an inviscid profile is reduced because of the effects of viscosity, ion diffusion, and wall recombination. In order to plot the flight data in this figure, they are divided by $N_{e,p}$ values from inviscid curves. All the reference data are for the nose region of blunt-nosed bodies with the exception of reference 19 which is for $x/d_N = 4$. Values appropriate to the stagnation point are generally near the high-altitude side of the hatched region, and values for the nose-body juncture are near the low-altitude side. The reference data are correlated on the RAM C altitude scale on the basis of the rarefaction parameter (used to scale results in ref. 21)

$$k^2 = \frac{\gamma_\infty - 1}{2\gamma_\infty} \frac{(\rho u)_\infty d_N}{2\mu_{ns}} \quad (1)$$

The correlation is seen to be indicative of the effect of ion diffusion and wall effects on the RAM C shock-layer peak N_e . The effects begin at about the altitude predicted ($k^2 \approx 100$).

The comparison between air theory and RAM C-II flight data in figure 2 is reasonably good at altitudes greater than 30 km but less than 60 km. The low-altitude ends of the bars for the X_3 and X_4 reflectometer data are believed to be near the critical electron concentration. (See ref. 14.)

A comparison between the RAM C-I flight data (30 km < altitude < 60 km) and the two sets of theoretical curves (representing air and air plus alkali theories) in figure 5 indicates that the data from the RAM C-I flight correlate better with the contaminated boundary-layer model than with the air model. This condition is true for the lower altitude part of the flight data. Above 50 km, the data drop off where the air plus alkali theory is rising. This drop-off of $N_{e,p}$ is probably due to failure of the local equilibrium assumption in this region (probable delay in production of alkali ions). This figure illustrates that there is a large increase in the electron concentration in the boundary layer due to ionization of alkali impurities from the heat shield of RAM C-I for altitudes less than 60 km. Comparison of flight data (altitude greater than 30 km) in figures 2 and 5 indicates that alkali ionization is probably responsible for the difference in the electron concentration between the RAM C-I and RAM C-II flights.

For comparison of the low-altitude flight data and theory (altitude less than 33.7 km), a velocity scale is used in figures 2 and 5. Table III gives the velocity-altitude pairs used. For the RAM C-I flight, $N_{e,p}$ values were obtained from attenuation data for X-band, C-band, and VHF frequencies by a method previously described. For the RAM C-II flight, $N_{e,p}$ values were obtained from attenuation data for VHF frequencies only, since signal recovery data for X- and C-band were not obtained because of tracking problems. Reflectometer data from RAM C-II are represented in figure 2 by bars as

previously described. The theoretical curves shown in figures 2 and 5 are computed for an air model where any electrophilic effects of teflon ablation into a laminar boundary layer are not considered since the boundary layer is thin relative to the plasma, and reduction of electrons would not appreciably affect $N_{e,p}$. However, calculations are made for a model containing the effects of alkali ablation in a laminar boundary layer (appendix D) since the shock layer $N_{e,p}$ is thus greatly increased.

The data from the RAM C-I flight in figure 5 agree reasonably well with the theoretical curves labeled "air plus alkali," which indicates that the $N_{e,p}$ values are two to three decades higher than the $N_{e,p}$ values computed by use of an air model. This difference is attributed to alkali impurity ionization in the boundary layer. The $N_{e,p}$ values obtained from the VHF attenuation data for the RAM C-II flight agree fairly well with the theoretical air curves in figures 2(d) and 2(e). The reflectometer data bars (fig. 2) do not agree with the theoretical curves. They show a much steeper drop-off of electron concentration than does theory as the payload slows down.

Uncertainties in Theory and Data

Since the low-altitude reflectometer data do not agree well with the plasma theory or deduced VHF data, possible uncertainties in both theory and data should be examined. One source of uncertainty in the theory is in the values of reaction rates used to determine plasma composition. Theoretical curves for pure air are given in figure 7 along with the effects of changing or deleting certain reaction rates. Changing the 15 dissociation reaction rate constants (1 to 15, table II) by factors of 10^1 and 10^{-1} produces $N_{e,p}$ changes as indicated by the hatched region for three of the body locations. The factors for the rate changes are arbitrarily taken and are not intended to indicate that the dissociation rates of O_2 , N_2 , and NO are uncertain by such large factors. Resultant changes in the $N_{e,p}$ level are not large. This result would be expected since reference 23 reported similar equilibrium and nonequilibrium N_e values for the nose flow at 24.5 km (Velocity = 5.12 km/sec) and indicated that N_e was not sensitive to the dissociation rate of O_2 , N_2 , and NO at this altitude. Deleting all reactions which involve O^- and O_2^- causes the electron density to be larger at velocities below 4.5 km/sec for an aft station. Factors of 10^1 and 10^{-1} for the rate constants involving $O^- + M \rightleftharpoons + e^- + M$ and $O_2^- + M \rightleftharpoons O_2 + e^- + M$ gave a change in the $N_{e,p}$ of only 20 percent at a velocity of 3.9 km/sec for the aft body stations. At higher velocities the changes in the rate constant for O^- and O_2^- do not produce any noticeable changes in the $N_{e,p}$ values. The exclusion of NO_2^- and reactions involving this molecule may cause some error in the low-speed calculations. Reference 24, which has equilibrium results for air, reports that NO_2^- becomes a dominating factor in determining the N_e at pressures higher than 1 atmosphere and temperatures less than 4000 K. However, the combination of pressure

and temperature where the reflectometer data are obtained does not match the conditions needed to make NO_2^- important.

One way the air calculation could be appreciably perturbed would be by the combination of large boundary-layer thickening, mixing, and chemical action of the teflon ablation products. The thickening and mixing would presumably occur by the combined effects of transition, increased mass injection, body motion, surface roughness, and so forth. These effects would have to thicken the boundary layer on the nose to ≈ 10 times the computed laminar value for ablation products to reach the required point (outermost point where $N_e \approx N_{e,cr}$) in the inviscid plasma for agreement with reflectometer data. Such large thickening seems unlikely since turbulent boundary-layer calculations show that transition would only cause about a factor of 2 increase in thickness. The maximum blowing parameter for the teflon is theoretically ≈ 0.06 , but the effects of blowing have not been determined. Also, material injection studies have shown it to be difficult to cause even liquids under pressure to penetrate such high density flows; therefore, gaseous ablation products would not be expected to penetrate the flow so deeply. In addition, any large thickening of the boundary layer would move the inviscid plasma out even further because of displacement effects.

The ablation of teflon (ref. 25), a polymer of tetrafluoroethylene (C_2F_4), occurs, sublimation producing the monomer gas. The high-temperature behavior of teflon is discussed in reference 26. Decomposition and oxidation of C_2F_4 in the hot air flow will produce a wide variety of products, some of which are CO , CO_2 , F , CF_4 , CF_2O , CF_3 , CF_2 , and CF . (See refs. 27 to 29 for the chemistry involved.) The structure of the laminar ablating air-teflon boundary layer is given in reference 30.

If the teflon-air products could somehow deeply penetrate the nose-plasma layer, the chemical action required to fit the observations must be either electron attachment or interference with electron production. The computed ablation mass is theoretically about 6 percent of the mass within the required plasma stream tubes. Reference 31 has computed only about 1 percent of the electrons attached for a 5-percent teflon-air equilibrium mixture at about the temperature (6000 K) and density of RAM C-II nose flow in this low-altitude flight regime. Reference 32 has reported no difference in the conductivity between air and air-teflon mixtures (≈ 3 percent teflon in air) behind normal-shock waves where the gas temperature was 3200 K to 6500 K and density on the order of $0.1\rho_0$ to $0.2\rho_0$. It has been shown experimentally in reference 33 that for mixtures of C_2F_4 -air above 3000 K, electron quenching was not obtained.

The agreement of RAM C-I low-altitude data with the alkali theory tends to rule out any large teflon electrophilic action in the boundary layer ($x/d_N > 0.8$) since the body coating injects more teflon into the boundary layer than there are NARMCO products present due to nose ablation. With the teflon present and if attachment of electrons

occurred, then the electron concentration for RAM C-I would not show a large spike (appendix D) in the boundary layer and attenuation data would not agree with the air plus alkali theory.

Although theoretical calculation of attenuation for the RAM C VHF case is not available, some feeling for the possible uncertainties in the interpretation of the VHF attenuation data can be had by examining figure 8 where theoretical plane wave VHF attenuation curves for 226 MHz at $x/d_N = 4$ are compared with recovery data at $x/d_N = 3.8$ for the RAM C-II flight. A curve showing attenuation due to absorption only (a lower limit for plane-wave signal loss) is shown along with a theoretically computed total signal loss curve by using the plane-wave nonhomogeneous plasma model in reference 17. The difference in the level of attenuation between the two curves is due to plasma reflection losses, and to each curve must be added any mismatch losses which may actually be present. (The magnitude of the RAM C VHF mismatch loss is not known.) During the body-motion period, the angle of attack of the vehicle changed by as much as 5° so that calculations of $(SL)_\alpha$ were made at 40.0 km and 30.6 km by using the N_e profiles given in appendix E. The hatched region gives the limits of attenuation in the body-motion period.

Several aspects of figure 8 suggest that the total-signal-loss calculation gives results that are preferred over the absorption-only case. (This statement is not to imply that plane-wave theory is valid for VHF, but merely that the total RAM-C losses due to absorption, reflection, mismatch, etc., happen to amount to something on the order of those calculated by using the plane-wave concept.) First, of course, is the good agreement of the attenuation data with the total-signal-loss values. Second is the fact that VHF recovery did not occur much earlier than observed, as should have been the case if plane-wave absorption were the only losses. In particular, there should have been a substantial recovery lasting for around 4 seconds during the body-motion period. Recovery would not be expected in the case of the higher losses since the reduction during the body-motion period (although not plotted) would be only to about the 40 dB (margin) level.

If one assumes that this total plane wave loss is at least a fair approximation, then the fact that VHF recovery did not occur earlier would rule against the low-altitude $N_{e,p}$ indications given in reference 8, where the faired $N_{e,p}$ curves for the aft stations (as a function of altitude) showed decreasing $N_{e,p}$ below about 37 km. Such a decrease in $N_{e,p}$, along with the increasing ν should result in a decreasing attenuation in the region below 37 km (where the theoretical is increasing), recovery occurring at least 3 seconds earlier than was observed (by 33 km).

For the VHF recovery data to be compatible with the low-altitude $N_{e,p}$ fairing in reference 8 for the RAM C-II flight, large losses, over and above the total-plane-wave losses, would have to be present because of antenna mismatch, and so forth. This condition can be seen from the difference between observed signal loss at recovery given in

figure 8 and that computed for the reflectometer indicated peak N_e profile (by fairing the data in ref. 8, and then using plane-wave theory and maximum plasma thickness to obtain an upper limit case).

Some of the factors which lead to uncertainties in the interpretation of the low-altitude reflectometer data were pointed out in reference 8 and are also discussed in appendix E. The effect of high electron-collision frequency is to make more difficult the interpretation of data from reflectometers for which $\nu/\omega > 1$. Therefore, identification of the point, $N_{e,p} = N_{e,cr}$, from the Γ_p record is subject to a large uncertainty in some cases. Another uncertainty arises because of the long-duration heat pulse of reentry (>20 sec) which causes erosion of the reflectometer dielectric covering. For example, the record for K-band at station 1 in figure 3 shows large oscillations which correspond closely to dielectric thickness changes rather than changes in $N_{e,p}$. Ablation may also be responsible, in part, for the nonideal character of the decay records of S-band at station 1 and X-band at stations 1 and 2. Finally, the sudden decays of reflected power for the X-band records as shown in figure 3 are believed to be associated with transition from laminar to turbulent flow in the boundary layer. Hence, there is an uncertainty in interpretation of the X-band data due to possible effects of changes in profile shape and stand-off distance. An interesting aerodynamic result from this effect is that the transition apparently occurs at a fairly low Reynolds number ($N_{Re} \approx 350\ 000$; see appendix E). This result may also suggest the reflectometer as an instrument for transition measurement.

In summary, much of the low-altitude reflectometer decay data plotted in figure 2 falls well below the plasma theory and the VHF attenuation data. Reasons for the discrepancy apparently cannot be found in terms of the chemical kinetics, boundary-layer thickness, boundary-layer blowing or electrophilic action effects which were used (or neglected) in the development of the plasma theory. The VHF attenuation data, although subject to many questions, seem to corroborate the plasma theory. Several of the reflectometer decays are questionable for indication of $N_{e,cr}$ because of deleterious effects of high collision frequency, ablation, body motion, and possible sensitivity to N_e profile shape.

CONCLUDING REMARKS

For RAM C-I at altitudes below 60 km, the largest values of electron concentration appear to have been present in the boundary layer and were the result of alkali (Na and/or K) present in the NARMCO 4028 phenolic graphite charring ablator used for heat protection on the nose. There was no evidence at any altitude for alkali contamination of the boundary layer for RAM C-II, which had a beryllium nose cap (discarded at 56 km) and was otherwise protected by teflon.

Except for the alkali contamination effects mentioned, electron concentrations computed for clean air gave satisfactory agreement with observations for altitudes between 36 km and 71 km. Divergence between theory and data above 71 km for both RAM C-I and RAM C-II was found to be due to ambipolar electron-ion diffusion and wall recombination. Apparent discrepancies between reflectometer results and calculated values of peak electron concentration below an altitude of 36 km are attributed, at least in part, to effects of high collision frequency, to changes in the thickness of teflon with time, and to effects of laminar-to-turbulent boundary-layer transition. Transition is believed to have occurred at a local Reynolds number of about 350 000.

Langley Research Center,
National Aeronautics and Space Administration,
Hampton, Va., April 7, 1971.

APPENDIX A

CLEAN-AIR FLOW FIELD

In this appendix techniques for computing ionization profiles for blunt-nosed reentry bodies are presented. Emphasis is on careful consideration of the chemical kinetics and of the effects of boundary-layer vorticity interaction. The computations are limited to orbital entry velocity or less and to the case of negligible ionizable ablation impurities. The body considered herein is a 9° half-angle cone blunted with a 30.5-cm-diameter spherical nose, and at zero angle of incidence to the entry flight path.

The method, which includes several machine programs and one hand operation, is tailored for the computation of detailed ionization profiles throughout the supersonic part of the shock layer at many points along the entry trajectory. Basically, the uncoupled stream-tube approach is used, but coupling is achieved, in effect, by iteration of the stream-tube and shock-layer programs. A complete reaction system is employed along the streamlines both in the inviscid-flow region and in the merged boundary-layer inviscid-flow region, but in the latter region the streamline locations and boundary conditions are changed according to the dictates of the boundary-layer solutions and the hand-merging procedure. Although the method used is not fundamentally different from previous methods for blunt bodies with regard to use of the stream-tube technique (ref. 34), boundary-layer swallowing (ref. 19), and boundary-layer merging (ref. 23), some of the innovations employed lead to more precise specification of the ionization profiles. The unique features include the use of finite-rate nonequilibrium shock-layer solutions for determination of shock shape, for location of inviscid streamlines, and for specification of edge conditions for boundary-layer swallowing and merging.

Definition of Inviscid-Flow Field

Figure 9 shows the sphere-cone body and a typical streamline path in the surrounding flow field. A number of methods for finding the details of such a flow field have been published in the literature. In the subsonic region either the direct (ref. 35) or the inverse (ref. 36) approach is used, and the solution is continued in the supersonic region by the method of characteristics. In these methods the gas properties are usually assumed to be either in complete thermochemical equilibrium or to have a frozen composition. The computer time and professional skill required to obtain a complete flow-field solution at one flight speed and altitude is substantial. When finite-rate reactions are included (ref. 37), the required effort goes up tremendously.

The stream-tube approach to finite-rate flow property determination avoids the complexity of the coupled approach by utilizing the streamline paths and boundary

APPENDIX A - Continued

conditions along the streamlines as obtained from equilibrium or frozen flow-field solutions. The error involved in the resulting ionization profiles is usually small, except in the nose regions. In the stream-tube approach used herein, streamline positions are adjusted for the effects of finite-rate chemistry through a shock-layer mass-balance program discussed in appendix B.

Furthermore, the necessity to calculate an equilibrium or frozen flow field for each trajectory point needed can also be avoided, with small error, by utilizing normalized plots of existing solutions. The normalizations which were used to construct inviscid streamline positions and pressure distributions are shown in figures 10 and 11. They were derived from a number of equilibrium and frozen flow-field solutions. (See refs. 36 and 38.) In the forms shown, these parameters are relatively independent of M_1 , θ_c , d_N , and gas properties in the hypersonic regime $15 > M_1 > 30$, in the range of cone angles $6 < \theta_c < 15$, and for the altitude range $20 < \text{altitude} < 70 \text{ km.}$ * Even though computations were made only for a 9° half-angle blunt-cone-shaped body, θ_c is larger than 9° at the higher altitudes where actual cone angles are replaced by larger effective cone angles in order to account for the displacement thickness of the boundary layer.

For a given set of flight conditions pressure distributions were constructed as follows: (1) The shock shape ($\epsilon - \theta_b$ plotted against x/d_N and ϵ/ϵ_c plotted against $\theta_c^2 \frac{x}{d_N}$) and the body pressure distribution (\hat{C}_p plotted against x/d_N and p/p_c plotted against $\theta_c^2 \frac{x}{d_N}$) are found, where θ_c and p_c are sharp-cone values based on M_1 , θ_c , and an assumed specific heat ratio; (2) At given x/d_N the variation of pressure and entropy across the shock layer is found from figure 11. The entropy parameter is used only for determining streamline locations in the shock layer by means of an entropy identification, which is chosen to be the entropy behind the equilibrium shock at its entry point into the shock layer;** (3) The resulting pressure distribution is curve fitted to provide pressure variation along streamlines (fig. 11).

A standard network of flow-field points composed of intersections between 20 numbered streamlines and 20 body station perpendiculars was devised to provide convenient cross-reference points between computer programs and as an aid in plotting results. At the beginning of work for given flight conditions, an initial shock line is plotted. (This line is subject to later modification by mass-flow considerations.) Each of the numbered streamlines originates at the intersection of a body station line with the shock line. Initial conditions on a streamline are obtained by iterating the Rankine-Hugoniot shock

*The upper altitude limit varies with body scale. The limit shown is appropriate for $d_N = 30.5 \text{ cm.}$

**This entropy value is not used for any other purpose because of the nonequilibrium nature of the flow.

APPENDIX A – Continued

equations for a gas of free-stream composition and fully excited internal energy across an oblique shock tangent to the shock envelope at the entry point.

Integration Along Stream Tubes

The next step is to solve the quasi-one-dimensional fluid-flow equations and the finite-rate chemical equations by means of step-by-step integration. These equations are written as follows:

$$\frac{\eta RT}{u_s^2} \left(\frac{1}{\rho_s} \frac{d\rho}{ds} \right) + \frac{\eta \rho RT_s}{\rho_s u_s^2} \left(\frac{1}{T_s} \frac{dT}{ds} \right) + \sum_{j=1}^{13} \frac{\eta_s \rho RT}{\rho_s u_s^2} \left(\frac{1}{\eta_s} \frac{d\gamma_j}{ds} \right) = \frac{1}{\rho_s u_s^2} \frac{dp}{ds}$$

$$\frac{\eta \rho RT_s \left(\frac{c_p}{R} \right)}{\rho_s u_s^2} \left(\frac{1}{T_s} \frac{dT}{ds} \right) + \sum_{j=1}^{13} \frac{\rho \eta_s RT \left(\frac{H_j}{RT} \right)}{\rho_s u_s^2} \left(\frac{1}{\eta_s} \frac{d\gamma_j}{ds} \right) = \frac{1}{\rho_s u_s^2} \frac{dp}{ds}$$

$$\sum_{j=1}^{13} \delta_{ij} \left(\frac{1}{\eta_s} \frac{d\gamma_j}{ds} \right) = \sum_{l=1}^{54} Q_{il}$$

where δ_{ij} is the Kronecker delta. This way of formulating the problem is essentially that described in reference 39, in which the solution of the equations is also discussed. The first and second equations are derivatives of the equation of state and the energy conservation equation, respectively. Substitution of the momentum conservation equation $\frac{du}{ds} = \frac{-1}{\rho u} \frac{dp}{ds}$ eliminated the use of the flow speed. The remaining equations give the production rates of the 13 species.

The composition of the ambient air is assumed to be O₂ (21 percent) and N₂ (79 percent). The species that are considered in the flow are

| Species no. | Neutral species | Species no. | Positive species | Species no. | Negative species |
|-------------|-----------------|-------------|-----------------------------|-------------|-----------------------------|
| 1 | O ₂ | 6 | NO ⁺ | 11 | e ⁻ |
| 2 | N ₂ | 7 | O ₂ ⁺ | 12 | O ₂ ⁻ |
| 3 | O | 8 | N ₂ ⁺ | 13 | O ⁻ |
| 4 | N | 9 | O ⁺ | | |
| 5 | NO | 10 | N ⁺ | | |

APPENDIX A – Continued

The reaction system used in this report is the following:

| Reaction | Dissociation reactions |
|----------|--|
| 1 to 5 | $O_2 + M \rightleftharpoons O + O + M$ |
| 6 to 10 | $N_2 + M \rightleftharpoons N + N + M$ |
| 11 to 15 | $NO + M \rightleftharpoons N + O + M$ |
| | } M = O ₂ , N ₂ , O, N, and NO |
| | Shuffle reactions |
| 16 | $O + N_2 \rightleftharpoons NO + N$ |
| 17 | $O + NO \rightleftharpoons O_2 + N$ |
| | Atom-atom impact (Dissociative recombination) |
| 18 | $O + O \rightleftharpoons O_2^+ + e^-$ |
| 19 | $N + N \rightleftharpoons N_2^+ + e^-$ |
| 20 | $N + O \rightleftharpoons NO^+ + e^-$ |
| | Electron impact (Three-body recombination) |
| 21 | $N_2 + e^- \rightleftharpoons N_2^+ + e^- + e^-$ |
| 22 | $N + e^- \rightleftharpoons N^+ + e^- + e^-$ |
| 23 | $O + e^- \rightleftharpoons O^+ + e^- + e^-$ |
| 24 | $O_2 + e^- \rightleftharpoons O_2^+ + e^- + e^-$ |
| 25 | $NO + e^- \rightleftharpoons NO^+ + e^- + e^-$ |
| | Electron transfer (Direct neutralization) |
| 26 | $O + O \rightleftharpoons O^+ + O^-$ |
| 27 | $O + N \rightleftharpoons N^+ + O^-$ |
| 28 | $O + NO \rightleftharpoons NO^+ + O^-$ |
| | Direct ionization (Three-body recombination) |
| 29 | $N + (O \text{ or } N) \rightleftharpoons N^+ + e^- + (O \text{ or } N)$ |
| 30 | $O + (O \text{ or } N) \rightleftharpoons O^+ + e^- + (O \text{ or } N)$ |

APPENDIX A – Continued

| Reaction | Direct charge transfer for positive ions |
|----------|--|
| 31 | $N_2 + NO^+ \rightleftharpoons N_2^+ + NO$ |
| 32 | $N + NO^+ \rightleftharpoons N^+ + NO$ |
| 33 | $O + NO^+ \rightleftharpoons O^+ + NO$ |
| 34 | $O_2 + NO^+ \rightleftharpoons O_2^+ + NO$ |
| 35 | $N_2 + O_2^+ \rightleftharpoons N_2^+ + O_2$ |
| 36 | $N + O_2^+ \rightleftharpoons N^+ + O_2$ |
| 37 | $O + O_2^+ \rightleftharpoons O^+ + O_2$ |
| 38 | $N_2 + O^+ \rightleftharpoons N_2^+ + O$ |
| 39 | $N + O^+ \rightleftharpoons N^+ + O$ |
| 40 | $N_2 + N^+ \rightleftharpoons N_2^+ + N$ |
| | Electron attachment and deattachment |
| 41 | $O^- + M \rightleftharpoons O + e^- + M$ |
| 42 | $O_2^- + M \rightleftharpoons O_2 + e^- + M$ |
| 43 | $O_2 + e^- \rightleftharpoons O^- + O$ |
| | Rearrangement charge transfer |
| 44 | $O + NO^+ \rightleftharpoons N^+ + O_2$ |
| 45 | $NO + NO^+ \rightleftharpoons N_2^+ + O_2$ |
| 46 | $O + NO^+ \rightleftharpoons O_2^+ + N$ |
| 47 | $N + NO^+ \rightleftharpoons N_2^+ + O$ |
| 48 | $N + NO^+ \rightleftharpoons O^+ + N_2$ |
| 49 | $NO + NO^+ \rightleftharpoons O_2^+ + N_2$ |
| 50 | $N_2 + O^+ \rightleftharpoons N^+ + NO$ |
| 51 | $NO + O^+ \rightleftharpoons N^+ + O_2$ |
| 52 | $N + O_2^+ \rightleftharpoons O^+ + NO$ |
| 53 | $O + N_2^+ \rightleftharpoons N^+ + NO$ |
| | Direct-charge transfer for negative ions |
| 54 | $O_2 + O^- \rightleftharpoons O_2^- + O$ |

APPENDIX A - Continued

The specific rate constants for the molecular dissociation reactions (1 to 15) have the following form (ref. 40):

$$k_{f,l} = N_A \left(\frac{8RT}{\pi \mu_l} \right)^{1/2} \frac{4\sigma_l \left(\frac{D_l T_o}{T} + \frac{1}{2} \right)^{3/2}}{3\pi^{1/2}} \exp \left[- \left(\frac{D_l T_o}{T} + 1 \right) \right]$$

The specific rate constants for the remaining reactions have the form (ref. 41):

$$k_{f,l} = N_A \left(\frac{8RT}{\pi \mu_l} \right)^{1/2} \sigma_l \exp \left[- \left(\frac{D_l T_o}{T} \right) \right]$$

The constants used in these equations are given in table II.

The σ_l values for these reactions are based on information in references 40 and 41 and were adjusted so that the theoretical rate constants would match the best available experimental rate data. The D_l values were obtained from reference 42. In addition to references 40 and 41, some helpful information on reaction rates can be found in references 29 and 43 to 48. All rates are written as forward rates in the endothermic direction. Reverse rates were obtained from the following relationship:

$$k_{r,l} = \frac{k_{f,l}}{K_l}$$

where the values of K_l are computed from the free energy of the species by the use of a polynomial obtained by fitting the data of references 49 and 50 to a set of fourth-order polynomial equations for enthalpy, entropy, heat capacity, and free energy as described in reference 51.

The chemical-rate terms have two forms. For reactions involving three-body recombination (contribution of reaction 12 to production of species 4 is a typical example),

$$Q_{4,12} = \frac{\rho d_N}{\eta_s u} \left(k_{r,12} \rho \gamma_3 \gamma_4 \gamma_2 - k_{f,12} \gamma_5 \gamma_2 \right)$$

For the two-body reactions (contribution of reaction 20 to the production of species 6 is an example),

$$Q_{6,20} = \frac{\rho d_N}{\eta_s u} \left(k_{r,20} \gamma_6 \gamma_{11} - k_{f,20} \gamma_3 \gamma_4 \right)$$

The program written to solve these equations computes and prints results for any desired number of streamlines in sequence. The curves in figure 12 are typical plots of some of the results for a body streamline at an altitude of 47.55 km. The velocity-altitude combinations where calculations were made are given in table III. Information from streamline plots such as figure 12 are used to construct profiles of gas properties.

APPENDIX A – Continued

Profiles of Gas Properties in the Inviscid Flow

Profiles of all the gas properties (ρ , u , T , ν , and p , as well as the concentrations of the species) are found by plotting the values computed at standard network points against y . Initially, y values are found from the normalized plots of figure 11, but these values are improved by means of a computation (see appendix B) which adjusts the y values to ensure conservation of mass flow at the nonequilibrium conditions.

Effect of Boundary Layer on the Electron Concentration Profiles

Although computer programs (ref. 52) for calculating boundary-layer flow properties along hypersonic bodies with coupled finite-rate chemistry have been developed, these programs are all based on the classical boundary-layer problem, for which boundary-layer edge properties change slowly in the flow direction and for which inviscid flow gradients normal to the boundary-layer edge vanish. Such idealized conditions conflict with actual conditions in a thick boundary layer where vorticity due to the curved bow shock is large. Another deterrent to the use of coupled boundary-layer programs for ionized flow-field calculations arises from the mathematical complications introduced by including a large number of finite-rate reactions.

In order to fulfill the need to compute with a reasonably complete reaction system and to be able at the same time to include effects of vorticity interaction, stream tubes from the inviscid region are continued into the boundary layer and the number of matching parameters along the stream tubes are increased from one to three. (This procedure is followed because of the necessity to delete the momentum and energy conservation equations.) Thus, the problem reduces to determination of streamline positions in the boundary layer and of the variation of the additional matching parameters. A three-step procedure is used to find these properties, as described in appendix C.

Electron Concentration Profiles

The effects of applying the procedures described herein are illustrated in figure 13. Curve A is a plot of inviscid stream-tube results against y -coordinates obtained from the mass-conservation program (appendix B). Displacement of curve A by the boundary-layer-displacement thickness led to curve B. The final result, curve C, includes reevaluation of gas composition inside the boundary layer as well as recalculation of y -coordinates in the boundary layer based on merged boundary layer and inviscid profiles (appendix C).

Profile plots of N_e are illustrated in figure 14. For altitudes less than 30 km, the only corrections made for boundary-layer effects were slight displacements in y of the inviscid-flow profiles. It is interesting to note that at altitudes near 40 km, the electron concentration is double-peaked. At higher altitudes the outer peak is dominant,

APPENDIX A – Continued

but at lower altitudes the peak value of N_e lies very close to the body surface. Since collision frequency is nearly constant as a function of distance from the body, a single plot of ν as a function of altitude for four x/d_N locations is given in figure 15. Electron concentration profiles and values of collision frequency are necessary in making attenuation calculations with the plane-wave program of reference 17.

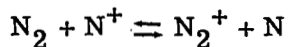
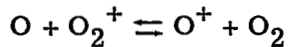
In figure 16, profile peak values of N_e which include boundary-layer effects in the clean-air flow are plotted as a function of velocity and altitude. In the nose flow region, N_e is essentially in local ionic equilibrium except at altitudes greater than 70 km and at velocities less than 4 km/sec. Ionic equilibrium at low altitude is not maintained since velocity falls off rapidly and causes the temperature to be low which, in turn, means that reaction rates fall off. For local ionic equilibrium and with the additional reasonable assumption for RAM C that $\gamma_e = \gamma_{NO^+}$, electron concentration is related to atom concentration by the equation:

$$N_e = \gamma_e N_A \rho = N_A \rho \sqrt{\gamma_N \gamma_O K_{20}}$$

The bulge near 30 km for the aft body locations is due to local ionic equilibrium. For velocities less than 5.5 km/sec and altitudes greater than 40 km, the N_e level on the aft portion of the payload will be determined by the amount of recombination of $NO^+ + e^-$ achieved in the flow time available. These two curves in figure 16 illustrate the effect of varying the rate constant for this reaction. The solid curve represents a reaction rate (ref. 48) which is three times faster than the rate given in reference 41.

The theoretical results from references 23 and 53 are also shown in figure 16. Although the overall agreement is good (comparison should be made with the dashed lines), some mention should be made of the chemistry used in reference 23.

The chemical reactions involving charge transfer that are used in the computations in reference 23 lead to errors in some of the N_e values at 45 km. The only charge transfer reactions used were



These two reactions are ineffective in removing O^+ and N^+ in the aft flow of the body; thus, the electron concentration is equal to the sum of the O^+ and N^+ ion concentration. (See ref. 1 for details.) The total positive atomic ion concentration produced at the nose, although not as large as the NO^+ concentration, does not decrease appreciably during expansion as does the NO^+ concentration. Thus, in the aft flow $O^+ + N^+$ concentrations are greater than that of NO^+ . At lower velocities NO^+ is the primary ion in the entire

APPENDIX A – Concluded

flow field; thus, an incomplete charge-transfer system does not introduce any error. At high altitudes (>75 km) and at the velocity of 7.6 km/sec, all the reactions involving charged species are essentially frozen and the NO^+ ion is the primary ion in the entire flow.

APPENDIX B

MASS CONSERVATION COMPUTER PROGRAM

The sketch in figure 9 should be helpful in understanding the derivation of the mass conservation equations. The basic idea is to equate the mass which flows through a specified area of the shock wave per unit time to a corresponding mass flow further downstream. The mass flow inside the body of revolution generated by rotating about the body axis the streamline whose entry point into the shock front is distant $(r_s)_i$ from the body axis is $\rho_1 u_1 \pi (r_s)_i^2$.

The mass flow between the same body of revolution and the surface of the body at any downstream station (except those close enough to the nose to ensure that the streamlines are not even approximately parallel to the body surface) is $2\pi \int_0^{y_i} \rho u (r_b + y \cos \theta) dy$.

If these two mass flows are set equal to each other, the unknown is y_i , the thickness of the gas layer. In this form the functions $\rho u = \rho u(y)$ and $y \rho u = y \rho u(y)$ must be integrated from the body surface to the streamline in question. The pitfalls inherent in automated curve fitting to obtain the required functions of y were avoided by formulating the problem in terms of increments of y between streamlines. For this procedure the entering mass flow is $\rho_1 u_1 \pi [(r_s)_i^2 - (r_s)_{i-1}^2]$ and the corresponding mass flow

downstream is $2\pi \int_0^{dy_i} \rho u [r_b + (y_{i-1} + y) \cos \theta] dy$.^{*} Let $A_i^2 = (r_s)_i^2 - (r_s)_{i-1}^2$, and

$B_i = \frac{r_b}{\cos \theta} + y_{i-1}$. Then,

$$\rho_1 u_1 A_i^2 = 2 \cos \theta \int_0^{dy_i} \rho u (B_i + y) dy$$

Let $\hat{y} = y/dy_i$, $\hat{\rho} \hat{u} = \rho u / \rho_1 u_1$, $\psi_i = \left(\int_0^1 \hat{\rho} \hat{u} d\hat{y} \right)_i$, and $\phi_i = \left(\int_0^1 \hat{\rho} \hat{u} \hat{y} d\hat{y} \right)_i$. Then,

$$\frac{dy_i}{2B_i} = - \frac{\psi_i}{\phi_i} + \left(\frac{\psi_i^2}{\phi_i^2} + \frac{2}{\phi_i \cos \theta} \frac{A_i^2}{B_i^2} \right)^{1/2} \quad (2)$$

This equation expresses the value of the increment in y , dy_i , between streamlines i and $i - 1$ in terms of the y -coordinate for the preceding streamline y_{i-1} , and the

^{*} When not subscripted, the angle θ may be either θ_b or θ_c .

APPENDIX B – Concluded

integrals ψ_i and ϕ_i . The values of ρ and u are already known at $\hat{y} = 0$ and at $\hat{y} = 1$, because these values are network points. By assuming that $\hat{\rho}\hat{u}$ varies linearly with \hat{y} in the range $0 < \hat{y} < 1$, the integrals can be evaluated as follows:

$$\left(\int_0^1 \hat{\rho}\hat{u} \, d\hat{y} \right)_i = \frac{1}{2} [(\hat{\rho}\hat{u})_{i-1} + (\hat{\rho}\hat{u})_i] \quad (3)$$

$$\left(\int_0^1 \hat{\rho}\hat{u}\hat{y} \, d\hat{y} \right)_i = \frac{1}{2} [(\hat{\rho}\hat{u})_{i-1}] + \frac{1}{3} [(\hat{\rho}\hat{u})_i - (\hat{\rho}\hat{u})_{i-1}] \quad (4)$$

The errors associated with substitution of a broken line for a smooth curve were not evaluated in detail but were estimated to be negligible for the purpose of calculating streamline position in the RAM-C flow field.

APPENDIX C

DETAILS OF BOUNDARY-LAYER TREATMENT

Boundary-Layer Profiles and Displacement Effects

Initial boundary-layer profiles are calculated from laminar similar solutions for an axisymmetric body at zero yaw (ref. 54). The results from these solutions are used in two ways: (a) At each body station the boundary-layer displacement thickness δ^* is added to the y-coordinate of each streamline outside the boundary layer (δ^* is approximate since the computation does not include vorticity), and (b) the profiles of ρu and u are merged with corresponding profiles in the displaced inviscid-flow field. Nonequilibrium edge conditions are used, and the program assumes that boundary-layer gas properties are thermally frozen (that is, no dissociation or recombination of atoms occurs in the boundary layer). This assumption is reasonably good for finding thermal properties (not ionization), as chemical kinetics computations show that very little change in atom concentration occurs in most of the boundary layer aft of the shoulder in the altitude regime where boundary-layer effects are significant. Even near the wall where atom recombination will actually occur, the error is very small, since T and ρ in this region must approach the cold-wall values as specified by the ablation temperature. Use of local nonequilibrium edge properties for the boundary layer gives better results than use of either equilibrium or frozen-flow edge properties (as in a complete blunt-body program), since, in general, processes behind the shock and in the expansion around the body are far from either.

Initial nonequilibrium edge properties are taken from the inviscid body streamline calculations. Then, since the boundary layer is thick, swallowing of the inviscid streamlines into the boundary layer is taken into account in choosing edge conditions along the boundary layer for a repeat calculation. The criterion for swallowing a given streamline is based on equality of the boundary-layer mass flow to the entering mass flow. For stations in the nose region, let $y' = y\left(1 + \frac{y}{d_N}\right)$. Then

$$\rho_1 u_1 \pi (r_s)_i^2 = \pi d_N \cos \theta_b \int_0^{y'} \rho u \, dy' \quad (5)$$

In the region aft of the shoulder, let $y' = y\left(1 + \frac{\cos \theta_c}{2} \frac{y}{r_b}\right)$. Then

$$\rho_1 u_1 \pi (r_s)_i^2 = 2\pi r_b \int_0^{y'} \rho u \, dy' \quad (6)$$

APPENDIX C – Continued

The first use of the boundary-layer solutions is to provide values of δ^* which are added to the body dimensions and thus displace the inviscid shock layer. A plot of the new shock shape is used to provide new starting angles and pressure for the entering streamlines. Also, an effective cone angle and nose diameter are determined which, along with use of the normalized flow-field inputs previously discussed, allows new pressure distributions along the streamlines to be found. The new pressure distributions are used to recompute the inviscid nonequilibrium shock-layer properties and streamline locations, and the whole cycle can be repeated until satisfactory agreement is obtained between input and output shock shape and streamline position.

Merged Profiles

Flow vorticity was accounted for partially in the preceding step, where edge properties were chosen by means of a swallowing criterion. An additional correction for the vorticity normal to the flow direction is obtained by merging boundary-layer profiles with displaced inviscid-flow profiles.

Merging is carried out for the ρu and u shock-layer profiles, and three principal criteria are applied in the merging procedure: (a) mass conservation for the ρu profiles, (b) velocity defect for the u profiles, and (c) smooth transition for both from the displaced inviscid profile (in the neighborhood of $y = \delta$) to the boundary-layer profile (in the neighborhood of $y = \delta^*$). In figure 17(a) where a typical ρu profile has been plotted against the transformed coordinate y' , equality of the shaded areas indicates that the mass flow is the same whether obtained by integrating the merged or the displaced inviscid profile. In addition to respecting the mass-flow criterion, the merged profile is required to blend smoothly into the two original profiles.

Figure 17(b) illustrates the merging of the velocity profiles. The velocity defect inside δ_m (δ_m was determined in step (a)) on the merged profile is made similar to that within the boundary-layer profile. This velocity defect criterion is applied only for the outer region of the profile, since the inner profile must merge into the boundary-layer profile.

Boundary-Layer Stream Tubes and Matching Conditions

The next step in the flow-field determination is to identify "streamline" positions inside the merged boundary layer so that the matching parameters for use in the boundary-layer nonequilibrium stream-tube analysis may be evaluated. This evaluation is made by integrating the ρu against y' merged profiles to find those values of y' within which mass flow equals that of each entering streamline. With streamline positions established in the boundary layer, values of the matching conditions are read from merged plots of ρu and u at each body station. These values, along with the pressure-matching

APPENDIX C – Concluded

parameters (which are assumed to be unchanged from those of the corresponding displaced inviscid streamlines), are used in the boundary-layer version of the stream-tube program. Profiles of species concentration can then be constructed at each body station. It should be pointed out that the specification of p and ρ in the boundary-layer stream-tube analysis is nearly equivalent to specifying the temperature T , within the altitude range where the boundary layer is significant. In this range the composition changes in the boundary layer involve principally electrons and ions, with no significant alteration of the neutral species concentration. Because the chemical kinetics depends strongly on temperature, it is important that the boundary layer and matching conditions be determined by using finite-rate considerations so that the temperature in the boundary layer is correctly specified.

The profiles of electron and ion concentrations which are obtained by these methods do not contain effects of surface recombination or of diffusion of ionic species, and therefore restrict the validity of calculations for the body considered herein to altitudes below about 70 km.

APPENDIX D

EFFECTS OF ABLATION ON ELECTRON CONCENTRATION IN BOUNDARY LAYER

Theoretical estimates are made of the influence on electron concentration of the ionization of NARMCO 4028 ablation products in the RAM C-I boundary layer. These estimates are based on a calculated rate of ablation, on measurements of the ionizable impurities present in NARMCO, on theoretical distributions of air flow and ablation material in the boundary layer, and on assumed local equilibrium ionization of the ablation impurities.

Ablation Gas Flow Rate

The rate at which the surface of the NARMCO nose cap material recedes due to ablation, and the flux of the vaporized and pyrolyzed material into the boundary layer at various stations on the body, has been computed by Ernest V. Zoby of Langley Research Center over the complete entry altitude range for RAM-C. These data were then cross-plotted, at various given altitudes, in the form of \dot{m} , the ablating surface flux, against A , the integrated surface area of the nose cap to the several body stations,

$$A = A(x)$$

The faired plots were then graphically integrated

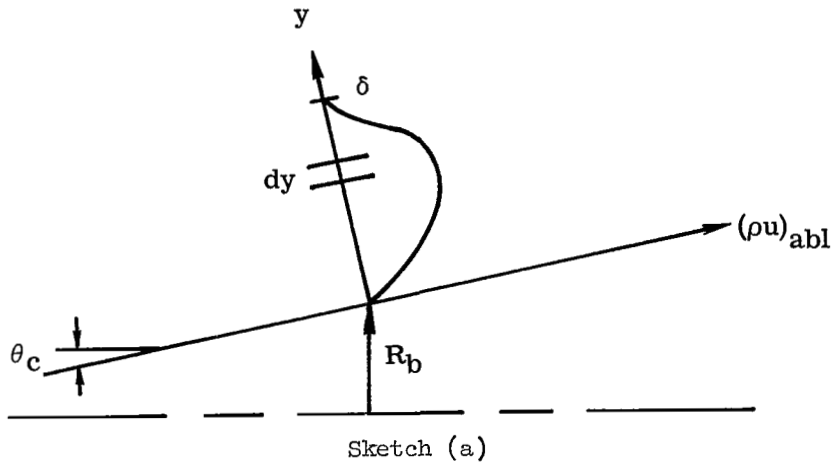
$$m_{abl} = \int_0^x \dot{m} dA \quad (7)$$

to find the ablation flow rate m_{abl} past the body stations $x/d_N = 0.15, 0.422,$ and 0.81 at each of the given altitudes. The resulting values of m_{abl} are plotted as a function of altitude in figure 18. The station $x/d_N = 0.81$ represents the termination of the NARMCO nose cap and the beginning of the teflon body coating. Since only the NARMCO is herein considered as a source of ionizable material, the values for m_{abl} at $x/d_N = 0.81$ are also used for all other downstream body locations. It is seen in figure 18 that the peak ablation rate at $x/d_N = 0.81$ occurs at an altitude of about 25 km.

Ablation Gas Flow Distribution

To determine the distribution of ablation pyrolysis gas flow in the RAM-C flow field, it is first assumed that the ablation gases are confined to the boundary layer, and that the amount of the gases approaches zero at the outer edge. This assumption means that integration of the ablation flow across the boundary layer at a given station must be equal to the value of m_{abl} already determined for that station (see sketch (a)).

APPENDIX D – Continued



$$m_{abl} = \int_{y=0}^{y=\delta} (\rho u)_{abl} 2\pi(R_b + y \cos \theta_c) dy$$

or

$$m_{abl} = 2\pi R_b \int_0^{\delta} \left(1 + \frac{y}{R_b} \cos \theta_c\right) (\rho u)_{abl} dy \quad (8)$$

This expression can be written in terms of a transformed normal coordinate y' as

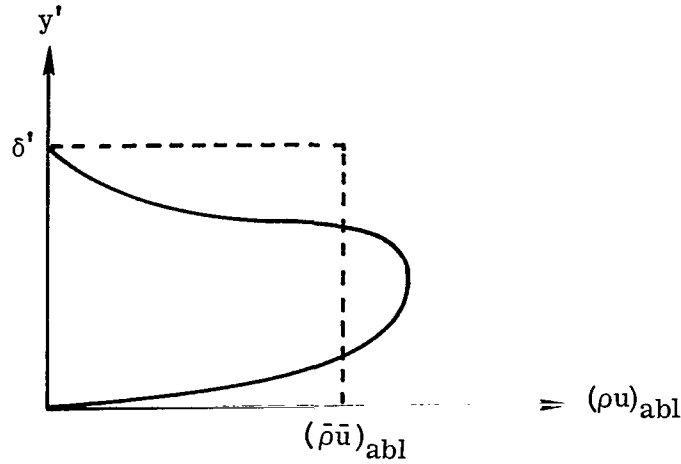
$$m_{abl} = 2\pi R_b \int_0^{\delta'} (\rho u)_{abl} dy' \quad (9)$$

where

$$y' = y \left(1 + \frac{y}{2R_b} \cos \theta_c\right)$$

$$dy' = dy \left(1 + \frac{y}{R_b} \cos \theta_c\right)$$

where the ordinate is proportional to the flow cross-sectional area. If $(\bar{\rho u})_{abl}$ (see sketch (b)) is defined as



Sketch (b)

$$(\bar{\rho u})_{abl} = \frac{\int_0^{\delta'} (\rho u)_{abl} dy}{\delta'} = \frac{m_{abl}}{2\pi R_b \delta'} \quad (10)$$

then

$$\int_0^1 \left(\frac{\rho u}{\bar{\rho u}} \right)_{abl} d\left(\frac{y'}{\delta'} \right) = 1 \quad (11)$$

and plots of $(\rho u / \bar{\rho u})_{abl}$ against y' / δ' , the normalized distribution of ablation gas flow, must have an integrated area of 1.0.

The second principal assumption is that the form of the normalized distribution be generally similar to the form of the velocity defect in the air boundary layer $\left(1 - \frac{u}{u_e}\right)$ plotted against y' / δ' for stations along the nose cap $\left(\frac{x}{d_N} \leq 0.810\right)$ and that for stations downstream of the nose cap, there is a peak in the distribution which moves progressively out from the surface toward the point of maximum shear, the ρu value falling off rapidly at the surface as in reference 55. The latter characteristic reflects the fact that only the NARMCO is considered to be pertinent to the ablation ionization problem. The assumed form which is used herein is shown in figure 19.

By using values of the boundary-layer thickness,

$$\delta' = \delta \left(1 + \frac{\delta}{2R_b} \cos \theta_c \right)$$

and m_{abl} , both at given body stations, the value of $(\bar{\rho u})_{abl}$ is found from equation (10) and values of $(\rho u)_{abl}$ plotted against y can then be found by using figure 18.

APPENDIX D – Continued
Air Boundary-Layer Profiles

The distributions in the air boundary layer of the parameters ρu and u are found by use of a merging technique described in appendix C which partially accounts for vorticity interaction of the boundary layer with the inviscid nonuniform flow field. The technique merges the displaced inviscid-flow profiles with the classical laminar boundary-layer profiles in such a way as to provide a smooth transition from the viscous flow in the inner part of the boundary layer to the inviscid flow at the outer edge of the boundary layer.

The temperature profile in the low-altitude boundary layer $T = T(y)$ is computed by using the merged ρu and u values at a given y -value

$$T = \frac{\rho u}{Z \frac{R}{M_0} (\rho u)} \quad (12)$$

where p , the pressure, is from the RAM-C shock layer solutions, and Z , the compressibility factor, is assumed to vary smoothly (from faired plots) from the nonequilibrium values at the outer part of the boundary layer to a value of 1.0 at the wall ($y = 0$). This method to obtain temperature was used at low altitudes where there are not enough streamlines in the boundary layer to define an accurate temperature profile. It is seen from equation (12) that the value of T becomes zero or indeterminate near the wall for body stations greater than $x/d_N = 0.81$. This result presents no particular problem, however, because the wall is assumed to be at 1000 K and T is simply faired toward this value. The arbitrariness is not important since no significant ionization of the ablation impurities occurs at the lower temperature ($T \leq 1500$ K).

The use of laminar boundary-layer theory in the merging technique is believed to be generally appropriate for these ablation calculations. The transition from laminar to turbulent flow at the $x/d_N = 0.81$ station is not expected to start above an altitude of about 28 km. At lower altitudes, only the thickness and distribution of ablation is in error, since the ablation rate calculations included the effects of turbulent flow. The resulting error in calculated radio signal attenuation is not known but may be small because of the compensating effects of larger thickness but lower $(\rho u)_{abl}$ values (lower N_e) for turbulent flow. (See eq. (10).)

Ionization of Ablation Gas in Boundary Layer

In order to determine meaningful estimates of the ionization within reasonable limitations on computing effort, several simplifying assumptions are employed. It is first assumed that the ionization is due solely to the alkali impurities known to be present in NARMCO. This assumption is probably good, since these impurities are present in amounts at least to 10^{-3} , by weight, and the ionization potential for the alkalis is very

APPENDIX D - Continued

much lower than that of other species expected to be present. Reference 56 gives the species that would be expected in the boundary layer when a phenolic carbon heat shield ablates. The second assumption is that the pyrolysis gases injected into the boundary layer contain these alkali impurities to the same extent as the virgin NARMCO material which was tested. The validity of this assumption is not known. The third assumption is that the ionization of the alkali impurities is in local equilibrium with the nonequilibrium air-ablation gas mixture in the boundary layer. This last assumption would be expected to be reasonably good for blunt-nosed bodies at low altitudes where large numbers of gas collisions occur in the flow field. However, at intermediate and high altitudes, the local equilibrium assumption would become progressively worse since there would not be time for recombination of electrons and ions in the expanded flow at intermediate altitudes, and, at the higher altitudes, there would be a lack of equilibrium ionization in the nose region as well. On the other hand, theoretical nonequilibrium calculations (ref. 56) for the ablation-air mixture would be subject to great uncertainty due to lack of knowledge with respect to the reaction rates for the many possible reactions. Because of the large computing effort required for nonequilibrium calculations, and the other uncertainties involved in the boundary-layer calculations, the local-equilibrium assumption is used for simplicity, its limitations being recognized for later quantitative comparison with flight data.

The three flow parameters which are needed for the calculations are $\frac{(\rho u)_{abl}}{(\rho u)_{air}}$, p/p_0 , and T . These parameters have already been discussed, but it should be pointed out that $\frac{(\rho u)_{abl}}{(\rho u)_{air}}$ becomes indeterminate at $y \rightarrow 0$, for the body stations beyond $x/d_N = 0.81$. This problem is only academic because near the wall the ionization is well below the peak and is falling rapidly toward very low values.

The Saha equation is used to compute the ionization of the boundary-layer mixture,

$$\frac{\alpha^2}{1 - \alpha} = \frac{N}{\sum X_i \frac{p}{p_0}} = \frac{\log^{-1} \left(2.5 \log T - 5040 \frac{\bar{V}_i}{T} - 6.49 + \log G \right)}{\sum X_i \frac{p}{p_0}} \quad (13)$$

where G , the degeneracy factor, is assumed to be 1 and hence the term drops out. A value of 4.85 eV is used for \bar{V}_i , the ionization potential, and represents a value between that for pure Na and pure K. The parameter $\sum X_i$ represents the mole fraction of the ionizable (alkali) species and is computed from

$$\sum X_i = X_{abl} \sum \frac{X_{alk}}{X_{abl}} \quad (14)$$

where

$$X_{abl} = \frac{\frac{X_{abl}}{X_{air}}}{1 + \frac{X_{abl}}{X_{air}}} = \frac{\frac{(\rho u)_{abl} \left(\frac{M_{air}}{M_{abl}} \right)}{(\rho u)_{air} \left(\frac{M_{abl}}{M_{abl}} \right)}}{1 + \frac{(\rho u)_{abl} \left(\frac{M_{air}}{M_{abl}} \right)}{(\rho u)_{air} \left(\frac{M_{abl}}{M_{abl}} \right)}} \quad (15)$$

and

$$\sum \frac{X_{alk}}{X_{abl}} = \sum \left(F \frac{M_{abl}}{M_{alk}} \right)_i \quad (16)$$

Combining equations (14), (15), and (16) and substituting the values for the various molecular weights gives

$$\sum X_i = \frac{0.7 \frac{(\rho u)_{abl}}{(\rho u)_{air}} \sum F_i}{1 + 3.5 \frac{(\rho u)_{abl}}{(\rho u)_{air}}} \quad (17)$$

where $M_{alk} = 30$, a value between that of Na and K, was used; $M_{air} = 21$, a value corresponding to an overall average for the air boundary-layer flow; $M_{abl} = 6$, a value arbitrarily assumed since the composition of the NARMCO was not known.

By using values of $\sum F_i$ and values of $\frac{(\rho u)_{abl}}{(\rho u)_{air}}$ plotted against y , the values of $\sum X_i$ plotted against y can be obtained by use of equation (17). Then α plotted against y can be obtained by use of equation (13). The electron mole fraction and electron concentration are then obtained, respectively, from

$$X_e = \alpha \sum X_i$$

$$N_e = \frac{7.35 \times 10^{21} \left(\frac{p}{p_0} \right) X_e}{T}$$

The resulting computations of N_e plotted against y for the ablation impurity ionization in the RAM-C boundary layer show large effects due to the NARMCO ablation,

APPENDIX D - Concluded

as is seen by the examples shown in figure 20. Diffusion effects were not included in obtaining the N_e profiles since they are not believed to influence $N_{e,p}$ significantly for these nondissipative blunt-body boundary layers at low altitude. Calculations were made for x/d_N locations which bracket RAM C-I flight data.

APPENDIX E

INTERPRETATION OF LOW-ALTITUDE REFLECTOMETER DATA

It was pointed out in reference 8 that determination of the flight time at which the peak N_e at a given body station goes through the critical value is made by using the sudden rise or decay of reflection coefficient. Although this concept was shown to be straightforward for the high-altitude data, it was pointed out that for low altitudes there were uncertainties due to high collision frequency, rapid erosion of the heat shield, body motion, antenna detuning, and so forth. Several of these factors are discussed further.

Heat-Shield Erosion

In figure 3, which shows the reflection coefficient data, as given in reference 8, the regions of fast ablation are indicated. Some ablation occurs prior to and subsequent to these times but the rates are much lower. The total changes in teflon thickness occurring during the times shown for body stations 1 to 4 are 1.9, 0.47, 0.29, and 0.23 cm, respectively, according to calculations made by Ernest V. Zoby of Langley Research Center. The free-space wavelengths for the K-band, X-band, S-band, and L-band reflectometers are 0.86, 3.0, 9.0, and 27 cm, respectively. Effects due to thickness change for the K_1 reflectometer are shown in figure 21 where the calculated rate of change of thickness, normalized to the peak rate, is compared with the normalized observed frequency of the $K_1 \Gamma_p$ oscillations which are seen in figure 3(a).

The close correspondence between the two parameters shows that the reflection coefficient for this reflectometer depended strongly on teflon thickness, since several swings of Γ_p from values near 1.0 to values near 0 are seen to occur during the ablation period but within a period when the plasma is maintained far above the critical N_e . Note that the Γ_p swings occurring prior to the fast ablation period are for a calculated change of only 0.18 cm in ablation thickness, during which time the plasma is well above critical N_e . It is also interesting to note that the magnitude of the Γ_p swings decreases to a relatively small value at about the time when the plasma $N_{e,p}$ falls through the critical value according to the plasma theory. There are similar swings, or bumps, but of lower magnitude and frequency, seen on some of the other records during the fast ablation period. For example, the bumps in X_1 , S_1 , and X_2 superimposed on the decay region of the records make determination of the actual decay very uncertain. One could sketch in any number of possible shapes which might exist in the absence of ablation, as shown by the dashed shapes inserted in figures 3(a) and 3(b).

APPENDIX E – Continued

Body Motions

There was a brief period during the low-altitude part of the RAM C-II reentry that the vehicle went from an angle of attack of around 1° to values as high as 5° . This body-motion period is seen in figure 22 and is from about 414.0 to 418.5 seconds, or from an altitude of about 38 to 30 km. In order to make estimates of the changes in N_e during this period, an approximate flow-field theory was employed. For reflectometer stations 2, 3, and 4, it was assumed that the flow conditions along the most windward and most leeward rays of the conical body at angle of attack could be approximated by computing axisymmetric flow fields for 14° and 4° half-angle sphere cones, respectively, to examine the case of an angle of attack of 5° . For station 1, conditions at angle of attack were approximated from the zero angle case by computing for stations 5° forward and aft of the actual body station angle (angle between body axis and line from sphere center to body station). The computed peak electron concentrations at each body station for altitudes of 30.7 and 40 km, which approximately bracket the body-motion region, are shown in figure 23. The hatched area is the resulting estimated swing in $N_{e,p}$ between the windward (upper) and leeward (lower) limits due to spin at an angle of attack of 5° during the body-motion period. The N_e profiles for the 14° and 4° cases are shown in figure 24.

It can be seen that for some of the body stations, a large change in peak electron concentration is predicted at angle of attack as the measurement point on the body goes from leeward to windward during each body rotation (spin rate of several times per second). Also the profile shape changes from leeward to windward. For the station 1 case in figure 23, the $N_{e,p}$ change is not so large and this, along with the fact that the N_e level is far above the critical values for the reflectometers, would suggest little, if any, oscillation of the reflection coefficient records due to N_e change during the body-motion period. Little change was observed.

For station 2, a fairly large oscillation of Γ_p is suggested for K-band, since N_e swings through critical, and this oscillation is indeed seen (fig. 23). However, changes in N_e profile shape can also produce changes in Γ_p and hence cannot be separated from the $N_{e,p}$ effects. The other frequencies show a small but discernible effect during the body-motion period as might be expected since the N_e values remain substantially higher than critical. However, for stations 3 and 4 there is a very large swing of theoretical peak N_e due to body motion and for X-band, in particular, where the swing is through critical N_e , very large effects on reflection coefficient were observed. Note that the hatched region also goes above K-band critical for about 2 seconds near the end of the period, but it must be recalled that the hatched band corresponds to an angle of attack of 5° throughout the body-motion period. As seen from figure 22, the angle is below 5° during this 2-second time so that K-band effects due to $N_{e,p}$ are not really

APPENDIX E – Continued

predicted. S-band effects are somewhat smaller since the swing is not through critical, and since the spatial changes in profile shape are a smaller fraction of a wavelength.

Boundary-Layer Transition

Careful inspection of the reflection-coefficient records in figure 3 shows that in each of the four X-band records, one very sharp decay of reflection coefficient occurs which is qualitatively unlike the decays in the other instruments. (The K_2 record is discussed later.) That is, these decays are very sharp, nearly discontinuous, even on the time-amplified records given in reference 8. The times at which these sudden decays occur for stations 1 to 4 are 420.5, 419.3, 418.1, and 415.6 seconds, respectively. The sudden decay on X_2 is only different from the other three in that the Γ_p does not drop all the way to a near-zero value. Another way of noting the uniqueness, or suddenness, of these decays is to compare them with the slopes of the S-band and L-band decays, or – more dramatically – with the slope of the X_2 final decay, which is significantly less steep. (See time-amplified records of ref. 8.)

It is interesting to compare the altitudes at which these sudden decays occur with those altitudes at which boundary-layer transition would occur based on a local Reynolds number criterion of 350 000. This value is the value assumed by Zoby in making estimates (believed to be conservative) of the RAM-C heating rates. The comparison is shown in figure 25 where it can be seen that very good correlation is obtained. This correlation is believed to be a strong indication that these sudden decays of Γ_p are associated with transition. They are not associated with the body motions or fast ablation periods since they occur at progressively different times with respect to these periods, and none occurs exactly at the beginning or end of the periods. The first two decays (X_4 and X_3) occur during the body-motion period and may be somewhat different in character than the last two decays since the instrument rotates a few times in and out of transition when spinning at an angle of attack (because of different flow lengths from stagnation point).

Since the important influence which heat-shield erosion, body motions, and boundary-layer transition can have on the low-altitude reflectometer records has been seen, there remain some questions to be clarified. One question is in regard to the sudden decay of the K_2 reflection coefficient, which occurs neither at the transition time nor very near to the time predicted for critical N_e from the theory. (Note the arrows in fig. 3.) However, it does occur at a time coincident with the end of the body-motion period. It is believed that the decay might be qualitatively explained in terms of body motion and heat-shield erosion as follows: (a) It was previously shown that the K_1 reflection coefficient went down markedly when the surface ablation was only on the order of 0.1 cm (that is, first drop occurring before fast ablation). (b) During the fast-ablation period at

station 2, there is theoretically a thickness change of about 0.47 cm and it is reasonable that approximately 0.1 cm occurs from the start of fast ablation to the end of body motions. (See fig. 3(b).) (c) If, therefore, a large Γ_p oscillation due to body motion is superimposed on a decaying Γ_p due to ablation, it is possible that the Γ_p indication could cease at a time coincident with the end of large body motion. It is seen from K_2 in figures 3(b) and 23(a) that the first Γ_p rise (which occurs at 414.7 sec) is almost exactly at the time predicted from theory which includes body motion. Although the magnitude of the oscillations should probably then increase, because of the general increase in $N_{e,p}$, any drop in Γ_p due to ablation would be working against this increase. At the time when body motion ceases, the Γ_p reduction from ablation may already be quite large. However, this argument is only qualitative based on the assumption that K_2 is generally similar to K_1 in its sensitivity to heat-shield thickness.

There is an important question with regard to the sudden drops in Γ_p which are believed to be associated with transition, since both changes in $N_{e,p}$ and/or profile shape can produce changes in reflection coefficient. A drop in $N_{e,p}$ through critical would certainly result in a drop of Γ_p to a very low value, whereas a shift in the N_e profile shape could cause Γ_p to go through a null point but it would probably not drop to a low value for those cases where the reflectometer is extended to the surface. (See fig. 8 in ref. 8.) Yet there is no conceivable way that the $N_{e,p}$ can fall to near critical, for example, at transition for station 1. Before transition the laminar boundary-layer thickness at this location is theoretically about 0.15 cm, and the plasma is nearly three decades supercritical for the X-band all the way out to the shock wave (about 1.7 cm) as seen in figure 14. Even if the boundary layer was several times thicker after transition and if it is assumed that teflon in the boundary layer is an efficient electrophilic, the peak value of N_e in the inviscid plasma is virtually unchanged. Furthermore, a thickening of the boundary layer due to blowing (the blowing parameter is theoretically about 0.06) or surface roughness would simply move the shock and inviscid plasma further out, with negligible effect on $N_{e,p}$.

There is an additional point which suggests that the large sudden drop in the X_1 record is more likely due to a profile change than to a large drop in $N_{e,p}$. A large drop in $N_{e,p}$ in the region around X-band critical should presumably also show up as a significant drop in the S_1 record since the N_e change was at a level of about 10 times S-band critical and collision frequency was high (that is, Γ_p was not at its highest value). For example, during the body-motion period, there were changes in the S-band records when N_e was supercritical for S-band and swinging about the X-band critical level. These S-band changes were probably not due to profile shifts, because the boundary-layer changes at low altitude are small compared with the S-band wavelength. By the same reasoning, little change would be expected in S_1 if a sudden change occurred in the distance of the N_e profile from the body surface but without any change in $N_{e,p}$.

APPENDIX E - Continued

(This change corresponds to a sudden thickening of the boundary layer for transition from laminar to turbulent flow.) Thus it seems significant that S-band response is missing at the times designated for transition, even though X-band response is large, because the changes in boundary-layer thickness are not negligible compared with the X-band wavelength.

High Electron Collision Frequency

In figure 26 the theoretical effect of collision frequency on the variation of Γ_p with $N_e/N_{e,cr}$ is shown for the X-band reflectometer used at station 1 on RAM C-II. (Similar curves for the X-band reflectometers used at stations 2, 3, and 4 are given in ref. 8.) These calculations are based on a parabolic N_e profile where the $\frac{1}{2}N_{e,p}$ point is located about 1/4 cm from the surface of the vehicle. Although the actual flight profiles are not known, the theoretical profiles shown in figure 14 (including boundary layer) for the low altitudes pertinent to this discussion have $\frac{1}{2}N_{e,p}$ points which are in this general range. In figure 15 it can be seen that the theoretical value of ν for station 1 at the altitude for theoretical $N_{e,cr}$ (approximately 20 km) is about $4 \times 10^{11} \text{ sec}^{-1}$. According to figure 26, the value of Γ_p at $N_e = N_{e,cr}$ is less than 0.01 and at $N_e = 10N_{e,cr}$ is only about 0.1. It is obvious that identification of $N_{e,cr}$ from a record of low-altitude decay of Γ_p for this case would be very uncertain, even within wide limits for $N_{e,p}$. More exact calculations, based on the theoretical plasma profiles, could be made but the large effort would not be warranted merely to show qualitatively the strong effect of collision frequency in the records as discussed here.

It would be interesting if a calculation of Γ_p based on the theoretical plasma profiles and reflectometer characteristics could be made for comparison with all the records. Although it would be possible to make these calculations for the X-band reflectometers, with a considerable effort, they have not been made. As pointed out previously, the profiles used to compute the X-band characteristics in figure 26 and reference 8 are not grossly different from the theoretical plasma profiles at low altitude where the decays occur. Therefore, for the purpose of making at least qualitative comparisons in the decay region for the X-band, values of Γ_p were calculated by using reference 8 and figures 2, 26, and 15. The results are shown in figure 27(a), where the numbers beside the squares are values of $N_e/N_{e,cr}$. It is seen that the only station where the comparison is at all close is at station 2 where the transition apparently did not cause a complete decay of Γ_p as at the other stations.

In order to make similar, but even cruder, comparisons with the S-band and L-band records, a very approximate approach was used. For this purpose the high collision frequency curves in figure 26 and reference 8 for X-band were used in normalized form (Γ_p plotted against ν/ω and $N_e/N_{e,cr}$) for application at the lower frequencies. The

APPENDIX E - Concluded

results are shown in figures 27(b) and 27(c). In spite of the admittedly crude approach used, it is believed that the results serve to illustrate the order of uncertainty in interpretation of the low-altitude results. That is, at low altitudes where $\nu/\omega > 1$, the steep drops in reflection coefficient appear to be associated with changes in $N_e/N_{e,cr}$ between 100 and 10, and between 10 and 1. Thus, the region of steep drop in Γ_p at low altitude does not necessarily include the $N_e = N_{e,cr}$ point, because of the effects of high collision frequency.

In view of the discussions in this appendix, the reflectometer decay bars in figure 2 are shown dashed to indicate these uncertainties, in contrast to the solid rise bars at higher altitudes which are believed to be much more precise indicators of the $N_e = N_{e,cr}$ point.

REFERENCES

1. Evans, John S.; Schexnayder, Charles J.; and Huber, Paul W.: Computation of Ionization in Re-Entry Flowfields. AIAA J., vol. 8, no. 6, June 1970, pp. 1082-1089.
2. Blottner, F. G.: Prediction of Electron Density in the Boundary Layer on Entry Vehicles With Ablation. The Entry Plasma Sheath and Its Effects on Space Vehicle Electromagnetic Systems, Vol. I, NASA SP-252, 1970, pp. 219-240.
3. Sims, Theo E.; and Jones, Robert F.: Flight Measurements of VHF Signal Attenuation and Antenna Impedance for the RAM A1 Slender Probe at Velocities up to 17 800 Feet Per Second. NASA TM X-760, 1963.
4. Raper, James L.; Keynton, Robert J.; and Woodbury, Gerard E.: Detailed Description and Flight Performance of the RAM B Vehicle. NASA TN D-2437, 1964.
5. Cuddihy, William F.; Beckwith, Ivan E.; and Schroeder, Lyle C.: RAM B2 Flight Test of a Method for Reducing Radio Attenuation During Hypersonic Reentry. NASA TM X-902, 1963.
6. Grantham, William L.: Preliminary Analysis of Plasma-Sheath Electron Density Measurements at Entry Velocities. NASA TM X-1035, 1064.
7. Akey, Norman D.; and Cross, Aubrey E. (With appendix A by Thomas G. Campbell; appendix B by Fred B. Beck; and appendix C by W. Linwood Jones, Jr.): Radio Blackout Alleviation and Plasma Diagnostic Results From a 25 000 Foot Per Second Blunt-Body Reentry. NASA TN D-5615, 1970.
8. Grantham, William L.: Flight Results of a 25 000-Foot-Per-Second Reentry Experiment Using Microwave Reflectometers To Measure Plasma Electron Density and Standoff Distance. NASA TN D-6062, 1970.
9. Huber, Paul W.; and Evans, John S.: Theoretical Shock-Layer Plasma Flow Properties for the Slender Probe and Comparison With Flight Results. NASA paper presented at Second Symposium on the Plasma Sheath (Boston, Mass.), Apr. 1962.
10. Cuddihy, William F.; Beckwith, Ivan E.; and Schroeder, Lyle C. (With appendix A by Ivan E. Beckwith, Dennis M. Bushnell, and James L. Hunt; appendix B by Ivan E. Beckwith and Sadie P. Livingston; and appendix C by Ivan E. Beckwith): Flight Test and Analysis of a Method for Reducing Radio Attenuation During Hypersonic Flight. NASA TM X-1331, 1967.
11. Evans, John S.: Charge Recombination on Water Droplets in a Plasma. NASA TM X-1186, 1965.

12. Evans, John S.; and Schexnayder, Charles J., Jr.: Analysis of Theoretical and Experimental Electron Concentrations for RAM B3 Flight. NASA TM X-1412, 1967.
13. Jones, W. Linwood, Jr.; and Cross, Aubrey E.: Electrostatic Probe Measurements of Plasma Surrounding Three 25 000 Foot Per Second Reentry Flight Experiments. The Entry Plasma Sheath and Its Effects on Space Vehicle Electromagnetic Systems, Vol. I, NASA SP-252, 1970, pp. 109-136.
14. Taylor, W. C.: An Experimental Investigation of the Interaction of Plasmas With Antennas. NASA CR-1727, 1970.
15. Crosswell, William F.; and Jones, W. Linwood, Jr.: Effects of Reentry Plasma on RAM C-I VHF Telemetry Antennas. The Entry Plasma Sheath and Its Effects on Space Vehicle Electromagnetic Systems, Vol. I, NASA SP-252, 1970, pp. 183-201.
16. Swift, C. T.; and Knop, C. M.: Equatorial Patterns of an Axially-Slotted Cylinder Coated With a Critically Dense Plasma. IEEE Trans. Antennas Propagation, vol. AP-12, no. 4, July 1964, pp. 498-502.
17. Swift, Calvin T.; and Evans, John S.: Generalized Treatment of Plane Electromagnetic Waves Passing Through an Isotropic Inhomogeneous Plasma Slab at Arbitrary Angles of Incidence. NASA TR R-172, 1963.
18. Lee, Richard H. C.; and Zierten, Thomas A.: Merged Layer Ionization in the Stagnation Region of a Blunt Body. Proceedings of the 1967 Heat Transfer and Fluid Mechanics Institute, Paul A. Libby, Daniel B. Olfe, and Charles W. Van Atta, eds.; Stanford Univ. Press, c.1967, pp. 452-468.
19. Kaplan, B.: The Non-Equilibrium Air Boundary Layer on a Blunt Nosed Body. Doc. No. 68SD227, General Electric Co., Apr. 1968. (Available from DDC as AD 833 789.)
20. Kaegi, E. M.; and McMenamin, D. L., Jr.: Measured and Predicted Air Ionization in Blunt Body Shock Layers. AIAA Paper 69-81, Jan. 1969.
21. Kang, Sang-Wook: Analysis of an Ionized Merged-Layer Hypersonic Flow Over a Blunt Body. CAL No. AI-2187-A-12 (Contract No. NAS 5-9978), Cornell Aeronaut. Lab., Inc., May 1969.
22. Dellinger, T. C.: Computation of Nonequilibrium Merged Stagnation Shock Layers by Successive Accelerated Replacement. AIAA Paper 69-655, June 1969.
23. Webb, H., Jr.; Dresser, H.; Korkan, K.; and Raparelli, R.: Theoretical Flow Field Calculations for Project RAM. NASA CR-1308, 1969.

24. Peng, T. C.; Doane, P. M.; and Fivel, H. J.: Model Optimization of Equilibrium Air Plasmas From 10^{-4} - 10^3 Atm. and 1000 to 10,000^o K. Report G996, McDonnell-Douglas Corp., Mar. 1969.
25. Steg, L.; and Lew, H.: Hypersonic Ablation. Tech. Inf. Series No. R62SD55 - Class I, Missile and Space Vehicle Dept., Gen. Elec. Co., May 1962.
26. Wentink, Tunis, Jr.: High Temperature Behavior of Teflon. Res. Rep. 55 (AFBMD-TN-59-15), Avco-Everett Res. Lab., July 1959.
27. Colwell, J. E.; Wachi, F. M.; and Greene, S. A.: An Investigation of the Tetrafluoroethylene Oxygen Flame. SSD-TR-65-141, U.S. Air Force, Aug. 1965. (Available from DDC as AD 474 126.)
28. Braun, E. R.: Effects of a Fully Catalytic Wall on a Non-Equilibrium Boundary Layer Including Ablation Products. Doc. No. 70SD253, Re-Entry Syst., Gen. Elec. Co., June 1970.
29. Heicklen, Julian: Gas-Phase Chemistry of Re-Entry. AIAA J., vol. 5, no. 1, Jan. 1967, pp. 4-15.
30. Greenberg, Robert A.; Kemp, Nelson H.; and Wray, Kurt L.: Structure of the Laminar Ablating Air-Teflon Boundary Layer. Res. Rep. 301 (SAMSO-TR-68-313), Avco-Everett Res. Lab., Nov. 1968.
31. DeBolt, H. E.; and Port, W.: Thermochemical Equilibrium Studies of Ablative Heat-Shield Materials. RAD-TM-63-27 (Contract AF04(694)-239), Avco Corp., June 7, 1963.
32. Morsell, A. L.: Electrical Conductivity of Shock-Heated Air and Air Plus Teflon Mixtures. Res. Note 20 (Contract No. DA 04-495-AMC-4582), Heliodyne Corp., June 1965. (Available from DDC as AD 476 132.)
33. Starner, K. E.: Evaluation of Electron Quench Additives in a Subsonic Air Arc Channel. AIAA J., vol. 7, no. 12, Dec. 1969, pp. 2357-2358.
34. DeRienzo, P.; Berner, F.; Wood, A. D.; and Teare, J. D.: Effects of Nonequilibrium on the Hypersonic Laminar Boundary Layer. BSD-TDR-63-210), U.S. Air Force, Sept. 1963. (Available from DDC as AD 429 808.)
35. Holt, Maurice: Direct Calculation of Pressure Distribution on Blunt Hypersonic Nose Shapes With Sharp Corners. J. Aerosp. Sci., vol. 28, no. 11, Nov. 1961, pp. 872-876.
36. Lomax, Harvard; and Inouye, Mamoru: Numerical Analysis of Flow Properties About Blunt Bodies Moving at Supersonic Speeds in an Equilibrium Gas. NASA TR R-204, 1964.

37. Hall, J. Gordon; Eschenroeder, Alan Q.; and Marrone, Paul V.: Blunt-Nose Inviscid Airflows With Coupled Nonequilibrium Processes. *J. Aerosp. Sci.*, vol. 29, no. 9, Sept. 1962, pp. 1038-1051.
38. Blick, E. F.; and Francis, J. E.: Spherically Blunted Cone Pressure Distributions. *AIAA J.*, vol. 4, no. 3, Mar. 1966, pp. 547-549.
39. Lomax, Harvard; and Bailey, Harry E.: A Critical Analysis of Various Numerical Integration Methods for Computing the Flow of a Gas in Chemical Nonequilibrium. NASA TN D-4109, 1967.
40. Hansen, C. Frederick: Estimates for Collision-Induced Dissociation Rates. *AIAA J.*, vol. 3, no. 1, Jan. 1965, pp. 61-66.
41. Lin, Shao-Chi; and Teare, J. Derek: Rate of Ionization Behind Shock Waves in Air. II. Theoretical Interpretations. *Phys. Fluids*, vol. 6, no. 3, Mar. 1963, pp. 355-375.
42. Schexnayder, Charles J., Jr.: Tabulated Values of Bond Dissociation Energies, Ionization Potentials, and Electron Affinities for Some Molecules Found in High-Temperature Chemical Reactions. NASA TN D-1791, 1963.
43. McKenzie, Robert L.: An Estimate of the Chemical Kinetics Behind Normal Shock Waves in Mixtures of Carbon Dioxide and Nitrogen for Conditions Typical of Mars Entry. NASA TN D-3287, 1966.
44. Dunn, M. G.: Reaction Rate Constants for Ionized Air. CAL Rep. No. AI-2187-A-1, Cornell Aeronaut. Lab., Inc., Apr. 1966.
45. Wray, Kurt L.: Chemical Kinetics of High Temperature Air. AFBSD-TR-61-32, U.S. Air Force, June 1961.
46. Bortner, M. H.: A Review of Rate Constants of Selected Reactions of Interest in Re-Entry Flow Fields in the Atmosphere. Tech. Note. 484, Nat. Bur. Standards, U.S. Dep. Com., May 1969. (Available from DDC as AD 692 231.)
47. Dunn, M. G.; Daiber, J. W.; Lordi, J. A.; and Mates, R. E.: Estimates of Non-equilibrium Ionization Phenomena in the Inviscid Apollo Plasma Sheath. NASA CR-596, 1966.
48. Dunn, Michael G.; and Lordi, John A.: Measurement of Electron Temperature and Number Density in Shock-Tunnel Flows. Part II: $\text{NO}^+ + \text{e}^-$ Dissociative Recombination Rate in Air. *AIAA J.*, vol. 7, no. 11, Nov. 1969, pp. 2099-2104.
49. Browne, William G.: Thermodynamic Properties of Some Diatomic and Linear Polyatomic Molecules. Eng. Phys. Tech. Memo. #3, Missile Space Vehicle Dep., Gen. Elec. Co.

50. Browne, William G.: Thermodynamic Properties of Some Atoms and Atomic Ions. Eng. Phys. Tech. Memo. #2, Missile Space Vehicle Dep., Gen. Elec. Co.
51. Zeleznik, Frank J.; and Gordon, Sanford: A General IBM 704 or 7090 Computer Program for Computation of Chemical Equilibrium Compositions, Rocket Performance, and Chapman-Jouguet Detonations. NASA TN D-1454, 1962.
52. Blottner, F. G.: Nonequilibrium Laminar Boundary-Layer Flow of Ionized Air. AIAA J., vol. 2, no. 11, Nov. 1964, pp. 1921-1927.
53. Widhopf, G.; Kaplan, B.; and Jannone, J.: Numerical Flow Field Prediction for Project RAM-C. Tech. Rep. No. 605 (Contract NAS1-5519), Gen. Appl. Sci. Labs., Inc., June 30, 1966. (Also available as NASA CR-66109.)
54. Cohen, Nathaniel B.: Boundary-Layer Similar Solutions and Correlation Equations for Laminar Heat-Transfer Distribution in Equilibrium Air at Velocities up to 41 000 Feet Per Second. NASA TR R-118, 1961.
55. Kemp, Nelson H.; and Wallace, James: Distribution of a Trace Element in a Boundary Layer With Mass Transfer. AIAA J., vol. 8, no. 1, Jan. 1970, pp. 81-86.
56. Anderson, Larry W.; and Kendall, Robert M.: A Nonsimilar Solution for Multicomponent Reacting Laminar and Turbulent Boundary Layer Flows Including Transverse Curvature. AFWL-TR-69-106, U.S. Air Force, Mar. 1970. (Available from DDC as AD 867 904.)

TABLE I.- LOCATION OF ONBOARD RADIO FREQUENCY AND ELECTROSTATIC PROBES

| x/d_N (a) | RAM C-I | RAM C-II |
|-------------------------------|--------------------------------------|--|
| 0.15 (45°) (Station 1) | | K-band reflectometer (35 000 MHz) X-band reflectometer (10 044 MHz) S-band reflectometer (3 348 MHz) |
| 0.76 (Station 2) | | K-band reflectometer (35 000 MHz) X-band reflectometer (10 044 MHz) S-band reflectometer (3 348 MHz) L-band reflectometer (1 116 MHz) |
| 2.3 (Station 3) | | K-band reflectometer (35 000 MHz) X-band reflectometer (10 044 MHz) S-band reflectometer (3 348 MHz) L-band reflectometer (1 116 MHz) |
| 2.4 | VHF telemetry slots (259.7 MHz) | |
| 2.6 | X-band telemetry horns (9210 MHz) | X-band telemetry horns (9 210 MHz) |
| 3.2 | | VHF telemetry ring (259.7 MHz) |
| 3.4 | VHF telemetry ring (225.7 MHz) | |
| 3.5 (Station 4) | | K-band reflectometer (35 000 MHz) X-band reflectometer (10 044 MHz) S-band reflectometer (3 348 MHz) L-band reflectometer (1 116 MHz) |
| 3.5 | | C-band beacon horn (5 800 MHz) |
| 3.7 | C-band beacon horn (5700 MHz) | |
| 3.8 | | VHF telemetry ring (225.7 MHz) |
| 3.9 | Langmuir probe rake ^b | |
| 4.0 | | Langmuir probe rake ^b |

^aLocation of center line of component,

d_N = 31.90 cm (12.56 in.) for RAM C-I NARMCO
 = 30.48 cm (12.00 in.) for RAM C-II beryllium
 = 32.13 cm (12.65 in.) for RAM C-II teflon.

^bProbes located at $y = 0.96, 1.84, 2.70, 3.58, 4.46, 5.34, 6.20,$ and 7.08 cm.

TABLE II.- CONSTANTS FOR USE IN REACTION RATE FORMULAS

| l | Reaction | μ_l | D_l | σ_l, cm^2 | l | Reaction | μ_l | D_l | σ_l, cm^2 |
|-----|--|-------------------------|--------|-------------------------|-----|--|-------------------------|--------|-------------------------|
| 1 | $\text{O}_2 + \text{O}_2 = \text{O} + \text{O} + \text{O}_2$ | 16.000 | 217.34 | 14.60×10^{-16} | 28 | $\text{O} + \text{NO} = \text{NO}^+ + \text{O}^-$ | 10.435 | 330.70 | 1.00×10^{-16} |
| 2 | $\text{O}_2 + \text{N}_2 = \text{O} + \text{O} + \text{N}_2$ | 14.934 | 217.34 | 7.75 | 29 | $\text{N} + (\text{O or N}) = \text{N}^+ + \text{e}^- + (\text{O or N})$ | 7.000 | 617.80 | 1.00 |
| 3 | $\text{O}_2 + \text{O} = \text{O} + \text{O} + \text{O}$ | 10.667 | 217.34 | 60.00 | 30 | $\text{O} + (\text{O or N}) = \text{O}^+ + \text{e}^- + (\text{O or N})$ | 8.000 | 578.40 | 1.00 |
| 4 | $\text{O}_2 + \text{N} = \text{O} + \text{O} + \text{N}$ | 9.739 | 217.34 | 6.72 | 31 | $\text{N}_2 + \text{NO}^+ = \text{N}_2^+ + \text{NO}$ | 14.50 | 268.90 | 20.00 |
| 5 | $\text{O}_2 + \text{NO} = \text{O} + \text{O} + \text{NO}$ | 15.484 | 217.34 | 5.00 | 32 | $\text{N} + \text{NO}^+ = \text{N}^+ + \text{NO}$ | 9.55 | 224.80 | 20.00 |
| 6 | $\text{N}_2 + \text{O}_2 = \text{N} + \text{N} + \text{O}_2$ | 14.934 | 414.50 | 10.30 | 33 | $\text{O} + \text{NO}^+ = \text{O}^+ + \text{NO}$ | 10.40 | 185.2 | 20.00 |
| 7 | $\text{N}_2 + \text{N}_2 = \text{N} + \text{N} + \text{N}_2$ | 14.000 | 414.50 | 16.50 | 34 | $\text{O}_2 + \text{NO}^+ = \text{O}_2^+ + \text{NO}$ | 15.50 | 120.20 | 20.00 |
| 8 | $\text{N}_2 + \text{O} = \text{N} + \text{N} + \text{O}$ | 10.182 | 414.50 | 6.45 | 35 | $\text{N}_2 + \text{O}_2^+ = \text{N}_2^+ + \text{O}_2$ | 14.90 | 148.70 | 20.00 |
| 9 | $\text{N}_2 + \text{N} = \text{N} + \text{N} + \text{N}$ | 9.334 | 414.50 | 72.00 | 36 | $\text{N} + \text{O}_2^+ = \text{N}^+ + \text{O}_2$ | 9.74 | 104.50 | 20.00 |
| 10 | $\text{N}_2 + \text{NO} = \text{N} + \text{N} + \text{NO}$ | 14.483 | 414.50 | 7.00 | 37 | $\text{O} + \text{O}_2^+ = \text{O}^+ + \text{O}_2$ | 10.70 | 65.00 | 20.00 |
| 11 | $\text{NO} + \text{O}_2 = \text{N} + \text{O} + \text{O}_2$ | 15.484 | 275.74 | 2.94 | 38 | $\text{N}_2 + \text{O}^+ = \text{N}_2^+ + \text{O}$ | 10.20 | 83.70 | 20.00 |
| 12 | $\text{NO} + \text{N}_2 = \text{N} + \text{O} + \text{N}_2$ | 14.483 | 275.74 | 3.12 | 39 | $\text{N} + \text{O}^+ = \text{N}^+ + \text{O}$ | 7.47 | 39.51 | 20.00 |
| 13 | $\text{NO} + \text{O} = \text{N} + \text{O} + \text{O}$ | 10.435 | 275.74 | 6.06 | 40 | $\text{N}_2 + \text{N}^+ = \text{N}_2^+ + \text{N}$ | 9.34 | 44.19 | 20.00 |
| 14 | $\text{NO} + \text{N} = \text{N} + \text{O} + \text{N}$ | 9.545 | 275.74 | 11.30 | 41 | $\text{O}^- + \text{M} = \text{O} + \text{e}^- + \text{M}$ | 10.00 | 62.48 | 10.00 |
| 15 | $\text{NO} + \text{NO} = \text{N} + \text{O} + \text{NO}$ | 15.000 | 275.74 | 14.80 | 42 | $\text{O}_2^- + \text{M} = \text{O}_2 + \text{e}^- + \text{M}$ | 15.00 | 19.55 | 10.00 |
| 16 | $\text{O} + \text{N}_2 = \text{NO} + \text{N}$ | 10.182 | 138.93 | 2.69 | 43 | $\text{O}_2 + \text{e}^- = \text{O}^- + \text{O}$ | 5.4858×10^{-4} | 155.14 | .10 |
| 17 | $\text{O} + \text{NO} = \text{O}_2 + \text{N}$ | 10.435 | 71.24 | 1.10 | 44 | $\text{O} + \text{NO}^+ = \text{N}^+ + \text{O}_2$ | 10.44 | 282.90 | 20.00 |
| 18 | $\text{O} + \text{O} = \text{O}_2^+ + \text{e}^-$ | 8.000 | 294.85 | .175 | 45 | $\text{NO} + \text{NO}^+ = \text{N}_2^+ + \text{O}_2$ | 15.00 | 188.60 | 20.00 |
| 19 | $\text{N} + \text{N} = \text{N}_2^+ + \text{e}^-$ | 7.000 | 247.27 | .66 | 46 | $\text{O} + \text{NO}^+ = \text{O}_2^+ + \text{N}$ | 10.40 | 178.40 | 20.00 |
| 20 | $\text{N} + \text{O} = \text{NO}^+ + \text{e}^-$ | 7.467 | 117.69 | .076 | 47 | $\text{N} + \text{NO}^+ = \text{N}_2^+ + \text{O}$ | 9.55 | 130.00 | 20.00 |
| 21 | $\text{N}_2 + \text{e}^- = \text{N}_2^+ + \text{e}^- + \text{e}^-$ | 5.4858×10^{-4} | 661.90 | 1.00 | 48 | $\text{N} + \text{NO}^+ = \text{O}^+ + \text{N}_2$ | 9.55 | 46.31 | 20.00 |
| 22 | $\text{N} + \text{e}^- = \text{N}^+ + \text{e}^- + \text{e}^-$ | 5.4858×10^{-4} | 617.80 | 1.00 | 49 | $\text{NO} + \text{NO}^+ = \text{O}_2^+ + \text{N}_2$ | 15.00 | 39.93 | 20.00 |
| 23 | $\text{O} + \text{e}^- = \text{O}^+ + \text{e}^- + \text{e}^-$ | 5.4858×10^{-4} | 578.40 | 1.00 | 50 | $\text{N}_2 + \text{O}^+ = \text{N}^+ + \text{NO}$ | 10.18 | 178.40 | 20.00 |
| 24 | $\text{O}_2 + \text{e}^- = \text{O}_2^+ + \text{e}^- + \text{e}^-$ | 5.4858×10^{-4} | 513.00 | 1.00 | 51 | $\text{NO} + \text{O}^+ = \text{N}^+ + \text{O}_2$ | 10.44 | 97.71 | 20.00 |
| 25 | $\text{NO} + \text{e}^- = \text{NO}^+ + \text{e}^- + \text{e}^-$ | 5.4858×10^{-4} | 393.00 | 1.00 | 52 | $\text{N} + \text{O}_2^+ = \text{O}^+ + \text{NO}$ | 9.74 | 6.80 | 20.00 |
| 26 | $\text{O} + \text{O} = \text{O}^+ + \text{O}^-$ | 8.000 | 516.00 | 1.00 | 53 | $\text{O} + \text{N}_2^+ = \text{N}^+ + \text{NO}$ | 10.18 | 94.74 | 20.00 |
| 27 | $\text{O} + \text{N} = \text{N}^+ + \text{O}^-$ | 7.467 | 555.50 | 1.00 | 54 | $\text{O}_2 + \text{O}^- = \text{O}_2^- + \text{O}$ | 10.67 | 42.93 | 20.00 |

TABLE III.- RAM C TRAJECTORY DATA

| Time from lift-off, sec | Altitude | | Velocity | |
|----------------------------|----------|---------|----------|--------|
| | km | ft | km/sec | ft/sec |
| 426.8 | 19.202 | 63 000 | 3.048 | 10 000 |
| 424.8 | 21.336 | 70 000 | 3.883 | 12 740 |
| 423.3 | 22.860 | 75 000 | 4.572 | 15 000 |
| 422.3 | 23.774 | 78 000 | 5.029 | 16 500 |
| 421.4 | 25.146 | 82 500 | 5.425 | 17 800 |
| 419.4 | 27.999 | 91 860 | 6.218 | 20 400 |
| 418.0 | 30.632 | 100 500 | 6.614 | 21 700 |
| 416.4 | 33.706 | 110 583 | 6.980 | 22 900 |
| 413.1 | 40.000 | 131 233 | 7.391 | 24 250 |
| 409.2 | 47.549 | 156 000 | 7.565 | 24 820 |
| 406.2 | 53.340 | 175 000 | 7.620 | 25 000 |
| 402.0 | 61.570 | 202 000 | 7.651 | 25 100 |
| 397.3 | 71.018 | 233 000 | 7.651 | 25 100 |
| 392.6 | 80.162 | 263 000 | 7.651 | 25 100 |
| 390.2 | 85.040 | 279 000 | 7.651 | 25 100 |

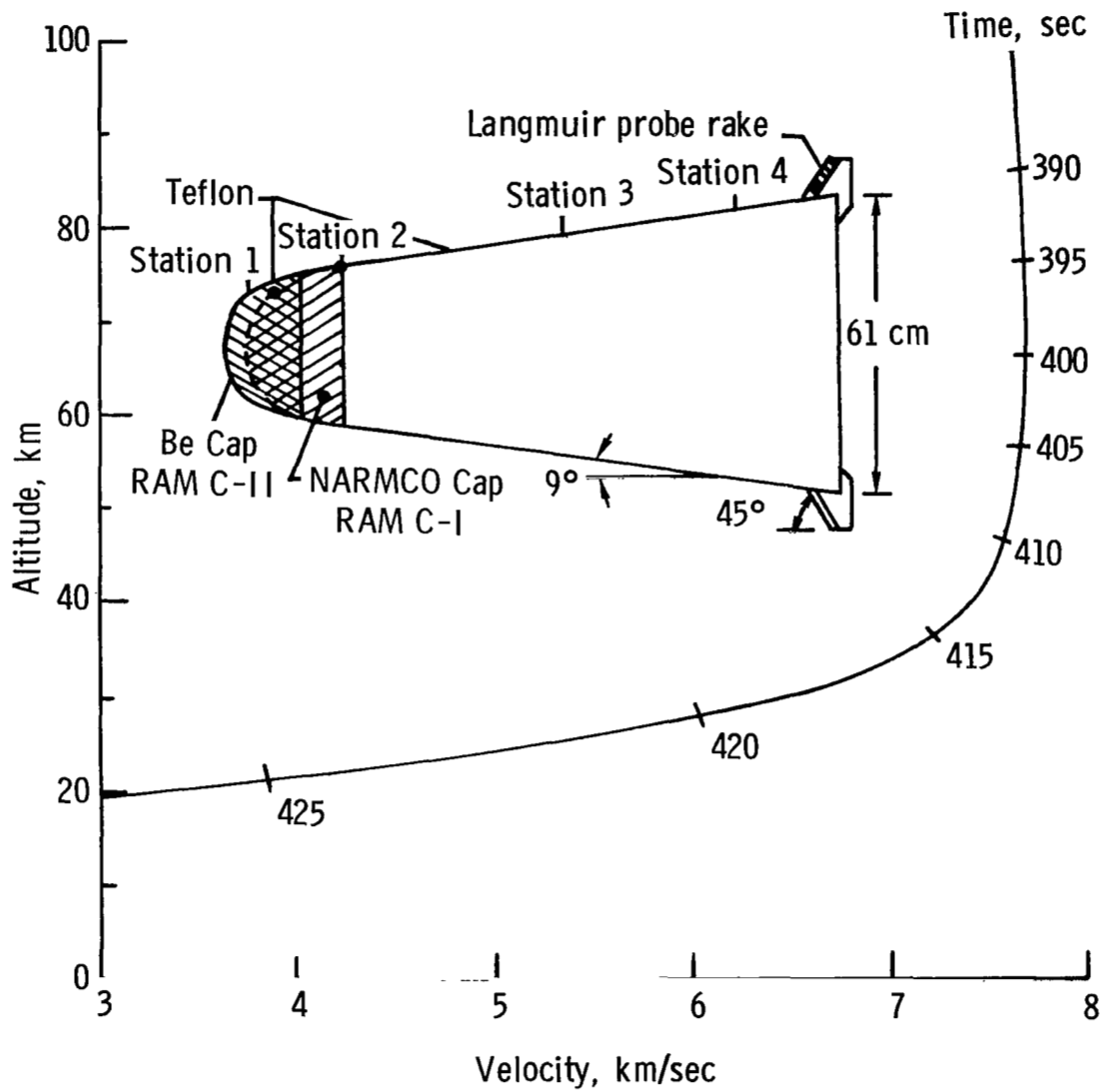
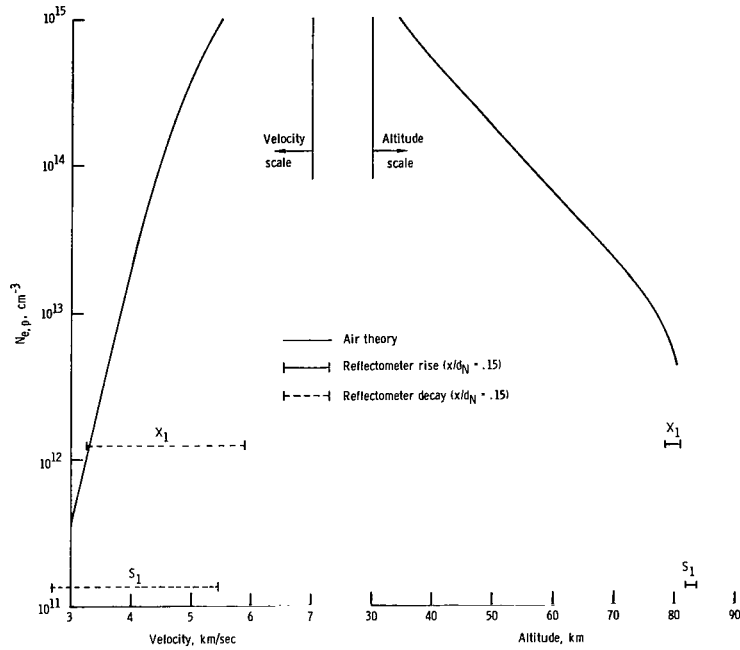
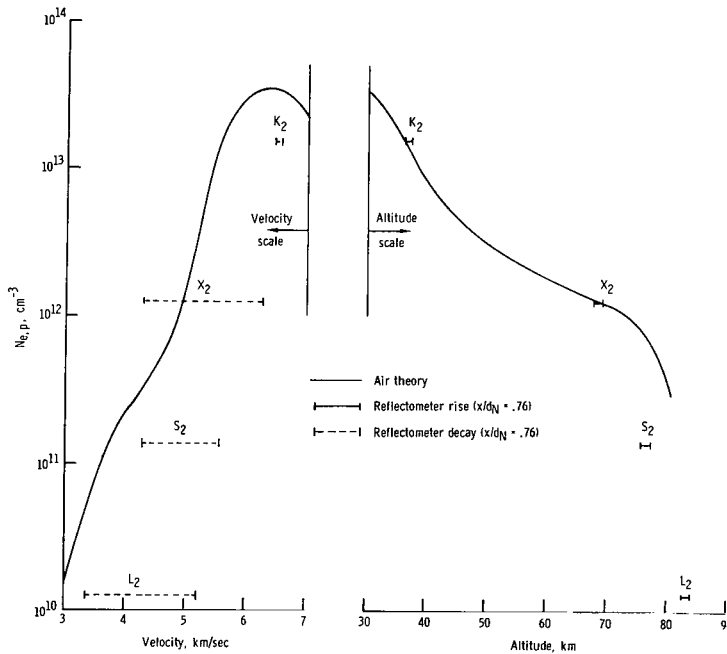


Figure 1.- RAM C configurations and entry profile.

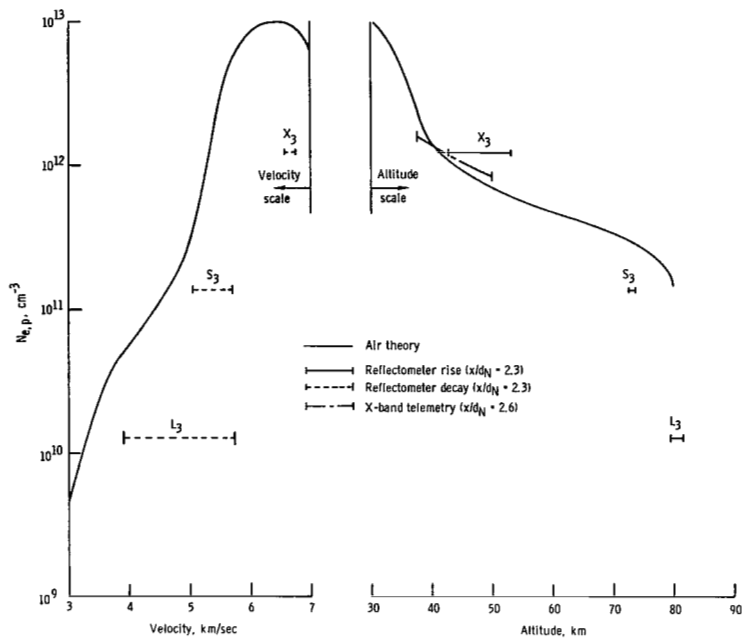


(a) $x/d_N = 0.15$.

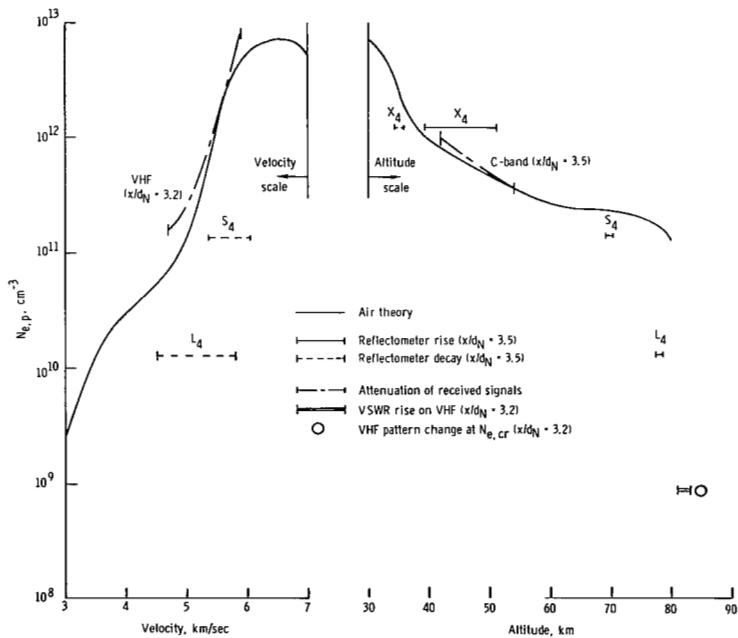


(b) $x/d_N = 0.76$.

Figure 2.- Comparison of peak electron concentration (air theory) with RAM C-II flight results.

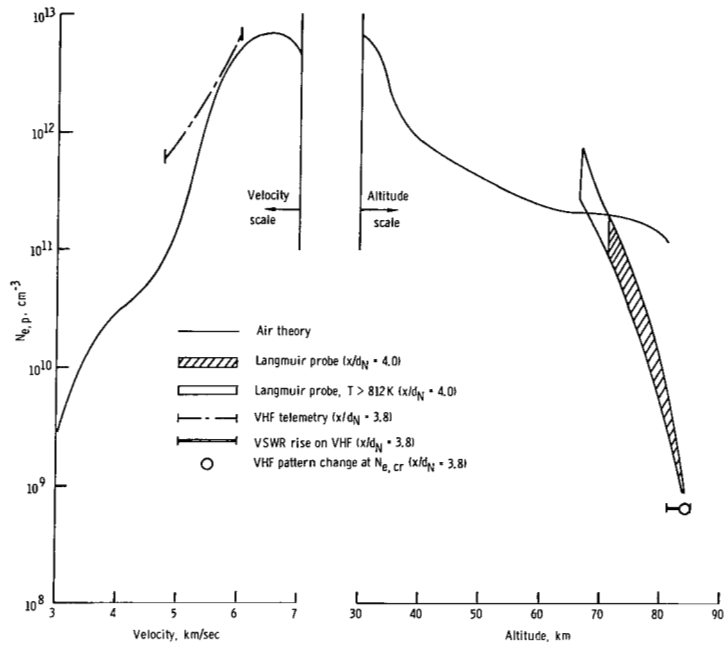


(c) $x/d_N = 2.3$.



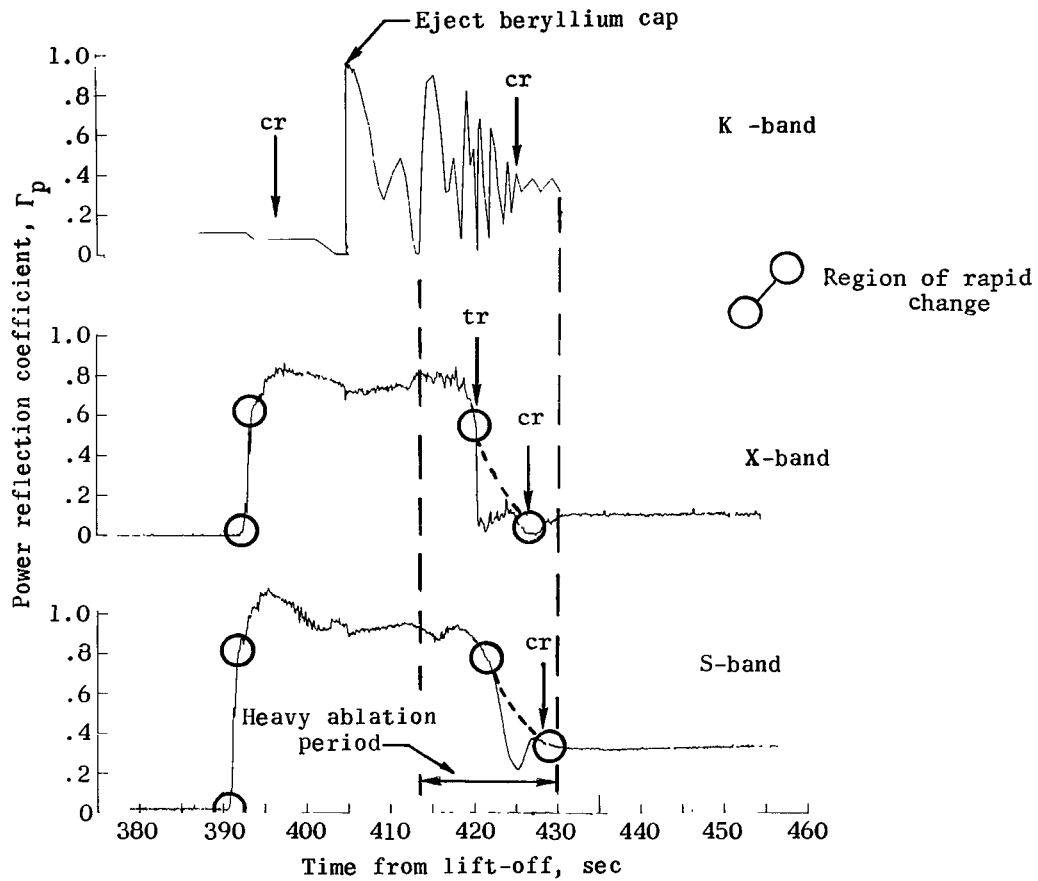
(d) $x/d_N = 3.5$.

Figure 2.- Continued.



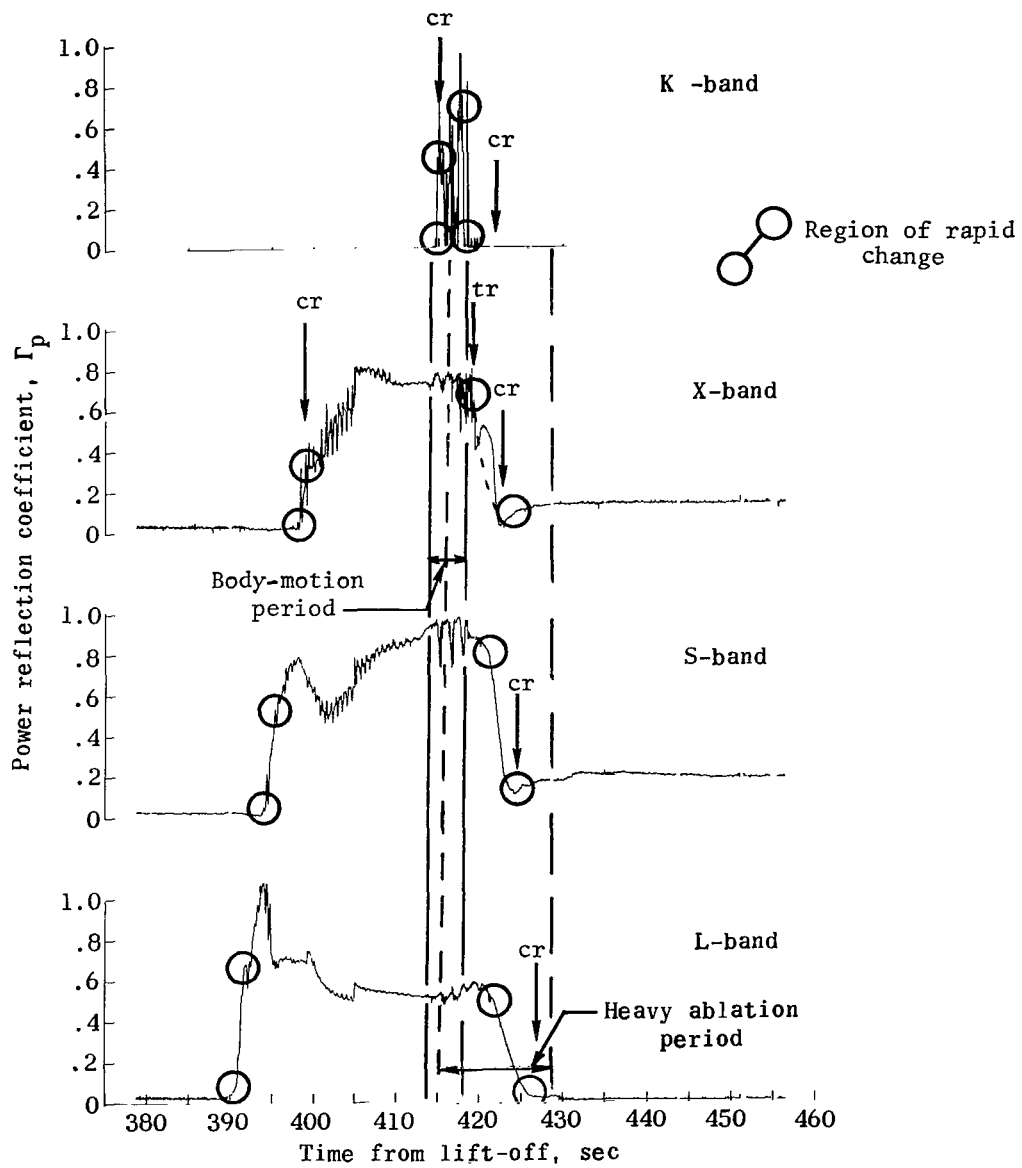
(e) $x/d_N = 4.0$.

Figure 2.- Concluded.



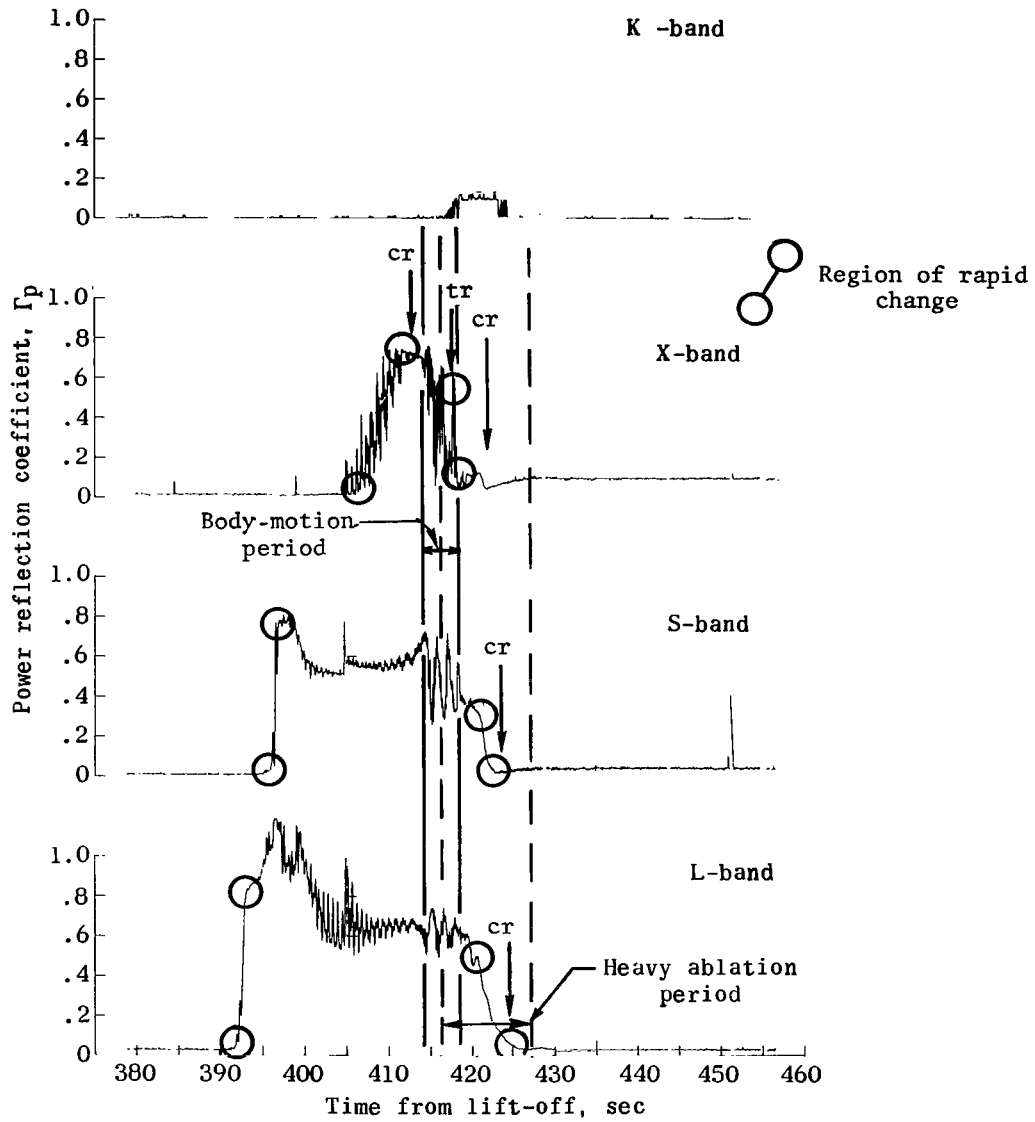
(a) Station 1 ($x/d_N = 0.15$).

Figure 3.- Measured reflection coefficients taken from reference 8.



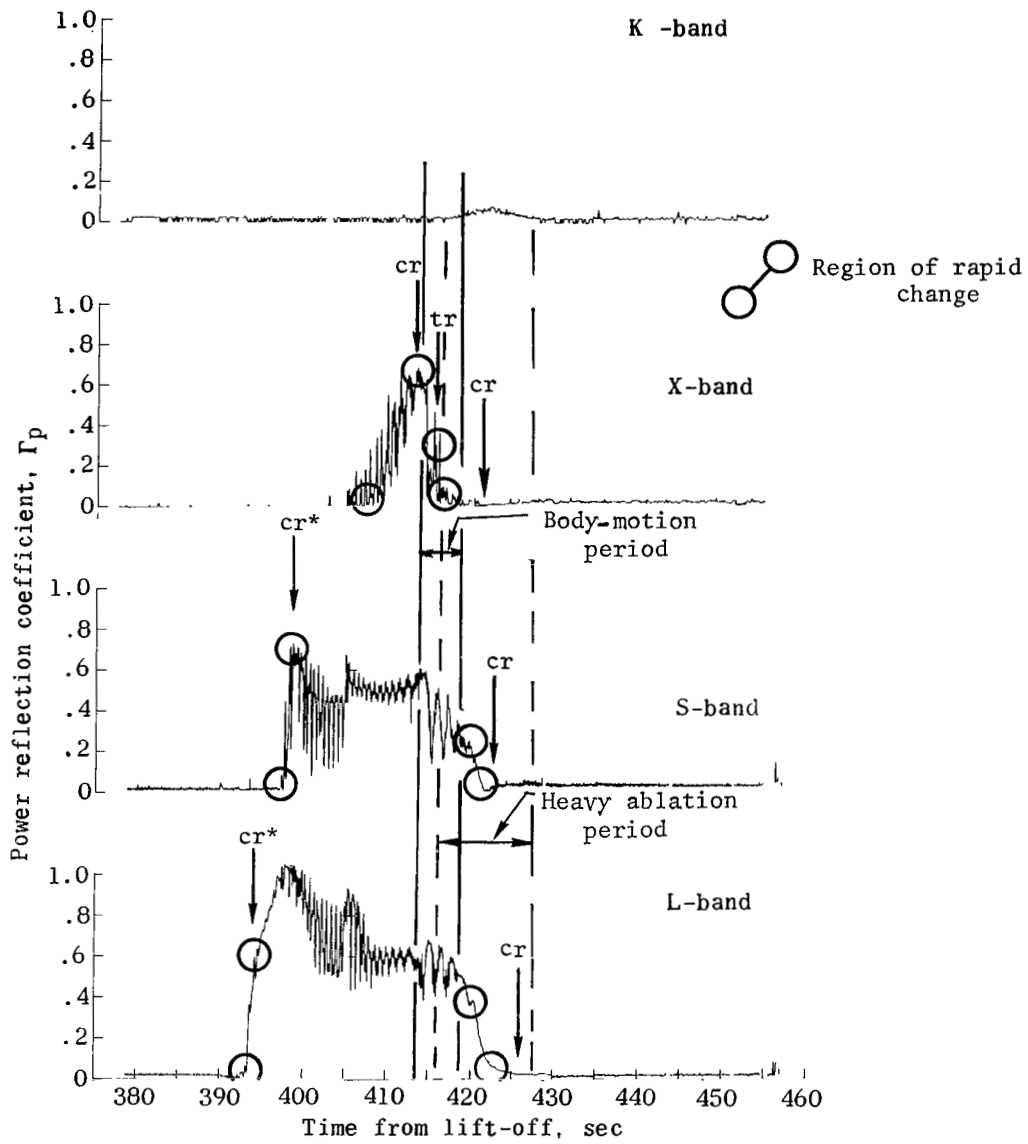
(b) Station 2 ($x/d_N = 0.76$).

Figure 3.- Continued.



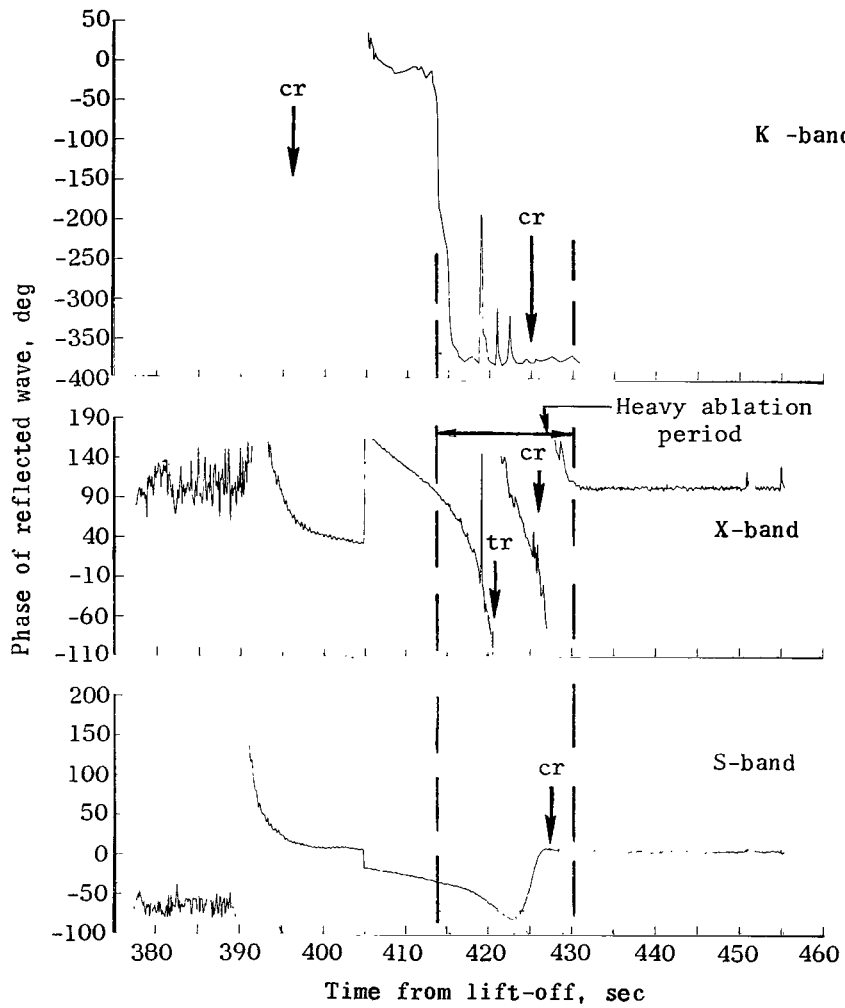
(c) Station 3 ($x/d_N = 2.3$).

Figure 3.- Continued.



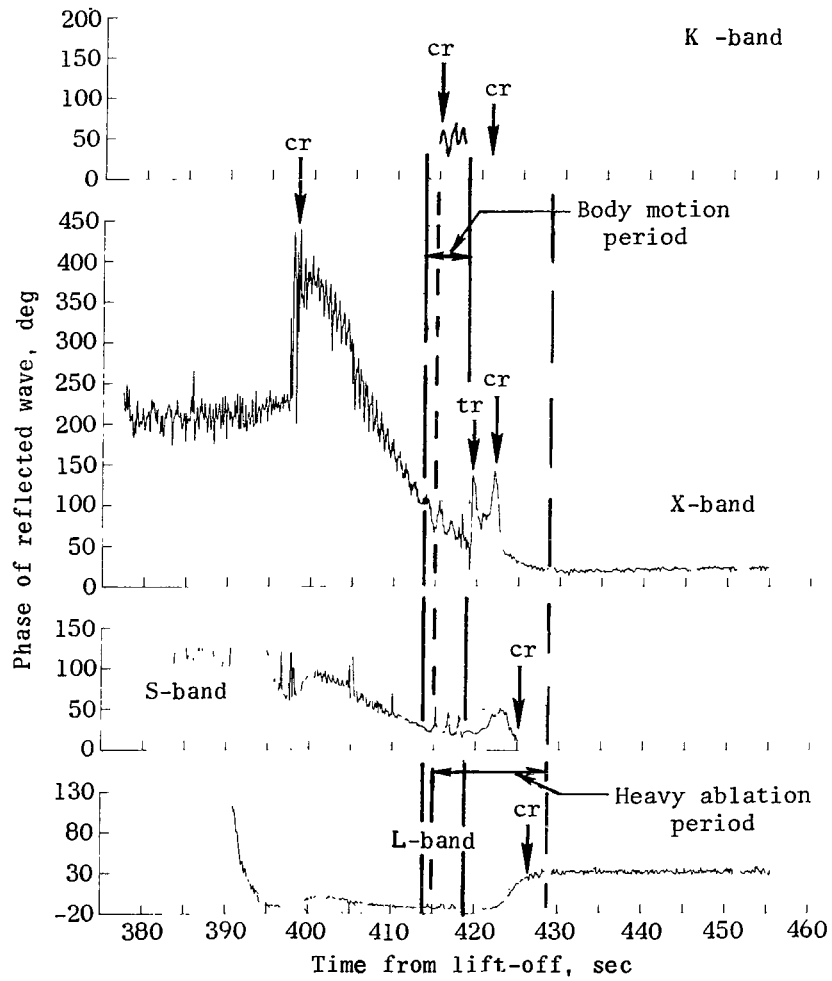
(d) Station 4 ($x/d_N = 3.5$).

Figure 3.- Concluded.



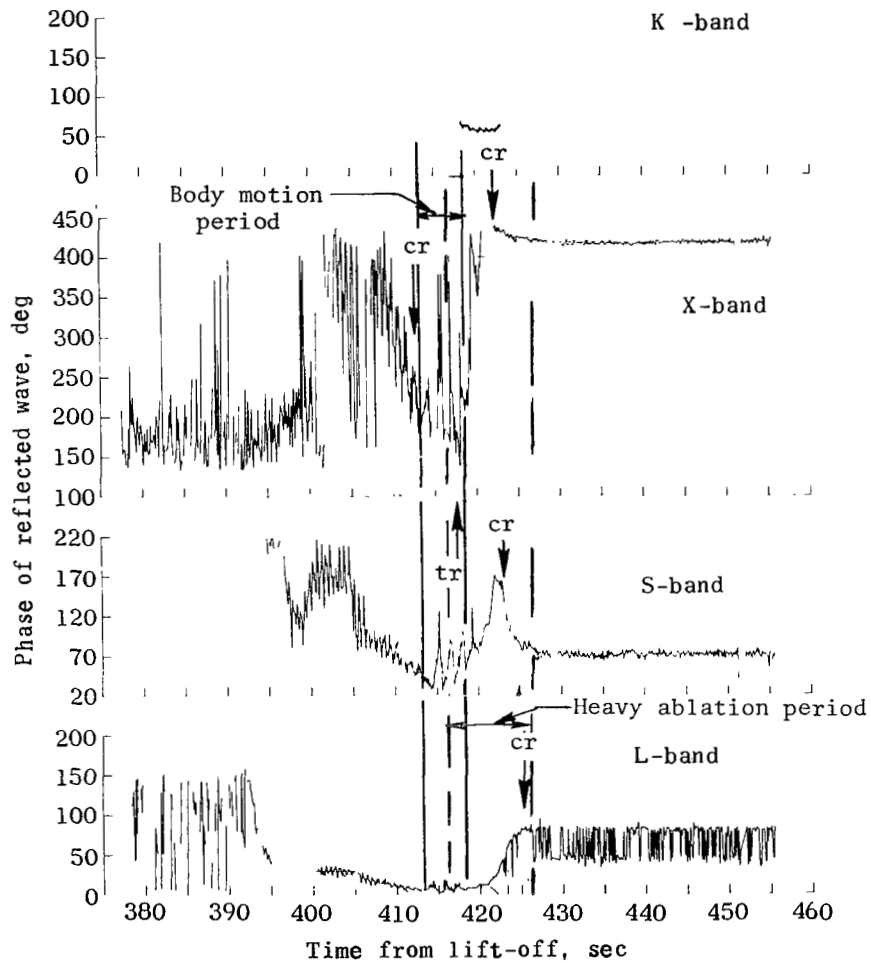
(a) Station 1 ($x/d_N = 0.15$).

Figure 4.- Measured phase coefficients taken from reference 8.



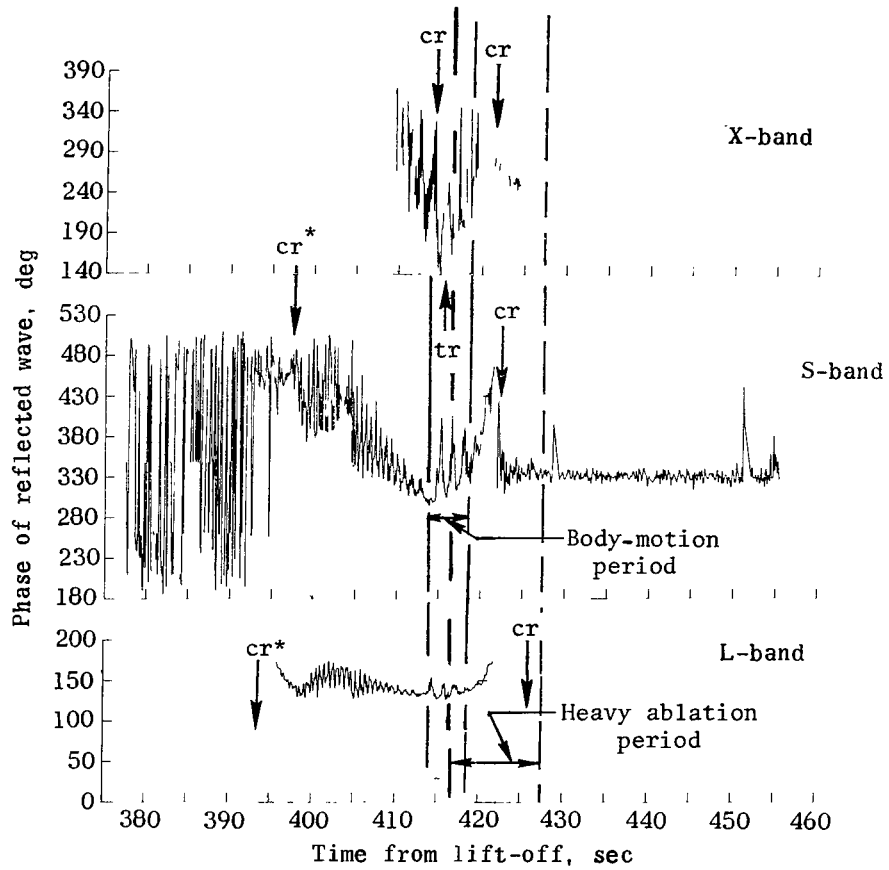
(b) Station 2 ($x/d_N = 0.76$).

Figure 4.- Continued.



(c) Station 3 ($x/d_N = 2.3$).

Figure 4.- Continued.



(d) Station 4 ($x/d_N = 3.5$).

Figure 4.- Concluded.

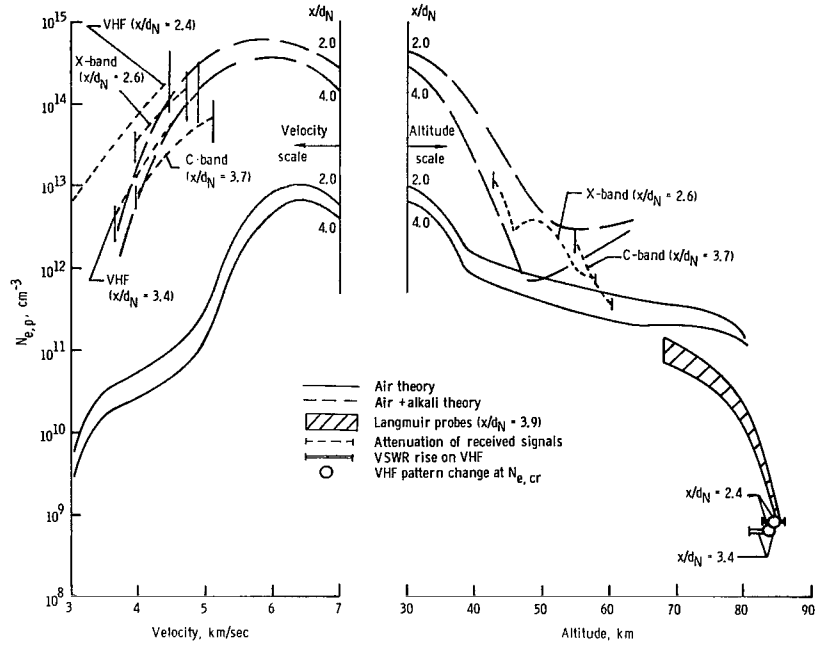


Figure 5.- Comparison of peak electron concentration with RAM C-I flight data.

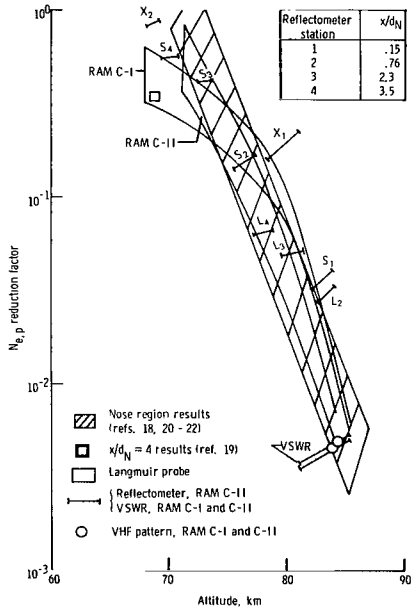


Figure 6.- Correlation of high-altitude data with electron-ion diffusion and wall effects factor.

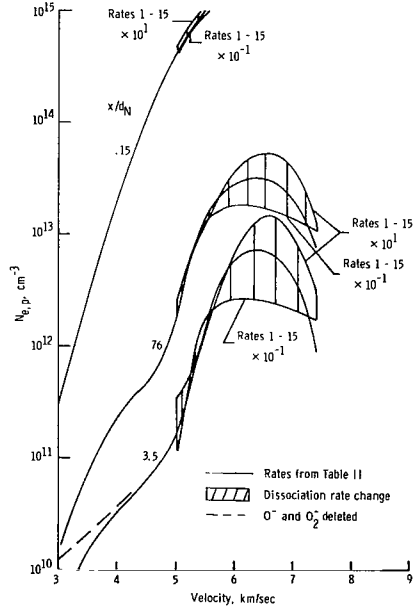


Figure 7.- Effects of reaction rate changes on electron concentration.

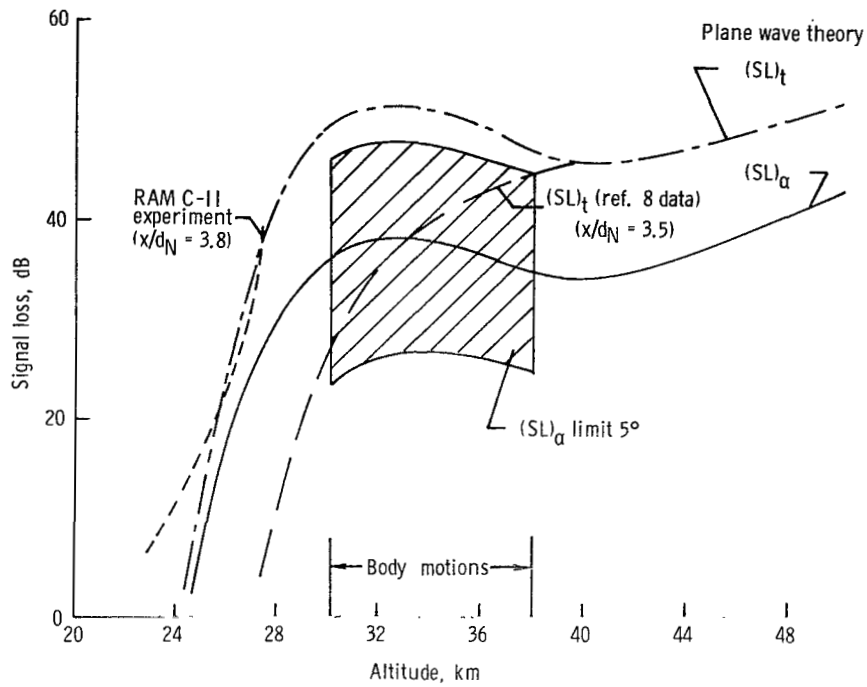


Figure 8.- VHF attenuation (226 MHz) for $x/d_N = 4$ using plane wave theory for RAM C-II vehicle at angles of attack of 0° and 5° .

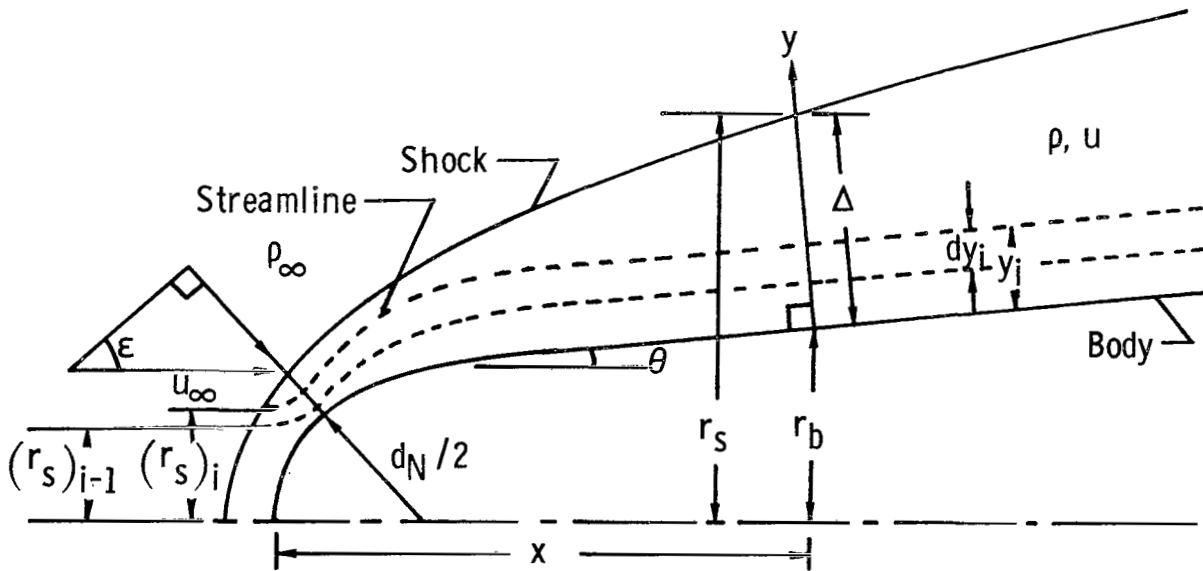


Figure 9.- Flow field and typical streamline paths.

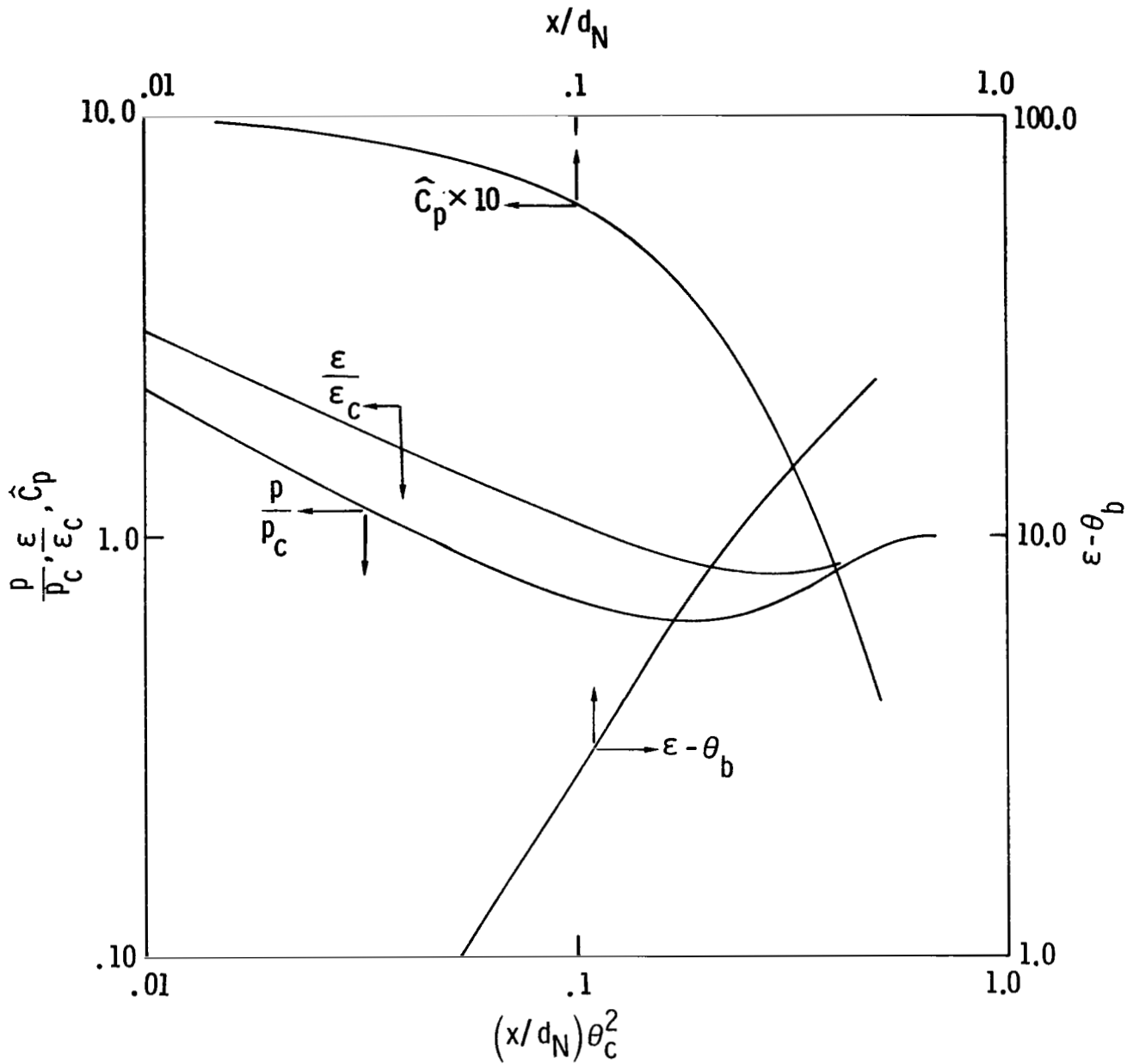


Figure 10.- Normalized shock shape and body pressure for equilibrium inviscid flow over a spherically blunted 9° half-angle cone.

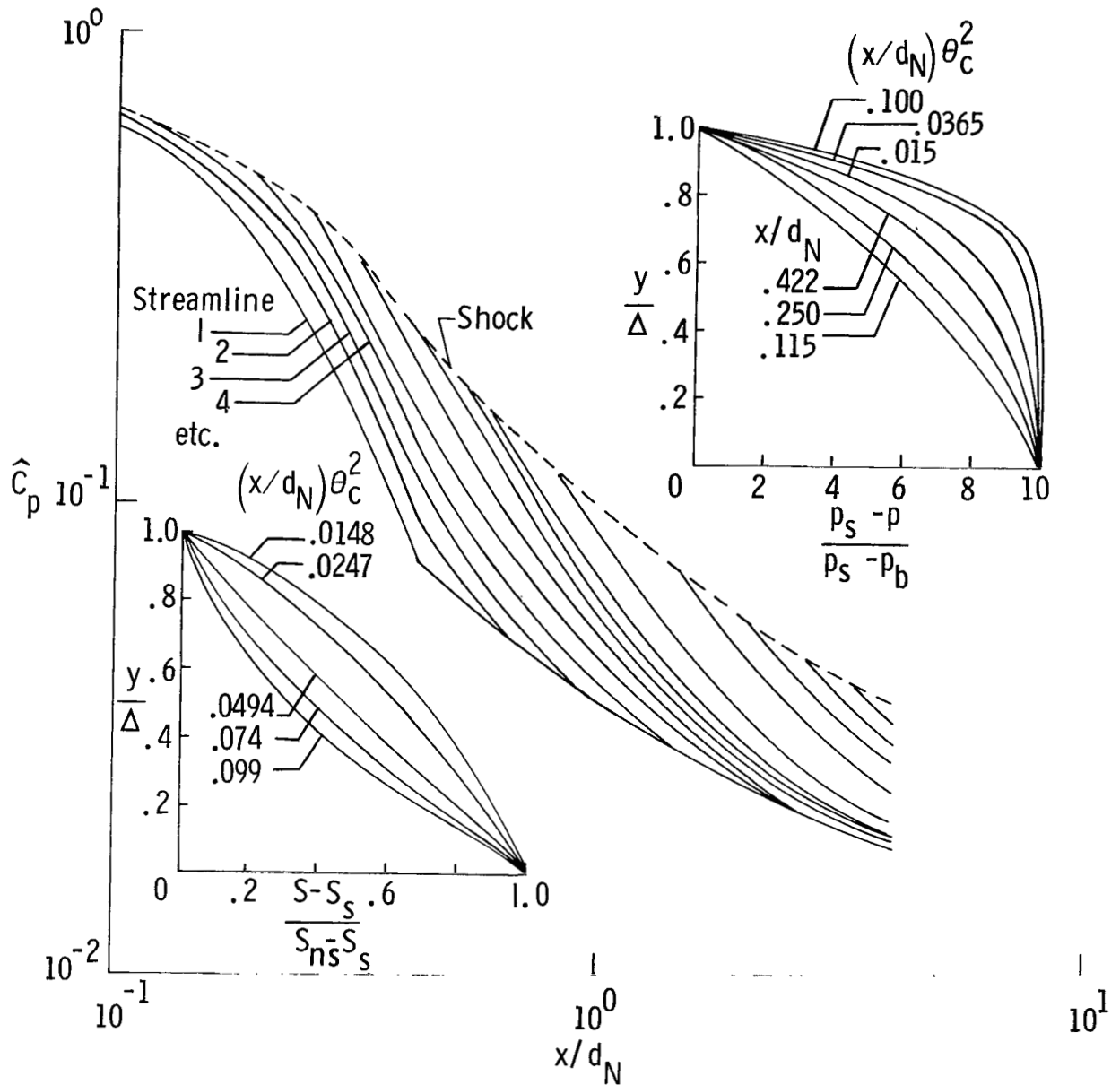
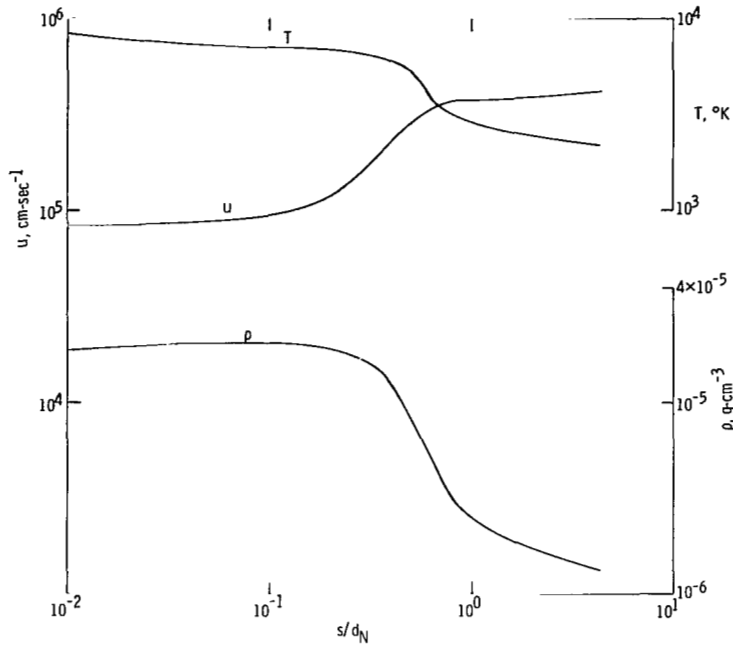
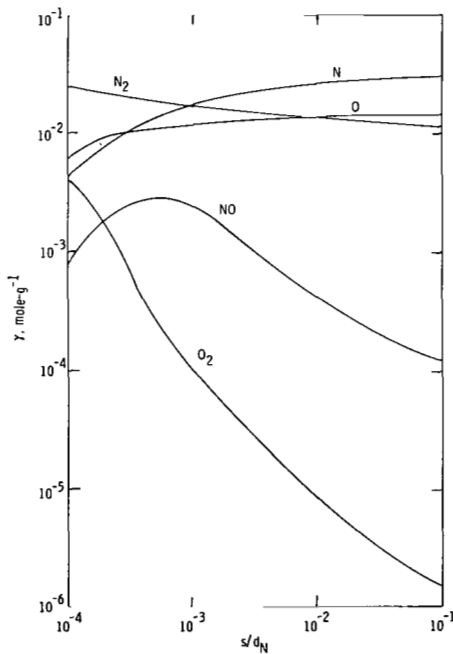


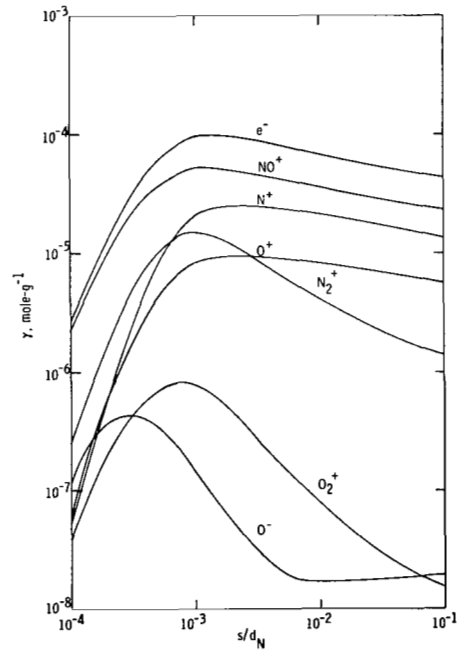
Figure 11.- Normalized pressure profiles, normalized entropy profiles, and streamline pressure distribution for équilibre inviscid flow over a spherically blunted 9° half-angle cone.



(a) Velocity, temperature, and density.



(b) Neutral species.



(c) Charged species.

Figure 12.- Inviscid flow-field properties along the body streamline.
Altitude, 47.55 km.

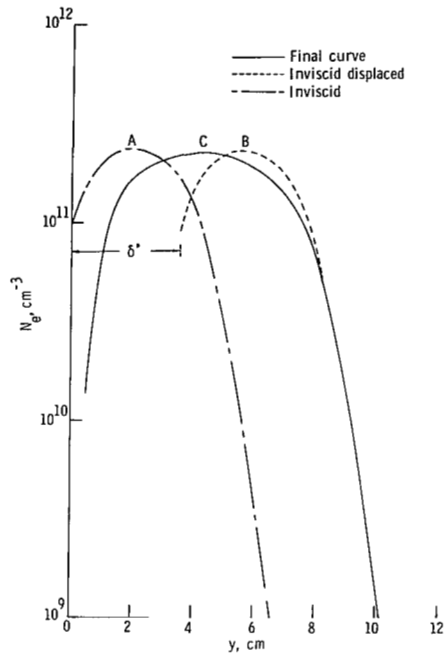


Figure 13.- Steps in calculation of an electron concentration profile. Altitude, 71.02 km; $x/d_N = 4$.

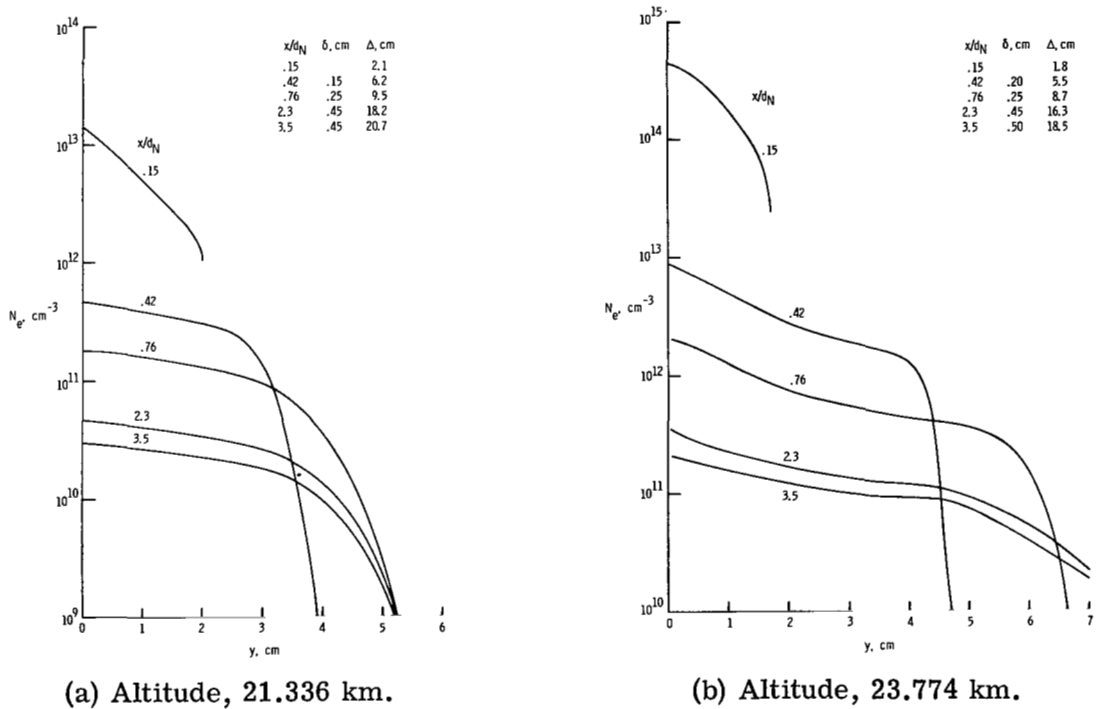
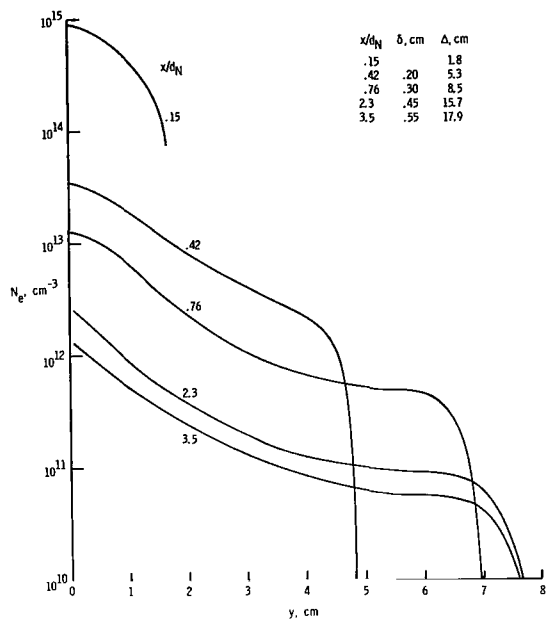
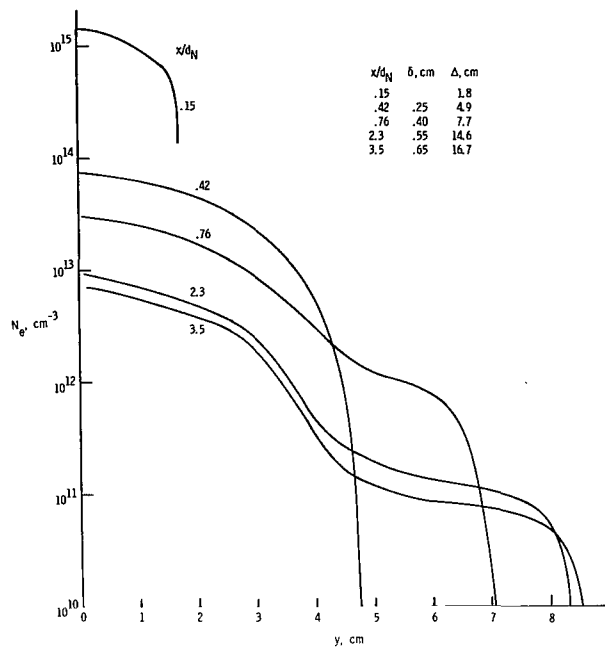


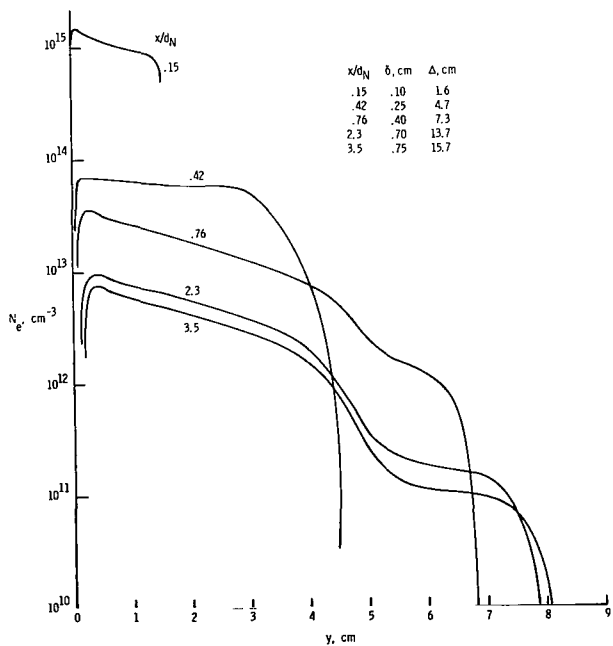
Figure 14.- Electron concentration profiles for air. (Fast $\text{NO}^+ + e$ recombination rate of ref. 48 used.)



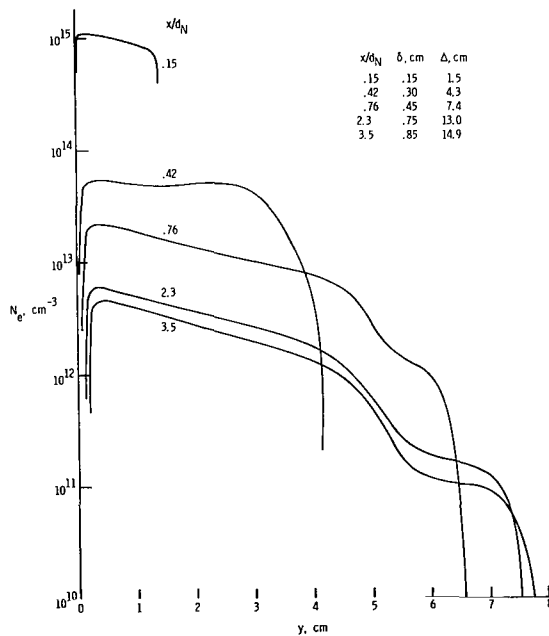
(c) Altitude, 25.146 km.



(d) Altitude, 27.999 km.

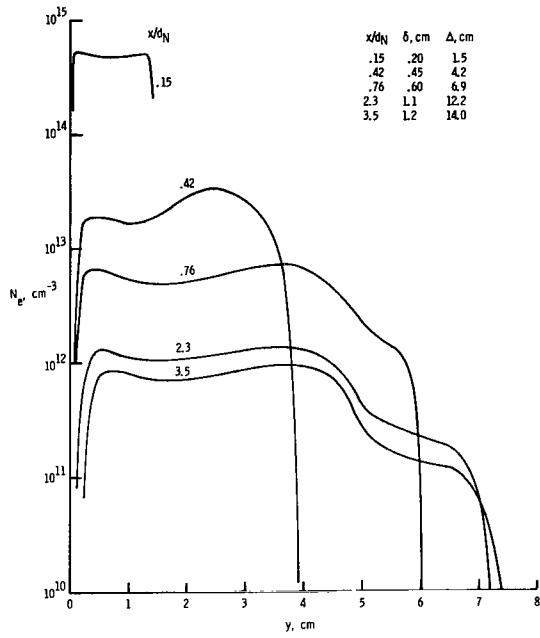


(e) Altitude, 30.632 km.

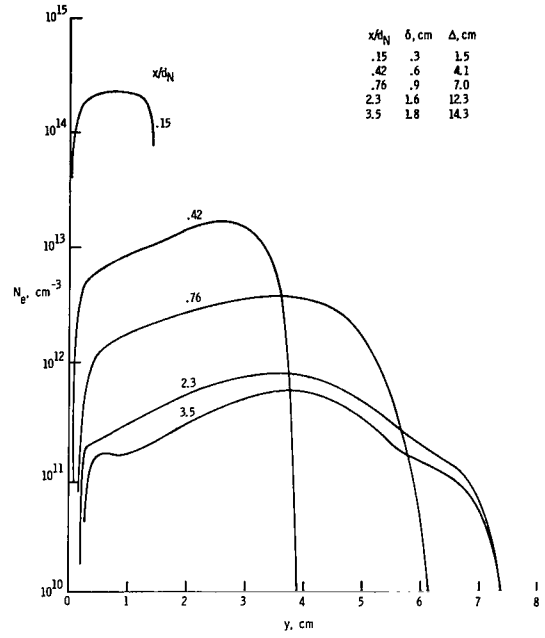


(f) Altitude, 33.706 km.

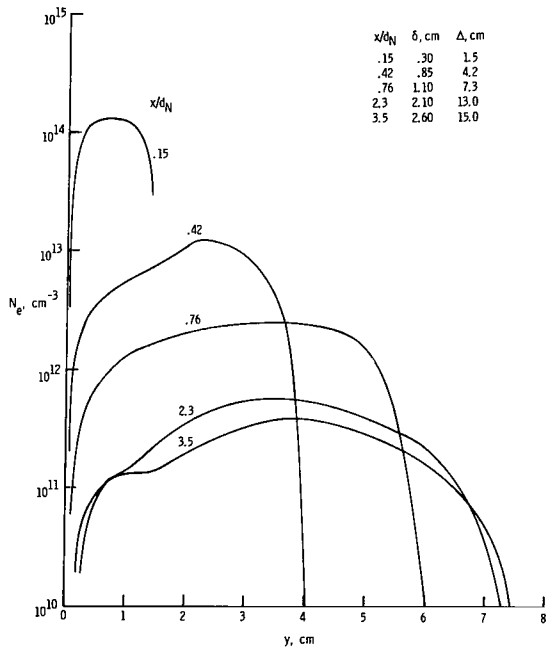
Figure 14.- Continued.



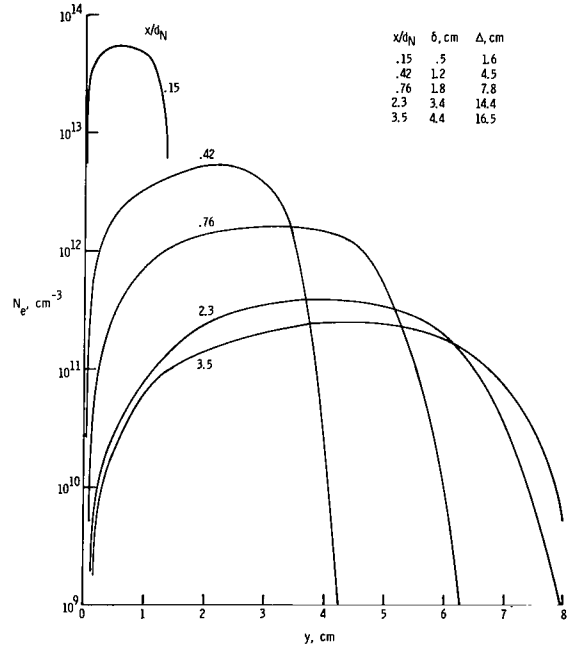
(g) Altitude, 40.000 km.



(h) Altitude, 47.549 km.

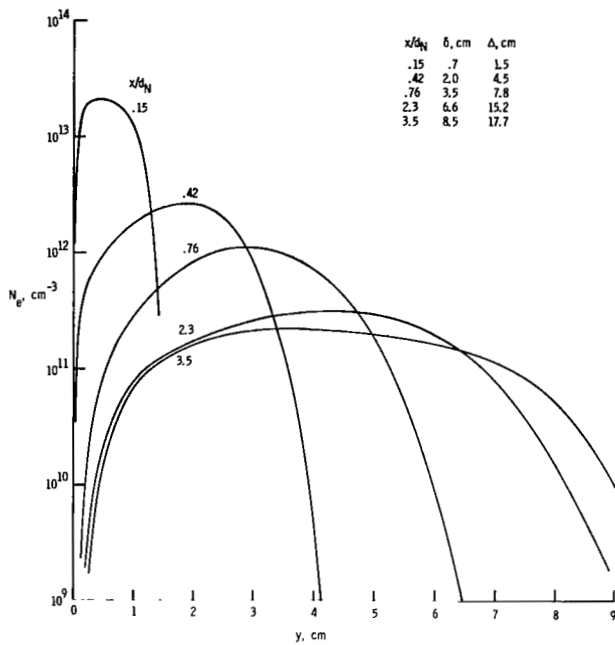


(i) Altitude, 53.340 km.

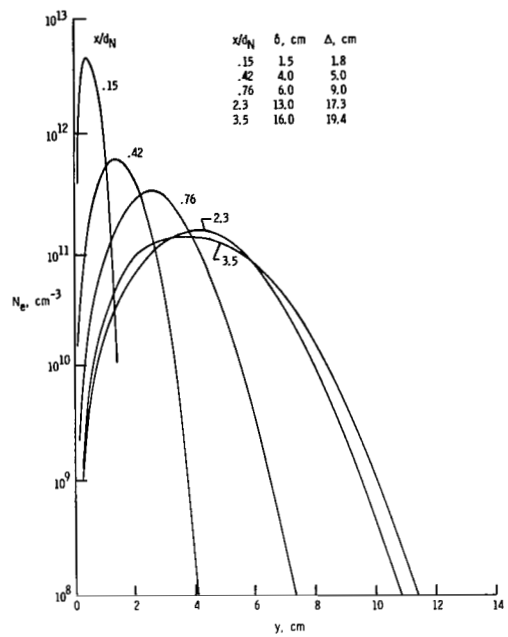


(j) Altitude, 61.570 km.

Figure 14.- Continued.



(k) Altitude, 71.018 km.



(l) Altitude, 80.162 km.

Figure 14.- Concluded.

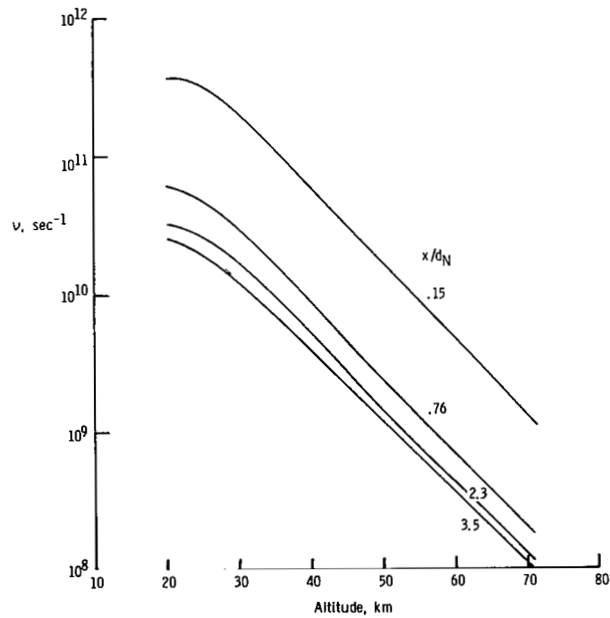


Figure 15.- Collision frequency for body streamline.

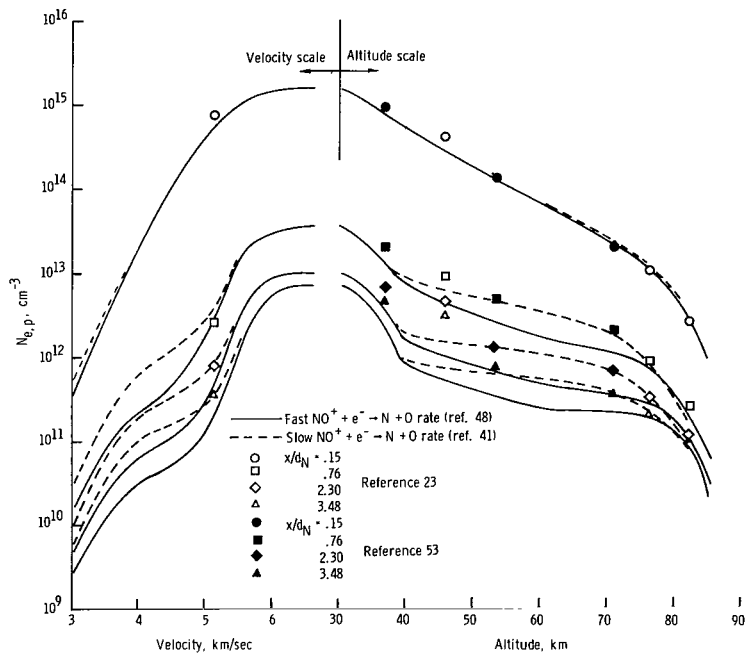


Figure 16.- Comparison of computed peak electron concentration (air theory) with previous calculations.

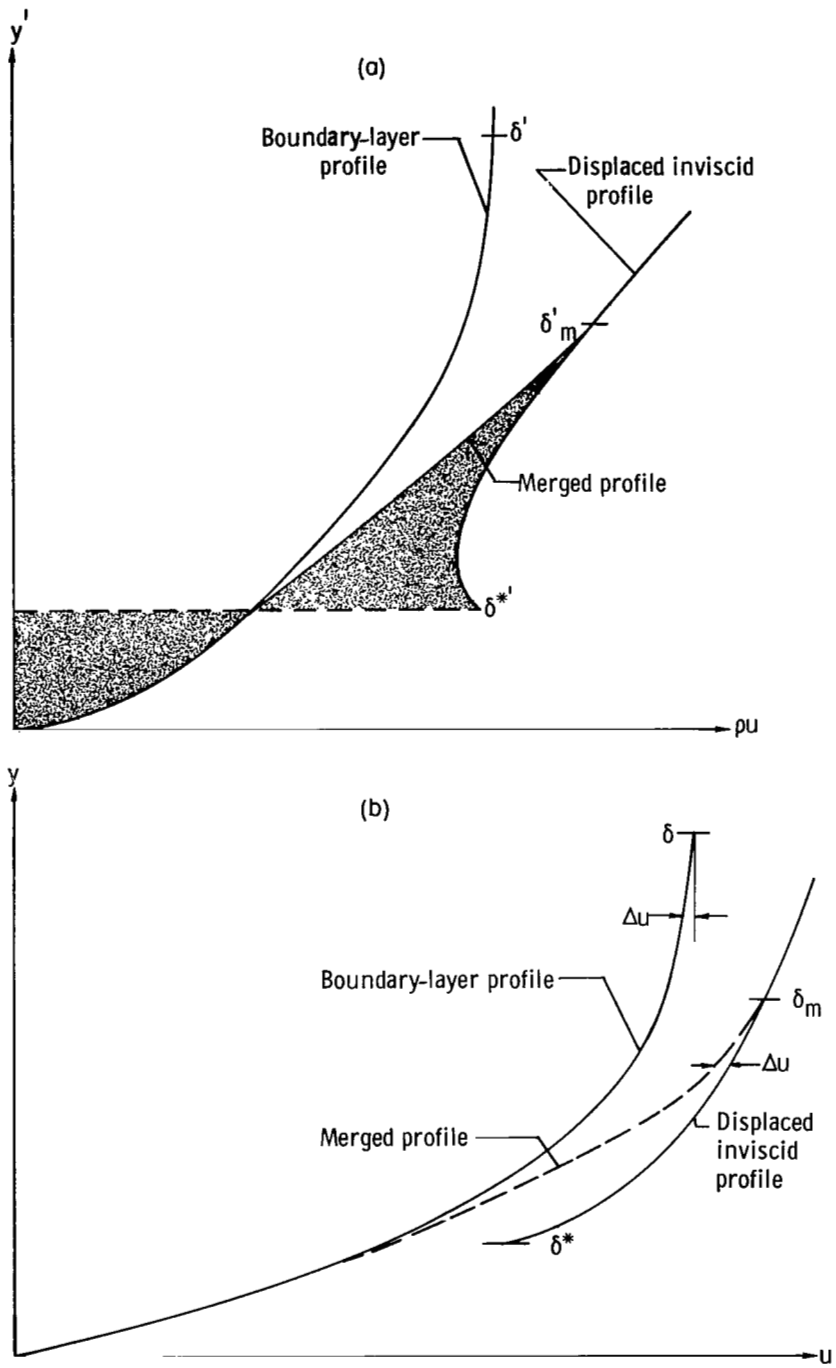


Figure 17.- Merging of inviscid and boundary-layer profiles.

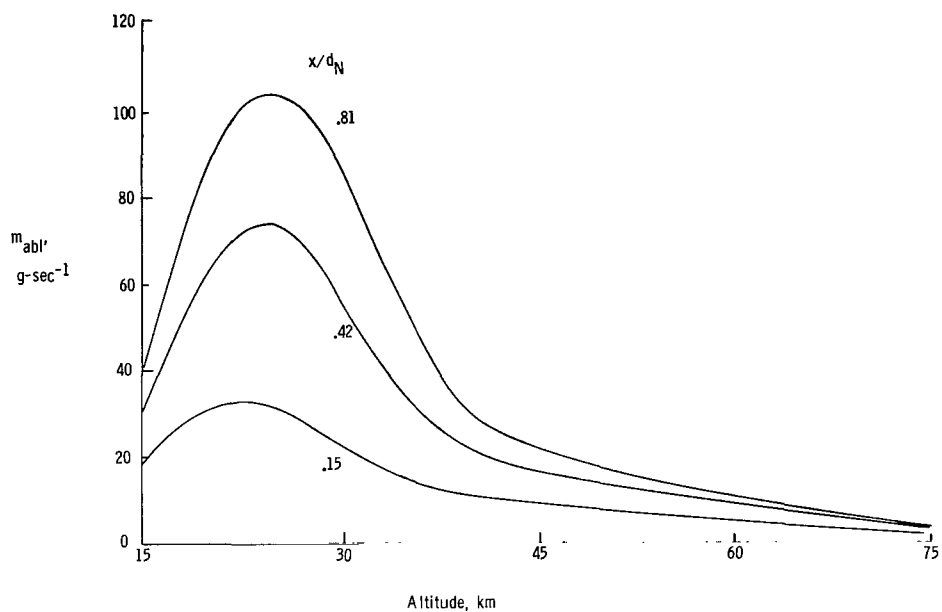


Figure 18.- Ablation rate for RAM C-I heat shield.

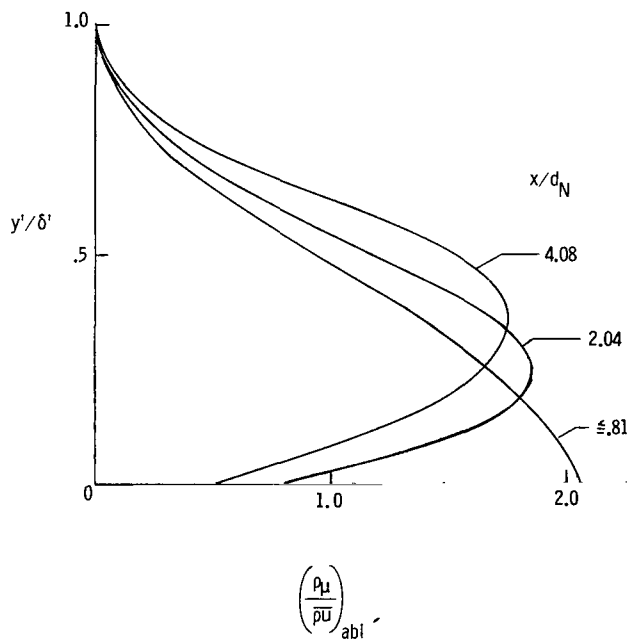
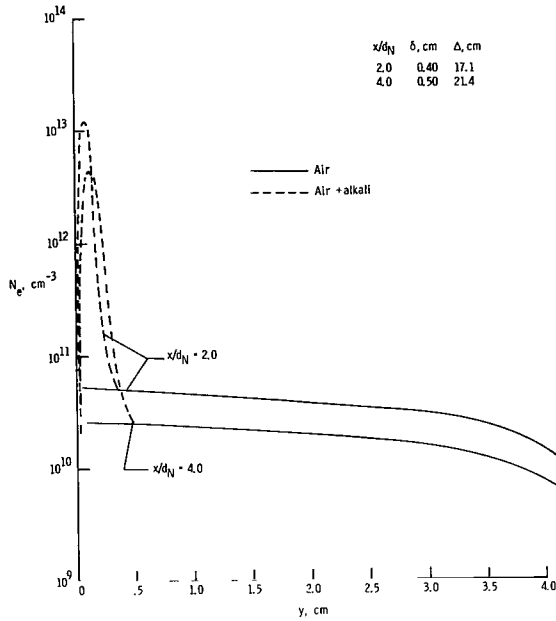
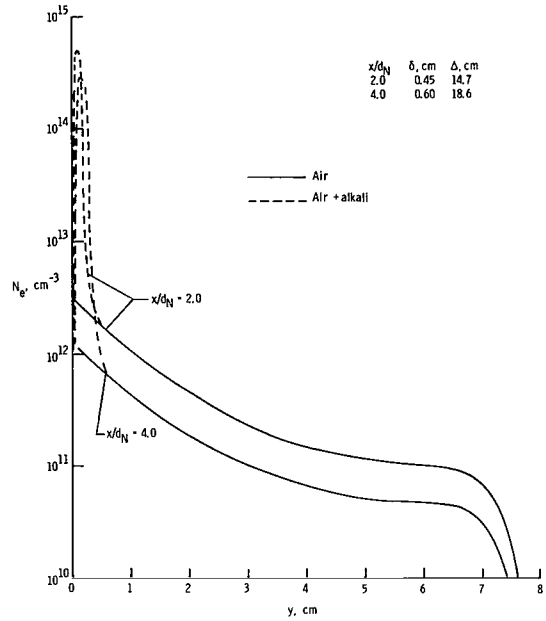


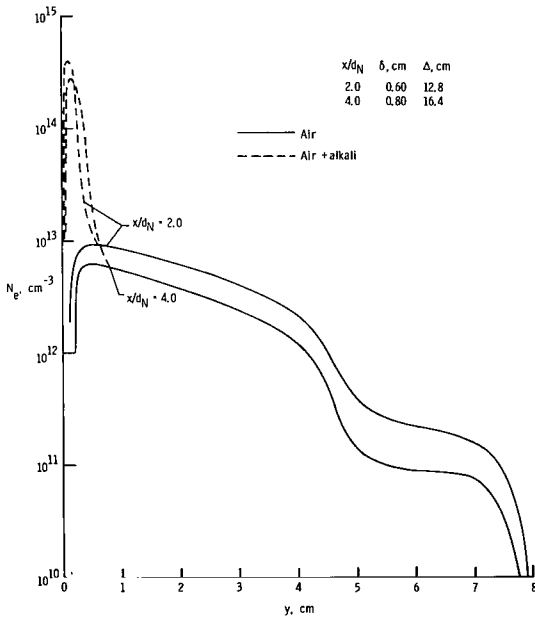
Figure 19.- Normalized distribution of NARMCO ablation gases in the RAM C boundary layer.



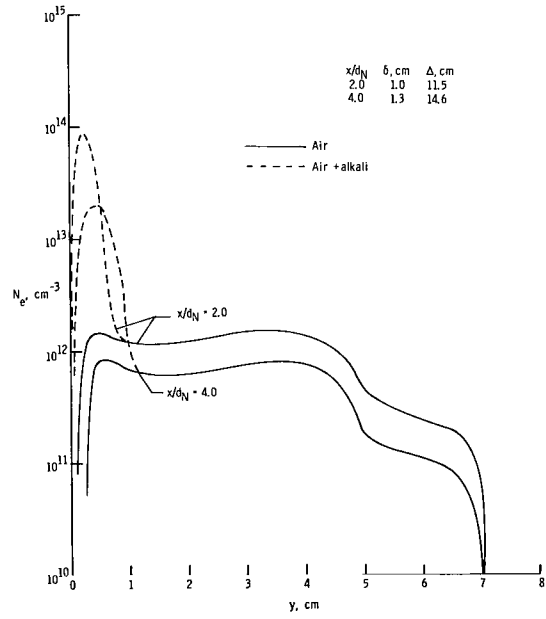
(a) Altitude, 21,336 km.



(b) Altitude, 25,146 km.

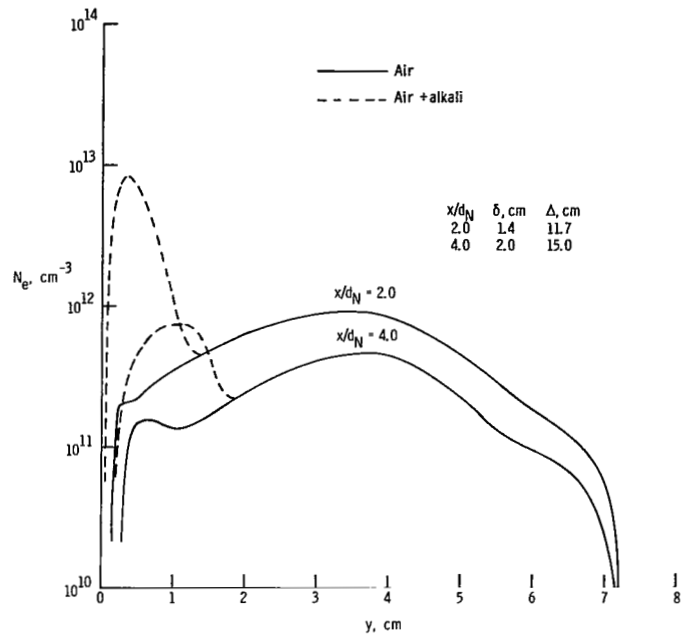


(c) Altitude, 30,632 km.

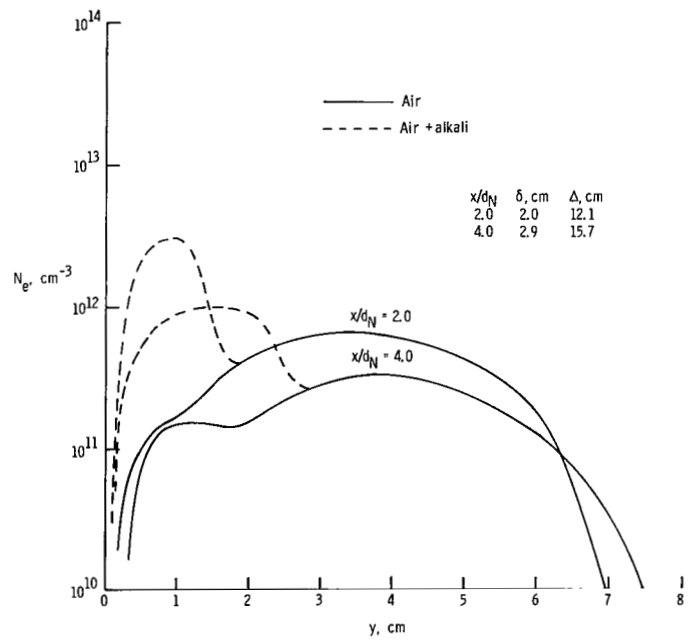


(d) Altitude, 40,000 km.

Figure 20.- Electron concentration profiles for air and air plus alkali in boundary layer. (Fast $\text{NO}^+ + e$ recombination rate of ref. 48 used.)

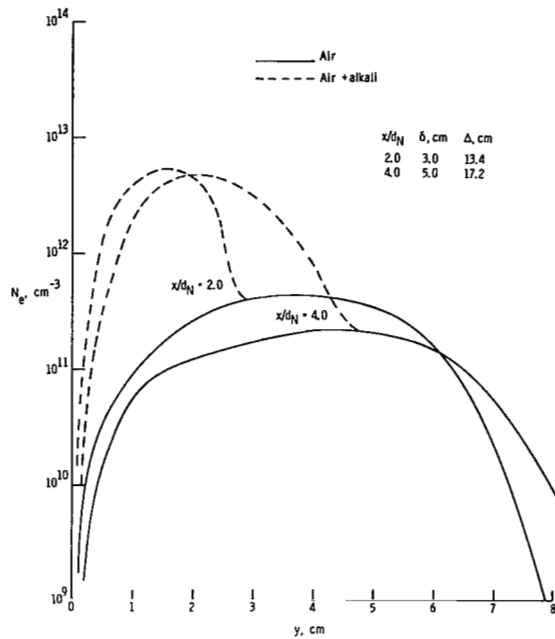


(e) Altitude, 47.549 km.



(f) Altitude, 53.340 km.

Figure 20.- Continued.



(g) Altitude, 61.570 km.

Figure 20.- Concluded.

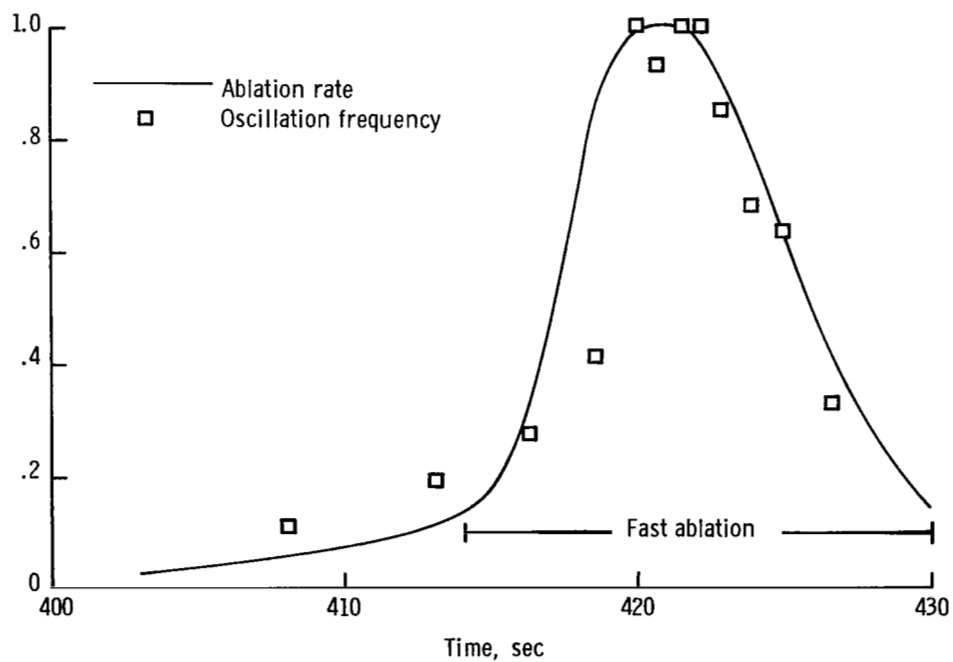


Figure 21.- Correlation of teflon ablation with K_1 reflectometer oscillations.

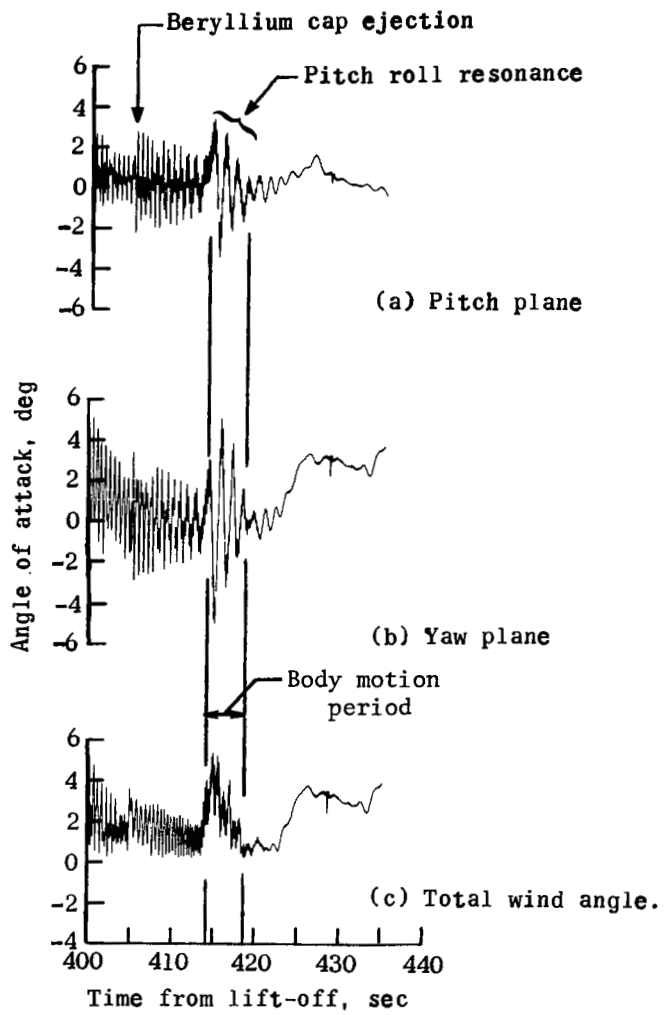
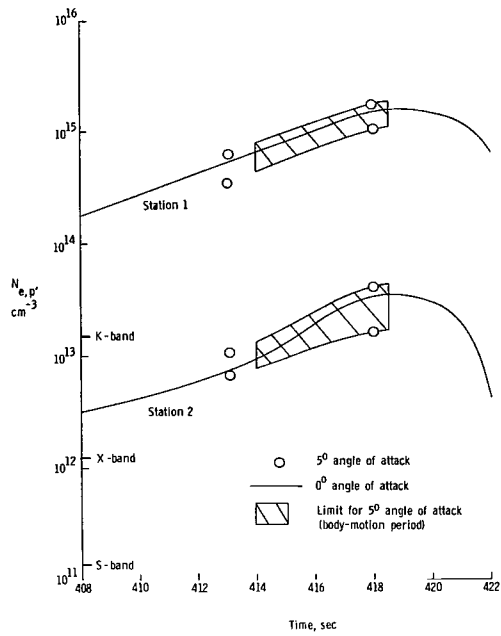
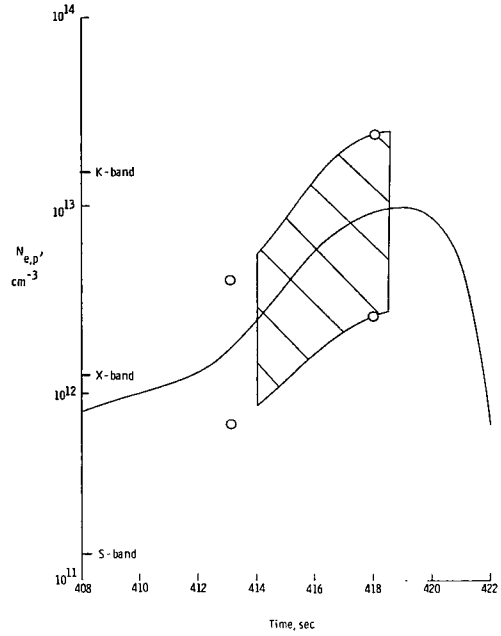


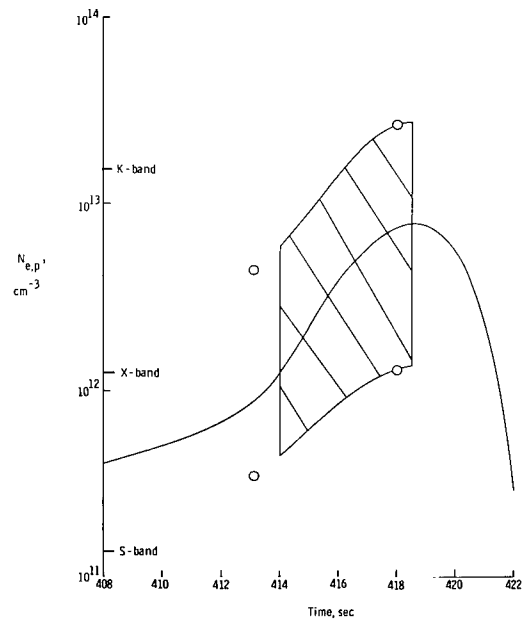
Figure 22.- Payload angle-of-attack time history.



(a) Stations 1 and 2.

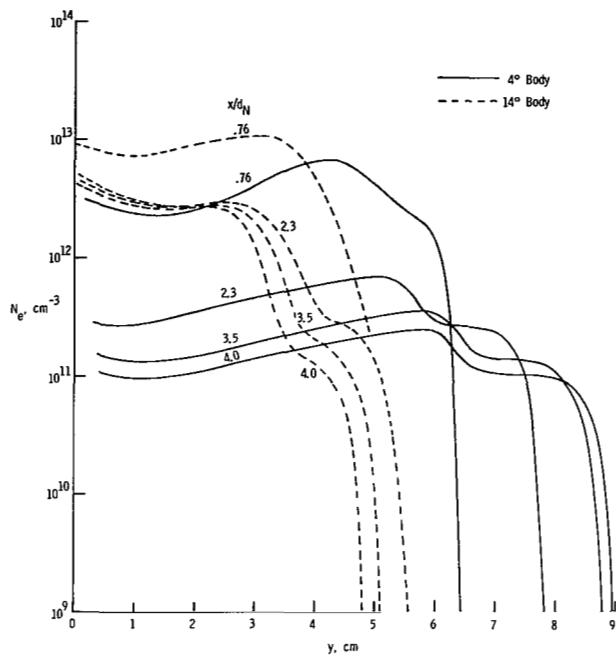


(b) Station 3.

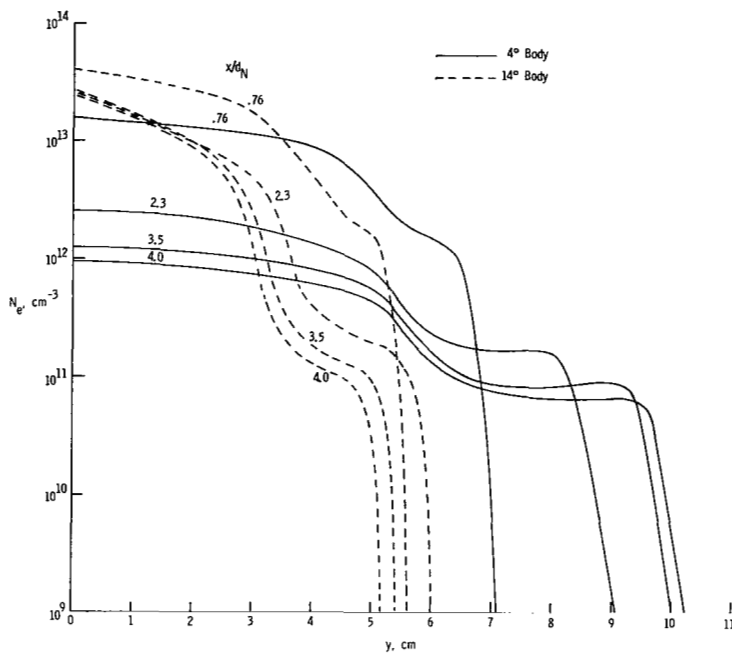


(c) Station 4.

Figure 23.- Theoretical peak N_e variation for an angle of attack of 5° at reflectometer stations.



(a) Altitude, 30.63 km.



(b) Altitude, 40.00 km.

Figure 24.- Electron concentration profiles for an angle of attack of 5° .

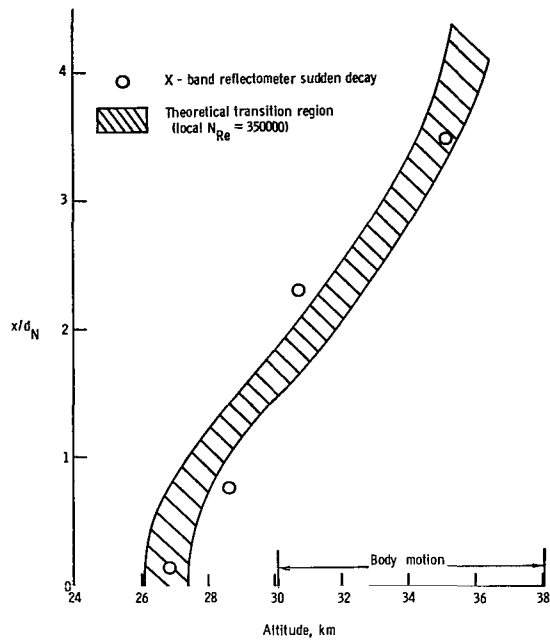


Figure 25.- Correlation of reflectometer decay from RAM C-II flight with boundary-layer transition.

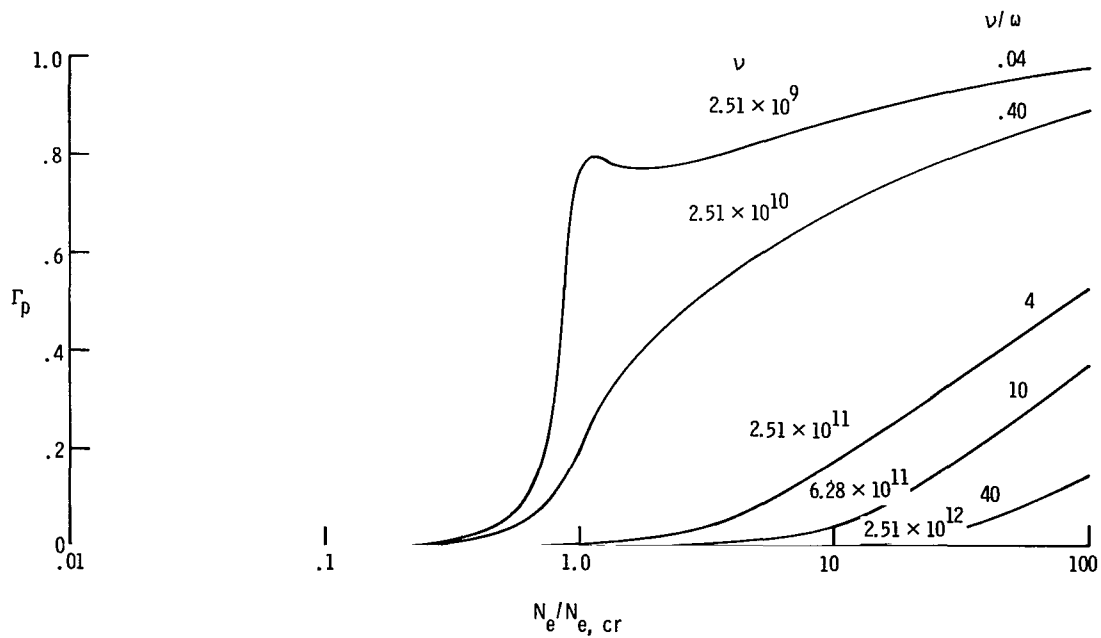
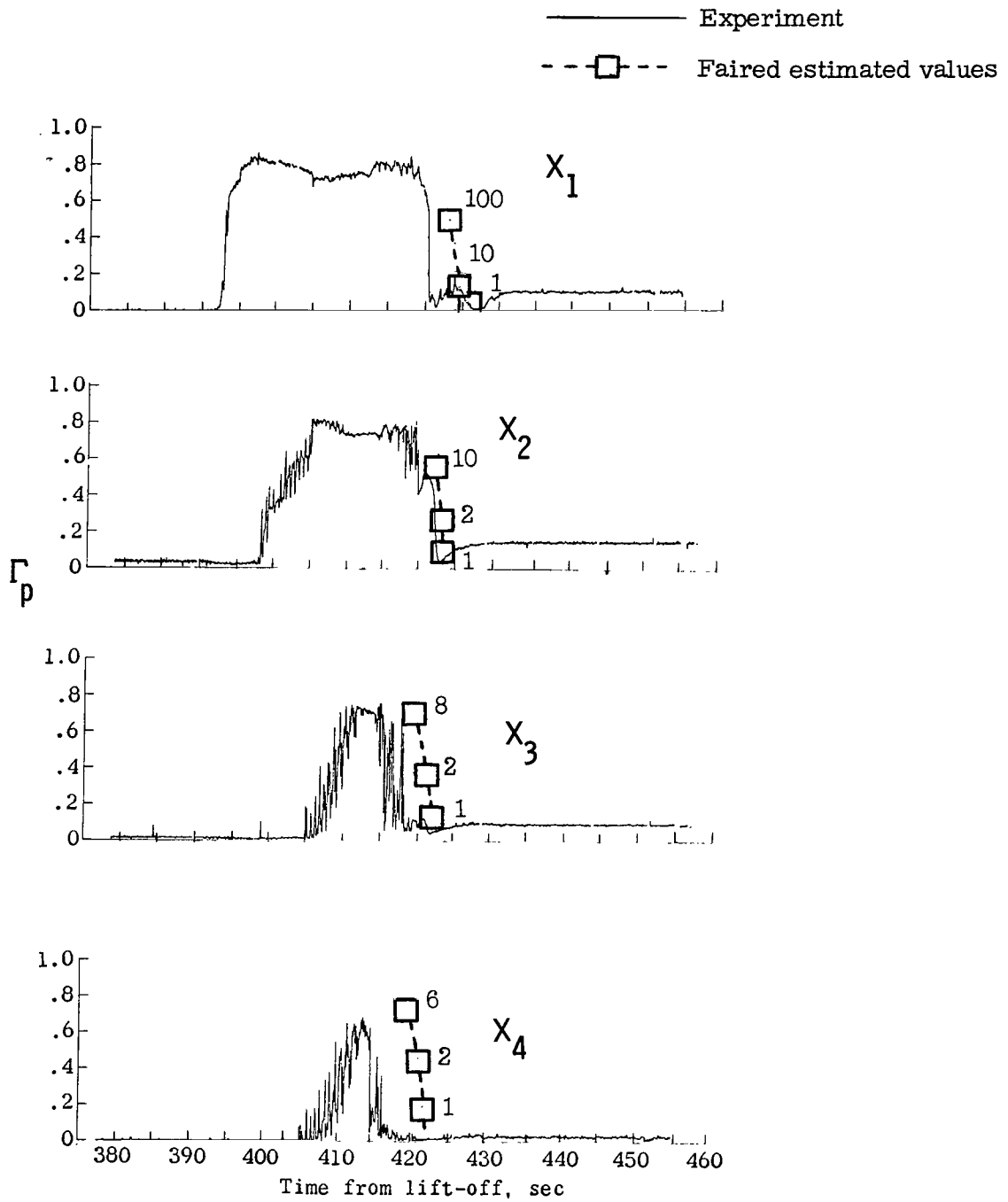
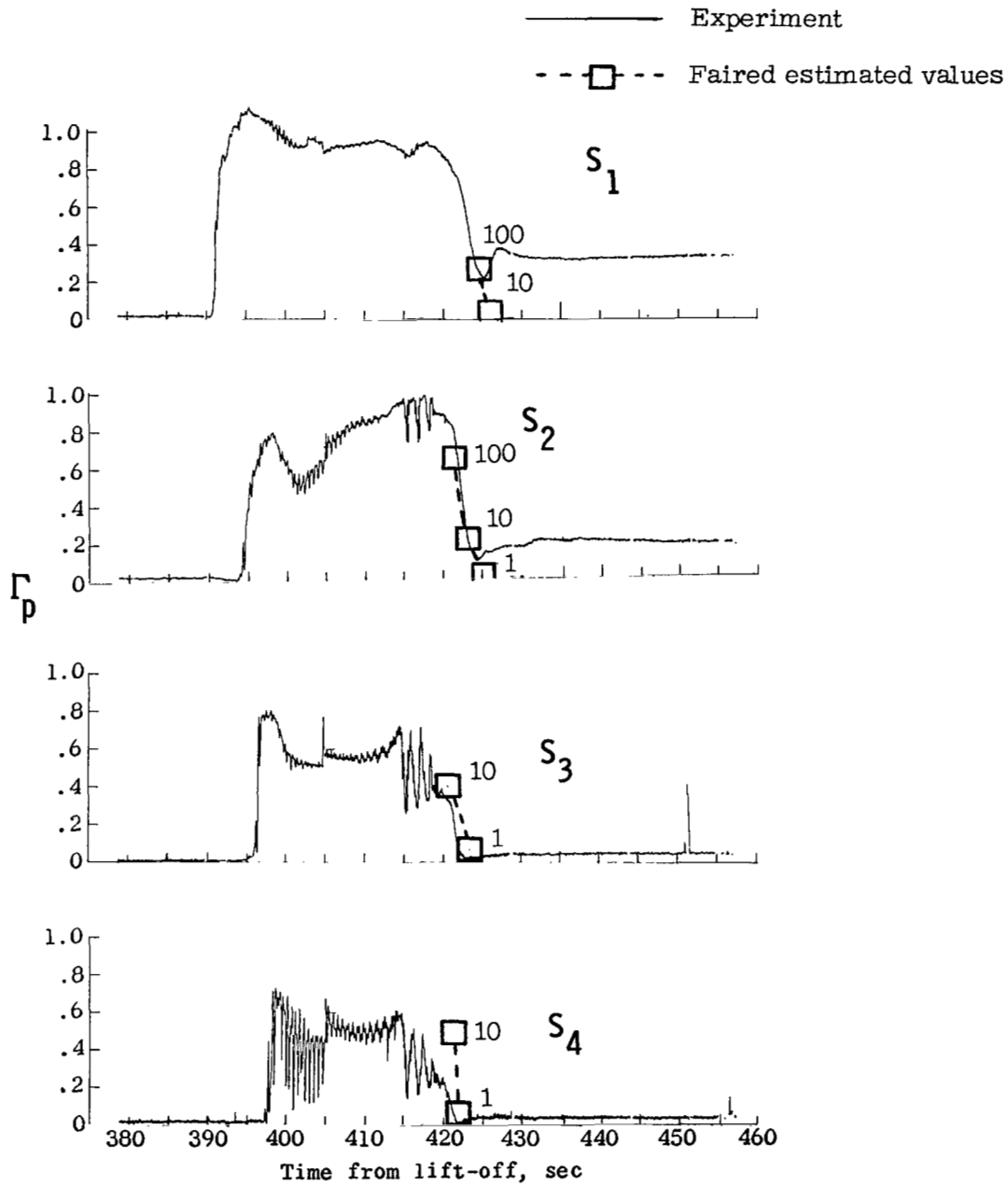


Figure 26.- Theoretical variation of reflection coefficient for X-band reflectometer at station 1.

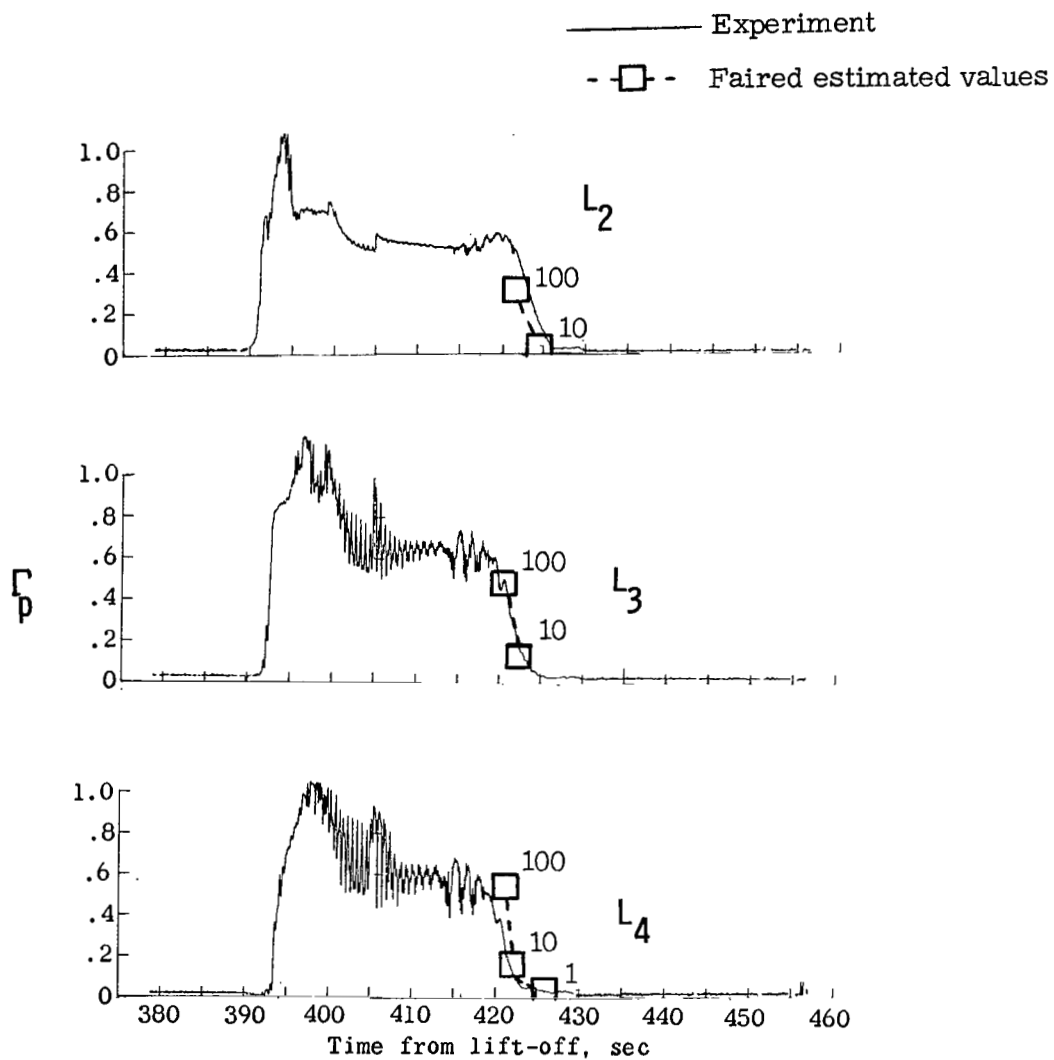


(a) X-band.

Figure 27.- Comparison of estimated reflection coefficient decay with experiment.
 (Numbers beside estimated points are values of $N_e/N_{e,cr}$)



(b) S-band.
Figure 27.- Continued.



(c) L-band.

Figure 27.- Concluded.

NATIONAL AERONAUTICS AND SPACE ADMINISTRATION

WASHINGTON, D. C. 20546

OFFICIAL BUSINESS
PENALTY FOR PRIVATE USE \$300

FIRST CLASS MAIL



POSTAGE AND FEES PAID
NATIONAL AERONAUTICS AND
SPACE ADMINISTRATION

09U 001 50 51 3DS 71135 00903
AIR FORCE WEAPONS LABORATORY /WL0L/
KIRTLAND AFB, NEW MEXICO 87117

ATT E. LOU BOWMAN, CHIEF, TECH. LIBRARY

POSTMASTER: If Undeliverable (Section 158
Postal Manual) Do Not Return

"The aeronautical and space activities of the United States shall be conducted so as to contribute . . . to the expansion of human knowledge of phenomena in the atmosphere and space. The Administration shall provide for the widest practicable and appropriate dissemination of information concerning its activities and the results thereof."

— NATIONAL AERONAUTICS AND SPACE ACT OF 1958

NASA SCIENTIFIC AND TECHNICAL PUBLICATIONS

TECHNICAL REPORTS: Scientific and technical information considered important, complete, and a lasting contribution to existing knowledge.

TECHNICAL NOTES: Information less broad in scope but nevertheless of importance as a contribution to existing knowledge.

TECHNICAL MEMORANDUMS: Information receiving limited distribution because of preliminary data, security classification, or other reasons.

CONTRACTOR REPORTS: Scientific and technical information generated under a NASA contract or grant and considered an important contribution to existing knowledge.

TECHNICAL TRANSLATIONS: Information published in a foreign language considered to merit NASA distribution in English.

SPECIAL PUBLICATIONS: Information derived from or of value to NASA activities. Publications include conference proceedings, monographs, data compilations, handbooks, sourcebooks, and special bibliographies.

TECHNOLOGY UTILIZATION PUBLICATIONS: Information on technology used by NASA that may be of particular interest in commercial and other non-aerospace applications. Publications include Tech Briefs, Technology Utilization Reports and Technology Surveys.

Details on the availability of these publications may be obtained from:

SCIENTIFIC AND TECHNICAL INFORMATION OFFICE

NATIONAL AERONAUTICS AND SPACE ADMINISTRATION

Washington, D.C. 20546